RADIATIVE NEUTRON CAPTURE BY DEUTERIUM

GEORGE MITEV

Triangle Universities Nuclear Laboratory
Department of Physics
Duke University

1984

RADIATIVE NEUTRON CAPTURE BY DEUTERIUM

by

George Mitev

Department of Physics
Duke University

Date: _____

Approved:

_____
Henry R. Weller, Supervisor

_____

_____

_____

_____

A dissertation submitted in partial fulfillment of
the requirements for the degree of Doctor
of Philosophy in the Department of
Physics in the Graduate School
of Duke University

1984

Abstract

RADIATIVE NEUTRON CAPTURE BY DEUTERIUM

by

George Mitev

Department of Physics
Duke University

Date: _____

Approved:

_____

Henry R. Weller, Supervisor

_____

_____

_____

_____

An abstract of a dissertation submitted in partial fulfillment of the requirements for the degree of Doctor of Philosophy in the Department of Physics in the Graduate School of Duke University

1984

RADIATIVE NEUTRON CAPTURE BY DEUTERIUM

by

George Mitev

A study of the $^{2}H(n,\gamma)^{3}H$ reaction has been performed employing polarized and unpolarized beams of neutrons.

Angular distributions of cross sections have been measured at E_n = 9.0, 10.8 and 14.0 MeV. An expansion in Legendre polynomials was fit to the data and the resulting coefficients are reported. Polarized neutrons were employed to measure an angular distribution of analyzing powers at E_n = 9.0 MeV. Coefficients resulting from fitting an expansion in associated Legendre polynomials to the angular distribution are reported. The combined analyzing power and cross section data at this energy were analyzed under simplifying assumptions to determine significant transition matrix elements of the $^{2}H(n,\gamma)^{3}H$ reaction. The data are consistent with (94.0 $\pm$ 3.4)% (s=1/2) E1, (3.3 $\pm$ 2.7)% (s=1/2) E2 and (2.7 $\pm$ 2.5)% (s=3/2) E1 admixtures, where s represents the incident channel spin.

Total cross sections have been determined at E_n = 9.0, 10.8 and 14.0 MeV from fits to the angular distributions. The total cross section at E_n = 6.85 MeV was calculated from $\sigma(90^{o})$ based on assumptions about the angular distribution. The reported values agree, after detail balancing, with photodisintegration data of Faul *et al.* (1980, 1981). Ninety degree differential cross sections of the $^{2}H(n,\gamma)^{3}H$ reaction, at

the above four energies, were compared with previous $^{2}H(p,\gamma)^{3}He$ measurements at TUNL (Skopik, 1979). The $^{2}H(p,\gamma)^{3}He$ to $^{2}H(n,\gamma)^{3}H$ ratios of cross sections are within a standard deviation of the value 1.0 predicted by direct capture calculations of this work.

Fore-aft asymmetries of the angular distributions of cross sections at E_n = 9.0 and 10.8 MeV were determined to be $a_s = -0.115 \pm 0.028$ and -0.136 ± 0.032 respectively. These values are surprisingly large in magnitude when compared with the predictions of two-body direct capture calculations. The data are consistent with an E2 strength which is enhanced relative to the theory by a factor of approximately two. A three-body direct capture calculation was performed in an effort to reconcile theory with experiment, but the results are essentially the same as those of the two-body calculations.

ACKNOWLEDGEMENTS

I would like to thank professor Henry Weller for his excellent guidance, constant encouragement and close companionship during my graduate career. His valuable advice contributed to my development as a scientist and to the success of the thesis experiment.

I am thankful to Denis Skopik for the use of the scintillating target. Paul Colby's assistance with practical and theoretical problems is greatly appreciated. In addition, I wish to acknowledge Don Lehman, Alphonse Van Hees and Dick Seyler for their theoretical contributions to the thesis.

Other contributors to the project include Mike Bailey, Sid Edwards, Bob Rummel, Paul Carter, Al Lovette and co.

I am grateful to the following past and present members of the capture group for their support and friendship: Dr.'s Steve King, Mike Wright, Bob August, Russell Roberson, Ron Tilley, Steve Wender, Colleen Fitzpatrick and current students Doug Wagenaar, John Riley and Mark Whitton.

The companionship of Ron Nelson and John Kolena, and the kindness of Tom and Suzie Fischer are warmly appreciated. The affection and encouragement of Janet Blum is especially cherished.

My dearest love to my father Atanas, whose bold move to America

established the foundation upon which my education and scientific career have grown; to my mother Milosava, whose strength during times of difficulty kept the family strong and allowed me the freedom to pursue my goals; and to Dušica and Veljko Lalich, for their constant support over many years. Finally, the concern of relatives in Yugoslavia for my well-being is appreciated and I look forward to seeing them again in the future.

TABLE OF CONTENTS

List of Figures

List of Tables

1 INTRODUCTION

1.1 Motivation for the $^2H(n,\gamma)^3H$ Study

The reasons for performing the $^2H(n,\gamma)^3H$ experiment may be stated in light of the following questions. First of all, why study the three-nucleon system? The three-nucleon system is one of the simplest examples of a many-body problem in nuclear physics. It is well-suited for application of the nucleon-nucleon potential within the framework of a many-body theory. Indeed, three-nucleon wave functions derived from the analytic Faddeev formalism are available (Gibson, 1984), and comprehensive calculations of reaction observables are forthcoming (Lehman, 1984). The observables measured in this experiment will test the extent to which this theoretical model is valid and may indicate the need for other degrees of freedom.

Next, why study the three-nucleon system with the $^2H(n,\gamma)^3H$ capture reaction? The data of this work are the first ever $^2H(n,\gamma)^3H$ angular distribution measurements at non-thermal neutron energies, thus providing an entirely new set of observables for comparison with theory. In addition, insights now stand to be gained from comparisons with results of other photonuclear reactions, such as $^2H(p,\gamma)^3He$, $^3H(\gamma,n)^2H$ and $^3H(e,e'd)n$. The capture reaction, which proceeds via an electromagnetic transition, is an excellent nuclear probe because the electromagnetic operator is well known. Less uncertainty in the operator implies greater sensitivity to the wave functions representing

the initial and final states, thus yielding information about nuclear structure. From a data analysis standpoint, the $^{2}H(n,\gamma)^{3}H$ experiment has the following desirable characteristics. The reaction proceeds via one channel, as opposed to photodisintegration which can yield both two-body and three-body break-up. The $^{2}H(n,\gamma)^{3}H$ experiment involves real photons, as opposed to electron scattering experiments, so ambiguities associated with virtual photon spectra do not enter into the analysis of the data.

Finally, why measure the specific observables which were measured in this experiment? Electrodisintegration data of Skopik et al. (1981) yielded surprisingly large asymmetries (a_s) in angular distributions of cross sections. Angular distribution measurements at E_n = 9.0 and 10.8 MeV were performed in order to investigate this anomaly. An angular distribution of analyzing powers at E_n = 9.0 MeV was obtained by employing a polarized neutron beam. The analyzing powers and cross sections combined made possible a transition matrix element analysis of the data which determined the strengths of electric dipole (channel spins 1/2 and 3/2) and electric quadrupole (channel spin 1/2) transitions at that energy. A comparison was made with results of the same analysis performed by King (1983, 1984) for the case of $^{2}H(p,\gamma)^{3}He$. Ninety degree differential cross sections were obtained at E_γ = 10.81, 12.23, 13.43 and 15.50 MeV. The ratios of these $^{2}H(n,\gamma)^{3}H$ cross sections to $^{2}H(p,\gamma)^{3}He$ cross sections of Skopik et al. (1979) were calculated in order to test for deviation from the expected value of one. Total cross sections were determined at the same four energies in

order to confirm photodisintegration measurements of Faul et al. (1980, 1981).

The methods employed, results attained and conclusions drawn from an investigation of the $^{2}H(n,\gamma)^{3}H$ reaction are presented in this dissertation. In addition, the following brief description of the ^{3}H wave function is presented as introductory information. For greater detail refer to the reviews of Delves and Phillips (1969) and Amado (1969) from which this discussion is drawn.

1.2 The ^{3}H Wave Function

A physical state may be labeled by a set of absolute quantum numbers which represent the conserved properties of the state. In the case of nuclear systems these "good" quantum numbers are few, partly due to the presence of both electromagnetic and nuclear forces in a nucleus, and partly because the strong nuclear interaction does not have a simple form. The strong interaction is known to depend not only on central forces, but also on noncentral and exchange forces. The total angular momentum and its projection are good quantum numbers of a nuclear state. However, due to noncentral forces, orbital and spin angular momenta are not. Conservation of charge implies another good quantum number which, in the isospin formalism, is the projection of the total isospin. The total isospin itself is not conserved in the presence of electromagnetic forces. Parity, the symmetry of the state under spatial reflection through the origin, is also a good quantum number of a

nuclear system.

The total angular momentum of the ^3H nucleus is $J = 1/2\ \hbar$, a fact initially established by spectroscopic measurements of hyperfine levels (Bloch, 1947) and molecular rotational levels (Dieke, 1949). The isospin projection of ^3H is $T_3 = +1/2$, a straightforward result since neutrons are assigned an isospin of +1/2 while protons are assigned -1/2. For a three-nucleon system, a projection of +1/2 can arise from a total isospin of $T = 1/2$ or $T = 3/2$. However, since there is no experimental evidence for the existence of trineutrons or ^3Li nuclei, it is assumed that ^3H and ^3He are states of the $T = 1/2$ isospin doublet. Theoretical predictions of Ohmura (1967, 1969) imply a $T = 3/2$ probability of less than 10^{-4}. The parity (π) of the ^3H nucleus is known to be even.

With the knowledge that the ^3H wave function must be characterized by the quantum numbers $J^{\pi}(T) = 1/2^{+}(1/2)$, and keeping in mind that ^3H is a system of three fermions, one can proceed to classify contributing admixtures of states in the wave function based on spatial, spin and isospin symmetries. Of course, the Pauli principle requires that the overall wave function be antisymmetric upon interchange of all coordinates of any two particles. Derrick and Blatt (1958) have performed such a classification and have shown that the $J^{\pi}(T) = 1/2^{+}(1/2)$ three-nucleon system may be represented in terms of ten states. Expressed in spectroscopic notation ($^{2S+1}L_J$) they are three $^2S_{1/2}$ states, three $^2P_{1/2}$ states, one $^4P_{1/2}$ state and three $^4D_{1/2}$ states.

Only some of the allowed states contribute significantly to the overall ^3H wave function. In particular, the dominant part of the wave function is expected to be S-state. This is because the ground state is by definition the lowest energy state, and L = 0 minimizes the rotational contribution to the energy of the system. Experimentally, the magnetic moment of ^3H, $\mu = +2.979$ nm (Wapstra, 1977), is evidence for a predominantly S-wave ground state. Since this value is very nearly equal to the magnetic moment of the proton, the implication is that the two neutron spins couple to zero and that the orbital angular momentum of the system is zero.

The classification of Derrick and Blatt gives rise to three $^2S_{1/2}$ states which are distinguishable by their symmetry with respect to space coordinates. One of these $^2S_{1/2}$ states is symmetric upon interchange of any two nucleons, another has mixed symmetry while the third is anti-symmetric. Historically, these three states have been referred to as the S, S' and S" states respectively. A spatially symmetric wave function adds stability to a nuclear system by virtue of its low kinetic energy (Blatt, 1952), consequently it is the symmetric S state which dominates the overall ^3H wave function. By contrast, a spatially anti-symmetric wave function is indicative of large kinetic energy and should be negligibly small in this case. A variational calculation by Delves et al. (1969) predicts the S" probability for ^3H to be less than 10^{-6}.

Other admixtures which are calculated to be negligibly small are

the P states (Delves et al., 1969). They arise through the spin-orbit force which, in ^{3}H, is a small effect (Derrick, 1960). They also arise from the tensor force, but this is a second order contribution (Delves and Phillips, 1969).

Thus far it has been established that the principal part of the ^{3}H wave function is S-state and that the S" and P states are unimportant. Before discussing the significance of the S' and D states it is useful to explicitly define the individual i-state probability as

$$P_i = \int_0^\infty |u_i(r)|^2 \, dr, \qquad 1\text{-}1$$

with normalization $\Sigma P_i = 1$. The functions $u_i(r)$ are related to radial wave functions according to $u_i(r)/r = \Psi_i(r)$. Amado (1978) has pointed out that the probabilities P_i are not experimental observables. Instead, they are parameters indicative of the strengths of individual states within the context of a theoretical model (King, 1983). Calculations aimed at predicting ground state properties of ^{3}H (see Table 1-1) have included varying percentages of S-state, S'-state and D-state probabilities. It is common to refer singularly to the overall D-state probability because the individual D states should have approximately equal strengths (Derrick, 1958). Variational calculations (Delves et al., 1969; Ohmura, 1969; Hennell, 1975) and Faddeev calculations (Barbour, 1967; Payne, 1980; Sasakawa, 1981; Gibson, 1984) have produced three-nucleon wave functions with P_S, ranging up to 4% and P_D up to 10%. Calculations of binding energy, electric radius, magnetic radius and magnetic moment are sensitive to the presence of the S'

Table 1-1. Measured ^{3}H properties.

Observable	Value	Reference
Binding energy (MeV)	8.48196 ± 0.00006	Wapstra and Bos (1977)
Electric radius (fm)	1.67 ± 0.06	Beck *et al.* (1982)
Magnetic radius (fm)	1.70 ± 0.05	Collard *et al.* (1965)
Magnetic dipole moment (nm)	2.978960 ± 0.000001	Lederer (1978)
^{3}H-^{3}He difference in binding energy (MeV)	0.74378 ± 0.00006	Wapstra and Bos (1977)

state. The magnetic radius and the magnetic moment are sensitive to the D state.

In this work two-body direct capture calculations of $^{2}H(n,\gamma)^{3}H$ observables have been performed employing two-body (neutron plus deuteron) projections of the three-body wave functions of Gibson and Lehman (1984). The three-body wave functions were generated from phenomenological nucleon-nucleon potentials via the Faddeev formalism. The following admixtures of states were present in the three-body wave functions: 1) $P_S = 98.26\%$, $P_{S'} = 1.74\%$, and $P_D = 0.00\%$; 2) $P_S = 93.16\%$, $P_{S'} = 1.74\%$, and $P_D = 5.08\%$; and 3) $P_S = 89.08\%$, $P_{S'} = 1.74\%$, and $P_D = 9.12\%$. Lehman performed the overlap integrals necessary to project out the two-body wave functions. The following admixture probabilities, corresponding to the above three cases and renormalized to 1, were present in the projected two-body wave functions: 1) $P_S = 100\%$ and $P_D = 0\%$; 2) $P_S = 98.8\%$ and $P_D = 1.2\%$; and 3) $P_S = 98.5\%$ and $P_D = 1.5\%$.

In addition to the above wave functions, the three-body wave function of Riska (1980) has been employed in this work. Its relatively simple form has been useful in carrying out a complete three-body calculation of the $^{2}H(n,\gamma)^{3}H$ to $^{2}H(p,\gamma)^{3}He$ asymmetry ratio (see §5.4). Riska's wave function contains the features of the Faddeev generated wave functions which are essential to the calculation of the asymmetry ratio (Lehman, 1984). It consists of a dominant $^{2}S_{1/2}$ part with an admixture of $^{4}D_{1/2}$ ($P_D = 8\%$). The S-state is of the Irving form and the D-state is generated from the S-state by first order perturbation theory. Realistic correlations are included in the wave function to

give the right form at small and large distances.

A detailed discussion of direct capture calculations employing the above-mentioned wave functions, and a comparison of theoretical predictions with experimental results, are presented in Chapter 5. A description of the $^{2}H(n,\gamma)^{3}H$ experiment and the data analysis which led to the experimental results are presented next.

2 EXPERIMENTAL TECHNIQUES AND EQUIPMENT

2.1 Introduction

The study of the $^{2}H(n,\gamma)^{3}H$ reaction required a target containing deuterium, a beam of neutrons which could interact with the target nuclei to produce γ-rays, and detectors capable of distinguishing $^{2}H(n,\gamma)^{3}H$ γ-rays from background. The beam of neutrons was produced from accelerated deuterons via the $^{2}H(d,n)^{3}He$ reaction. The equipment and reaction employed to create the neutron beam are discussed in the first part of this chapter. This is followed by a description of the detectors and targets employed in the experiment. Finally, the techniques which yielded the desired spectra (data) are discussed.

2.2 Deuteron Beam Transport and Neutron Beam Production

The $^{2}H(n,\gamma)^{3}H$ experiment was performed at the Triangle Universities Nuclear Laboratory (TUNL) which is schematically represented in Figure 2-1. Negatively charged ions of deuterium were produced by either a direct extraction negative ion source (DENIS I) or a Lamb-shift polarized ion source in order to generate the beams of unpolarized and vector polarized deuterons required for this experiment. The negative ions were transported to the tandem Van de Graaff accelerator with the aid of electrostatic steerers, magnetic steerers and quadrupole focussing magnets. Inside the Van de Graaff the ions were accelerated by the positively charged terminal which is

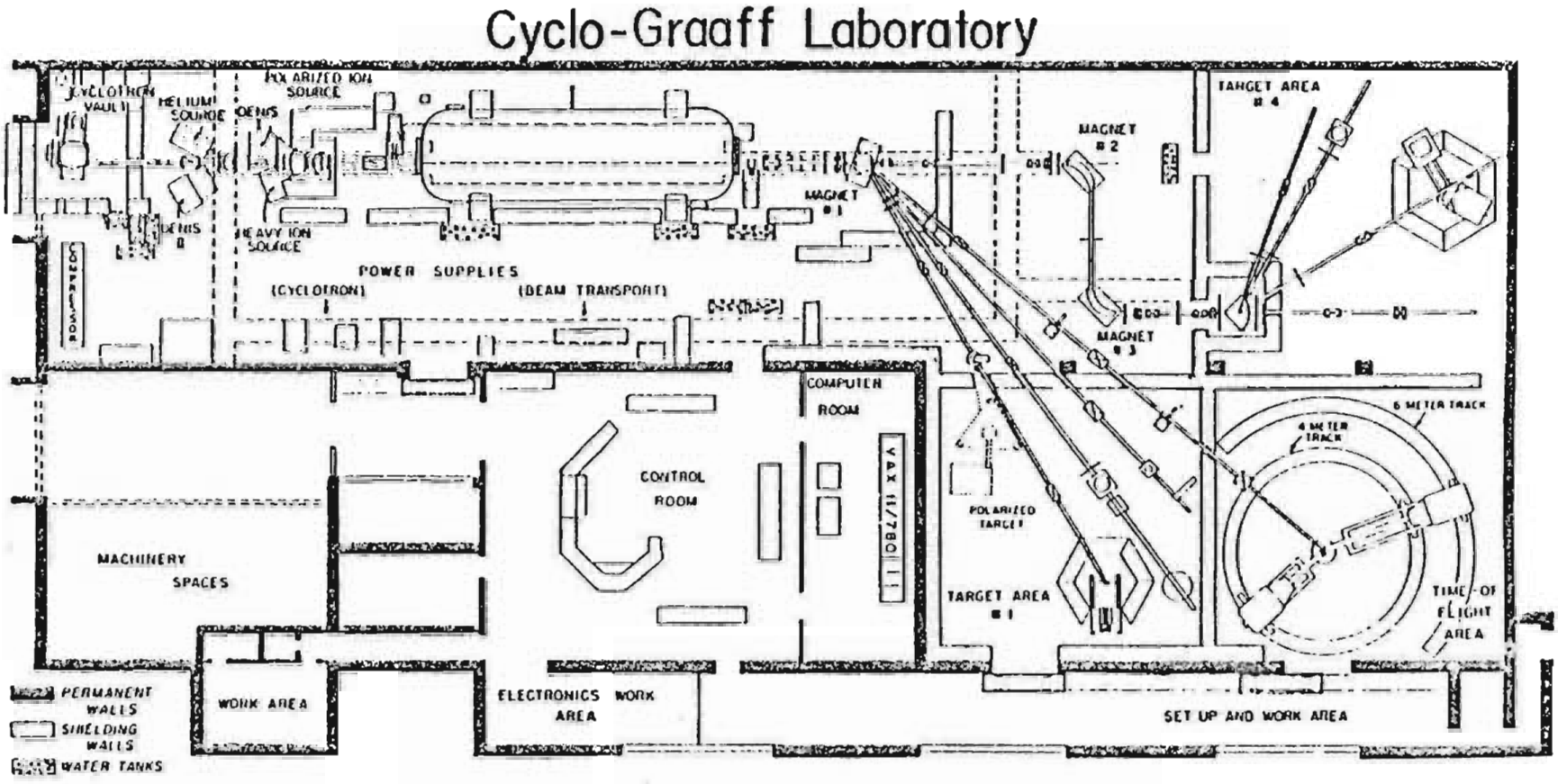

Figure 2-1. TUNL Cyclo-Graaff Laboratory.

capable of sustaining voltages up to 9 MV. Upon reaching the terminal at the center of the accelerator, the ions were stripped of their electrons by a 10 $\mu g/cm^2$ carbon foil. The deuterium nuclei passed through the foil and underwent a repulsive acceleration away from the terminal. The operation and characteristics of the accelerator and ion sources are further described in publications (Newson, 1974; Clegg, 1974).

Upon exiting the accelerator the beam was transported into a system of two 90° analyzing magnets. The energy of the beam was established by adjusting the magnetic fields such that only deuterons of the desired energy could follow a trajectory through the system. Deuterons with greater or lesser energies, and particles with other masses (such as protons), were deflected into the wall of the beam line or into horizontal slits stationed between the magnets. The beam current on the slits was used to generate a feedback signal which provided minor adjustments to the terminal voltage. This stabilized and centered the beam, allowing deuterons with the correct energy to pass through the two magnets.

The beam was then transported to a switching magnet which deflected the deuterons into the 30° beam line of target area #4. This line leads to the target site which was viewed by γ-ray detection equipment. A one inch long gas cell containing deuterium gas, pressurized to either 90.0 or 108.0 psia (see Figure 2-2), was situated at the end of the beam line. The deuteron beam was focussed through a 5.65 mg/cm^2 Havar foil into the gas cell. A tantalum beam stop located

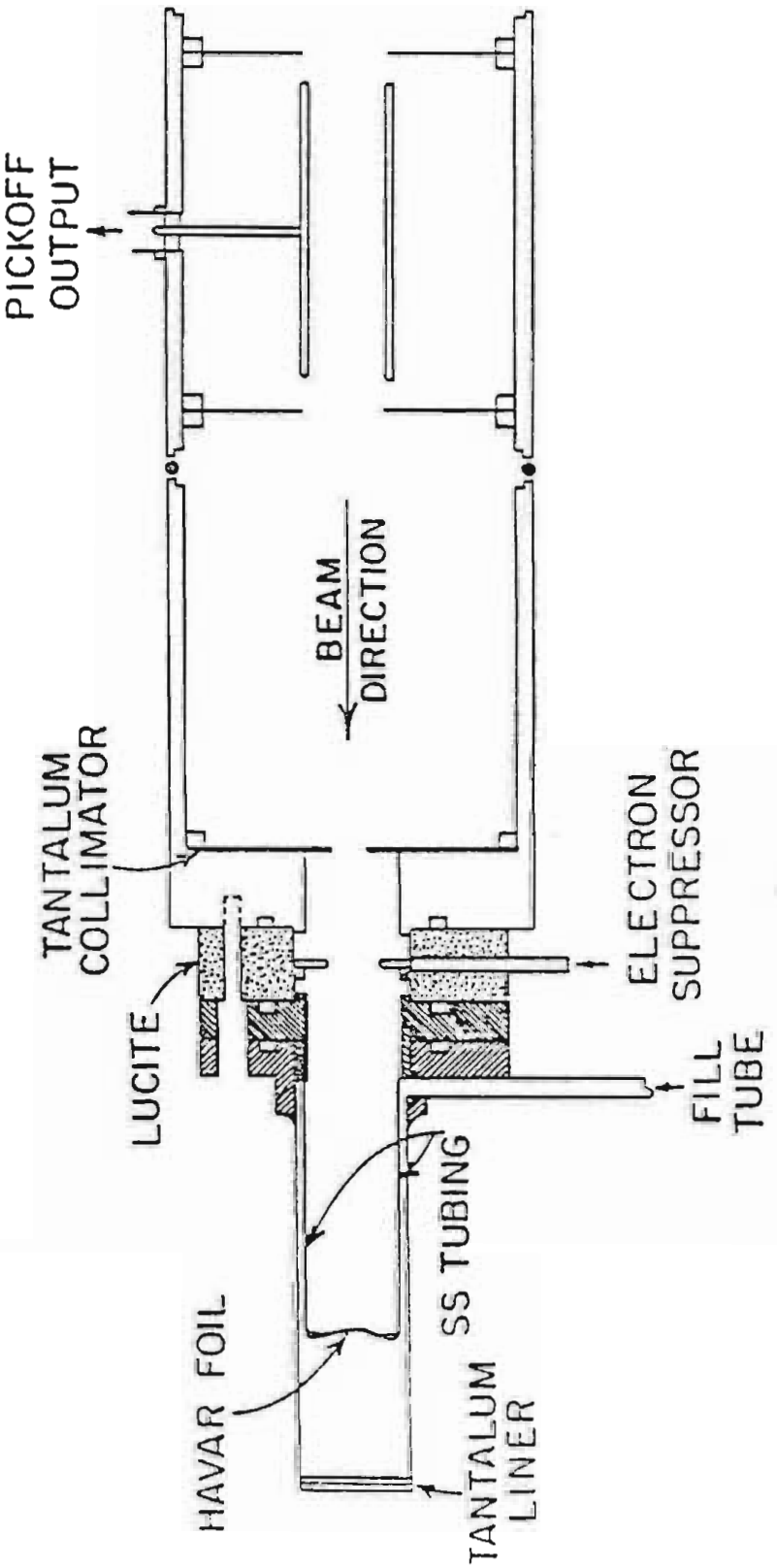

Figure 2-2. Neutron production assembly.

at the end of the cell was used to integrate the beam current in order to determine the number of deuterons passing through the cell. Inside the gas cell neutrons were produced via the $^{2}H(d,n)^{3}He$ reaction. This reaction is suitable for creating an intense, forward-peaked and polarized flux of neutrons. Cross sections for the reaction have been measured by Drösg (1978) and polarization transfer coefficients have been measured by Lisowski et al. (1975).

2.3 Detectors

The capture group at TUNL employs two cylindrical NaI detectors which are 25.4 cm in diameter and 25.4 cm in length. These detectors have an intrinsic efficiency near 100% and a resolution of 3 to 5% for detection of γ-rays in the energy region of this experiment (10.8 to 15.5 MeV). Figure 2-3 displays a top view of the detector geometry as it was arranged in the $^{2}H(n,\gamma)^{3}H$ experiment. An anti-coincidence shield, consisting of Nuclear Enterprises NE110 scintillating plastic (viewed by eight photomultiplier tubes), was used to reject events registered by both the NaI and the shield (Suffert, 1968; Paul, 1974). Passive shielding included 10 cm of lead (to stop γ-rays), 20 cm of paraffin doped with lithium carbonate (to thermalize energetic neutrons), 1.5 cm of sheet-plastic containing boron or 0.15 cm of sheet-metal containing cadmium (to absorb thermal neutrons) and tungsten (to shield the detector from the direct neutron flux emitted from the gas cell). Target-born γ-rays entered the NaI crystal through a hole in the lead specifically designed to illuminate the back face of the

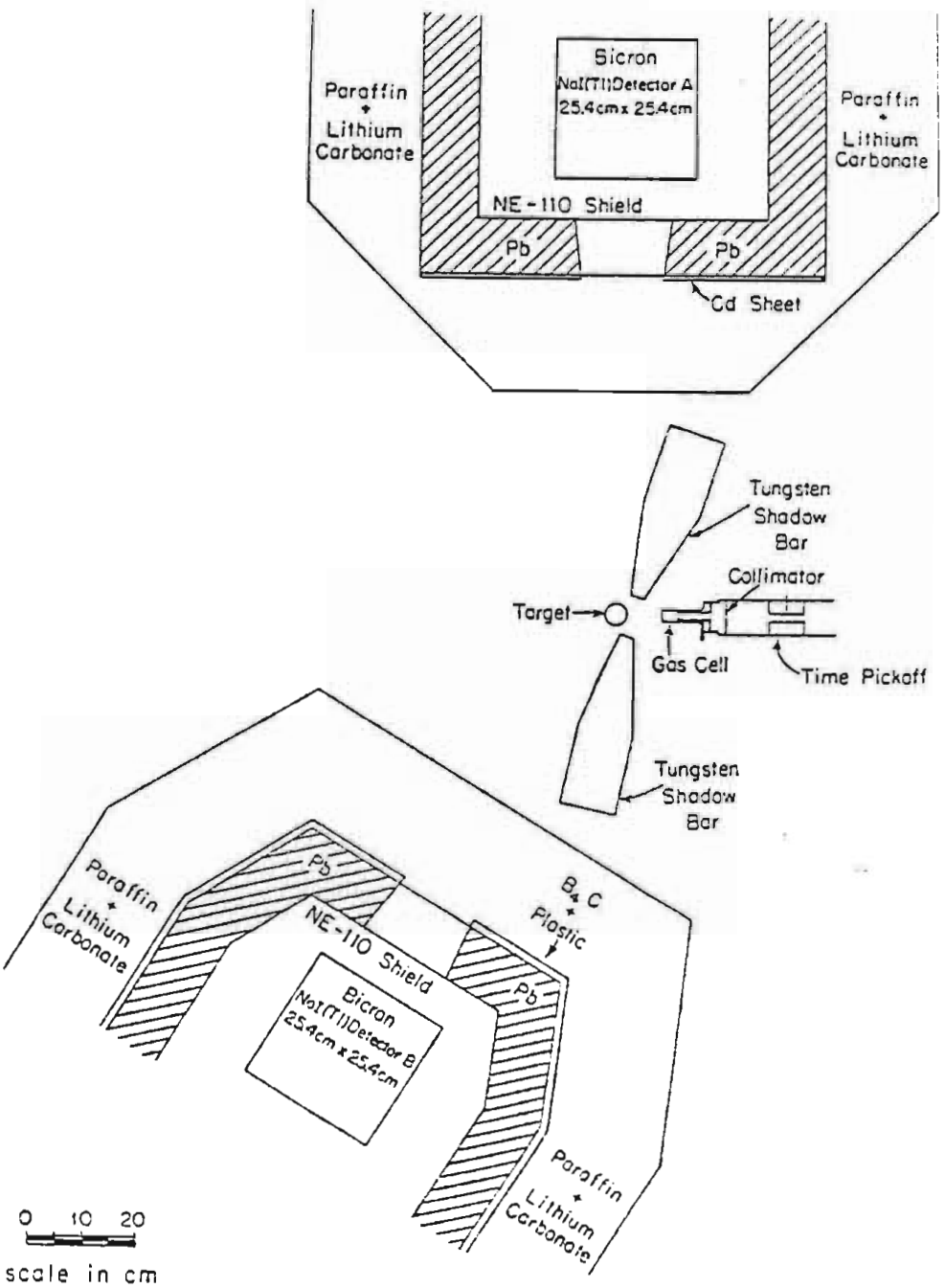

Figure 2-3. NaI detectors, shielding, target, and gas cell.

detector. Coincidence rejection, passive shielding and summing technique (§3.1) yield an effective efficiency for each detector system of approximately 20%. Precise values of the efficiency, as functions of amplifier gains and discriminator thresholds, were determined experimentally (see §4.4 for details).

Ten to fifteen MeV γ-rays interact with the NaI crystal primarily through the process of pair production which creates an electron and a positron. These charged particles radiate away their kinetic energy via bremsstrahlung. Thallium (Tl), a doping element uniformly present throughout the NaI (0.25%), shifts the frequency of the radiation into the optical region for more efficient collection by the six photomultiplier tubes which view the rear face of the crystal. In addition, positron annihilation creates a pair of 0.511 MeV photons, one or both of which may or may not escape the detector, the deposited energy being converted to light and collected. The output pulse for a γ-ray is linearly proportional to the energy deposited in the crystal in the energy region of this experiment. Nonlinearity of the light output from the crystal occurs for γ-rays of energy greater than 80 MeV, while nonlinearity due to saturation of the photomultiplier tubes occurs in the 40 to 60 MeV range depending on the applied high voltage (Weller, 1984).

Signals from the NaI detectors and plastic shields were shaped and timed by electronics modules and sent to a VAX 11/780 computer for processing. A brief description of the standard capture-group electronics, accompanied by a block diagram of the circuits, is

presented in Appendix A. Further information about the spectrometer system and associated electronics is available (Weller, 1981) and similarly for the computer and data aquisition software (King, 1981; Gould, 1981; Roberson, 1981; Holzsweig, 1981; Gould, 1983). A detailed discussion of the electronics which is unique to this coincidence experiment is forthcoming in this chapter.

2.4 Targets

The difficulty in the thesis experiment was that the standard experimental set-up was incapable of clearly distinguishing $^{2}H(n,\gamma)^{3}H$ capture γ-rays from other γ-rays. Two different approaches, employing two different targets, were used to make measurements in this neutron capture experiment. One technique exploited the kinematics of the $^{2}H(n,\gamma)^{3}H$ reaction and pulsed beam in order to extract the data from the background. The second employed a scintillating target to substantially reduce background through the use of a coincidence requirement.

A sample of deuterium oxide (heavy water) purified to 99.75% was initially used as a target in the experiment. Although it was felt that this experimental approach was not good enough to yield a systematic study of the $^{2}H(n,\gamma)^{3}H$ reaction (see below), it would provide a cross section measurement, under well established experimental conditions, to be used to compare with results from the scintillating target. The heavy water was placed in a cylindrical thin-walled glass container and hung with its axis 8.89 cm from the center of the deuterium gas cell.

At a neutron lab energy of E_n = 14.0 MeV the kinematics of the $^2H(n,\gamma)^3H$ reaction are such that the energy of the desired γ-rays places the peak in the 2.19 MeV gap between $^{16}O(n,\gamma)^{17}O$ γ-ray transitions to the first and second excited states of ^{17}O (see Figure 2-4). Furthermore, by using a target of ordinary distilled water, it was possible to measure the background under the data due to the tails of the oxygen peaks. The spectra of Figure 2-4 were obtained by employing a polarized beam pulsed at 4 MHz, with deuteron packets of full width at half maximum (FWHM) typically 2 ns (Wender, 1980). The beam pulsing was instrumental in eliminating fast-neutron related background. Since the time-of-flight of neutrons scattered from the target into the NaI detector was greater than the time-of-flight of γ-rays emerging from the target, electronic gating was employed to accept data only when γ-ray bursts struck the detector.

Although we were fortunate enough to obtain data under the described conditions, there were several severe limitations to this approach. First of all, at forward angles less than 65^o the tungsten shadow bar could not prevent the direct neutron flux of the gas cell from hitting the shielding around the NaI crystal and scattering into the detector itself. This increased the number of low energy γ-rays resulting from thermal neutron capture in the crystal and created an intolerable amount of pile-up in the energy region of the $^2H(n,\gamma)^3H$ data (i.e. when two or more pulses are not sufficiently separated in time, they add together to create a larger pulse (Paul, 1974)). Secondly, energy dependent effects of the $^2H(n,\gamma)^3H$ reaction would be difficult to

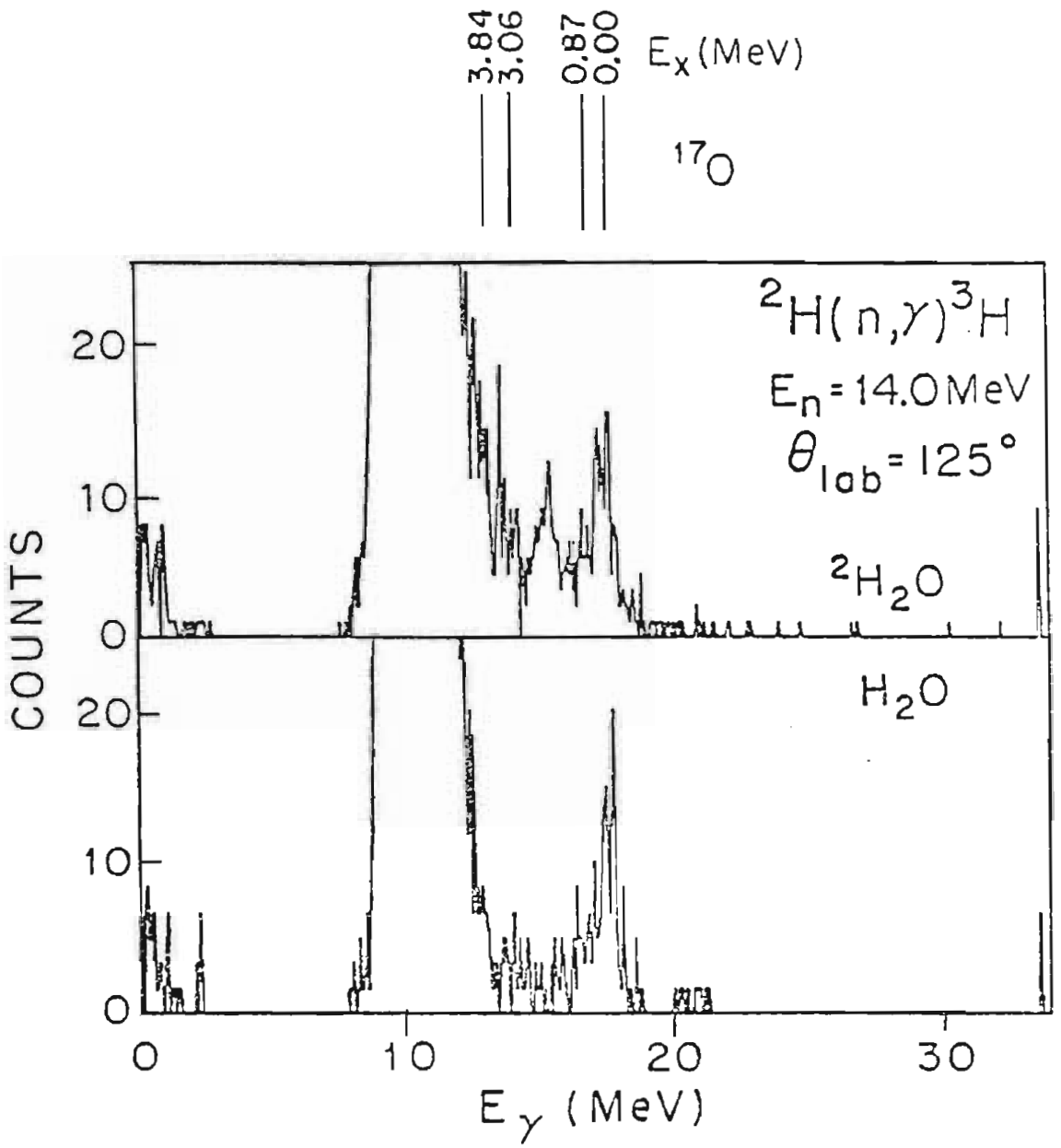

Figure 2-4. Heavy water and distilled water spectra.

study because a well resolved peak was available only at a neutron bombarding energy of 14.0 MeV. At lower energies the desired γ-rays overlapped γ-rays to the ground and first excited states of ^{17}O. At higher energies there was overlap with γ-rays to higher excited states of ^{17}O, in addition to greater pile-up background. Finally, the malady of low counting rate was suffered due to two necessary experimental conditions. The detectors were placed as far away as possible from the gas cell (and consequently the target) to reduce background, resulting in a detection solid angle which was approximately half of that of the standard position. Also, 40% of the available beam time was spent measuring the background, instead of "true data", in order to be able to accurately subtract the oxygen counts from the data. Considering all these limitations an alternative target was obtained to improve our measurement capabilities.

A deuterated liquid scintillator produced by Nuclear Enterprises, NE232, has been employed in the $^{2}H(n,\gamma)^{3}H$ experiment. The virtue of employing a scintillating target is that one can substantially reduce background by a coincidence requirement. To each γ-ray resulting from a $^{2}H(n,\gamma)^{3}H$ reaction there corresponds a recoiling ^{3}H nucleus in the target. If the target is a scintillator, the recoiling triton generates a signal which can be constructively employed. Background is substantially reduced by restricting the acceptance of data to events which generate both a NaI and an NE232 signal. Background cannot be completely eliminated because the finite duration of signals gives rise to accidental coincidences. These must be corrected for in the data

analysis.

The chemical formula of cyclohexane-based NE232 is C_6D_{12} with an actual deuterium to carbon ratio of 1.96 (the remainder being mainly hydrogen atoms). Its density and volume are specified as 0.89 gm/cm^3 and 45 cm^3 respectively. The outer dimensions of the cylindrically-shaped glass container are 3.70 cm diameter and 4.18 cm length. There exists a protruding expansion vessel containing nitrogen gas. The scintillator was optically coupled to a lucite light pipe which was also optically coupled to an RCA 8575 photomultiplier tube (see Figure 2-5). The reasons for employing a light pipe were to displace the photomultiplier away from the direct flux of neutrons emerging from the gas cell and to enable a fiber-optic cable to be attached so that light from a light emitting diode (LED) could be pulsed into the photomultiplier. The important role of the LED was to generate a constant energy signal which could be used to monitor the gain stability of the photomultiplier and attached base. The axis of the scintillator was placed 8.89 cm from the center of the neutron-producing gas cell.

Events in the NE232 scintillator were primarily neutrons interacting with ^2H and ^{12}C. The recoils from these interactions lost energy through ionization. Light was consequently emitted when electrons filled vacated atomic orbitals. Since a heavy element such as Tl was not present to shift the frequency of the light into the visible region, and since the collection time of NE232 is shorter than that of NaI, the light output

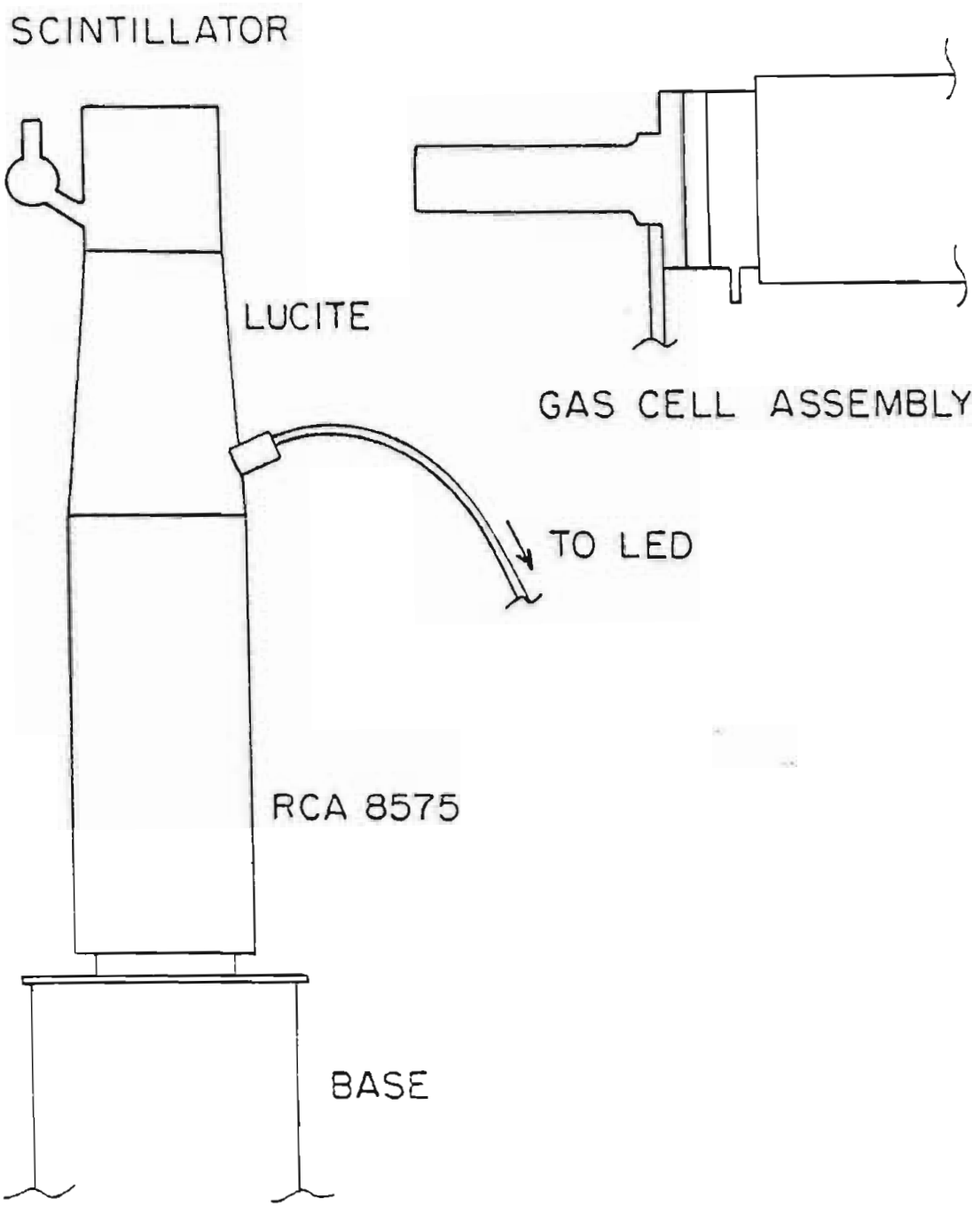

Figure 2-5. Scintillating target assembly.

from the scintillator is relatively small. Unlike the NaI detector, the light output from NE232 is not linear with energy (Bertl, 1972; Mitev, 1984; Birks, 1964).

2.5 Coincidence Electronics and TAC Spectra

A block diagram of the electronics employed to identify coincident events between the NaI detector and the scintillating target is displayed in Figure 2-6. Light from an event occurring in the NaI crystal was collected by six RCA 8575 photomultiplier tubes which were coupled to special high-current transistorized bases. These bases were designed to optimize gain stability under high count-rate and variable count-rate conditions (Turner, 1978). The photomultiplier-base pairs were carefully gain matched by adjustments to the applied high voltage. The anode signals emerging from the bases were mixed to form one pulse which was subsequently amplified, passed through a differential discriminator (which fired only on pulses greater than the selected threshold level) and routed to the start input of a time-to-analog converter (TAC). Similarly, the pulses from the scintillator were amplified, passed through a constant fraction discriminator and routed to the stop of the TAC. The importance of gain stability is evident from this block diagram. If the gain of the NaI or NE232 signals were to decrease, pulses corresponding to desired data could be stopped by the discriminators in the circuit. The gain stability of the NaI electronics is excellent at the low γ-ray count-rates typical of this experiment and was not a problem. This was not true in the case of the

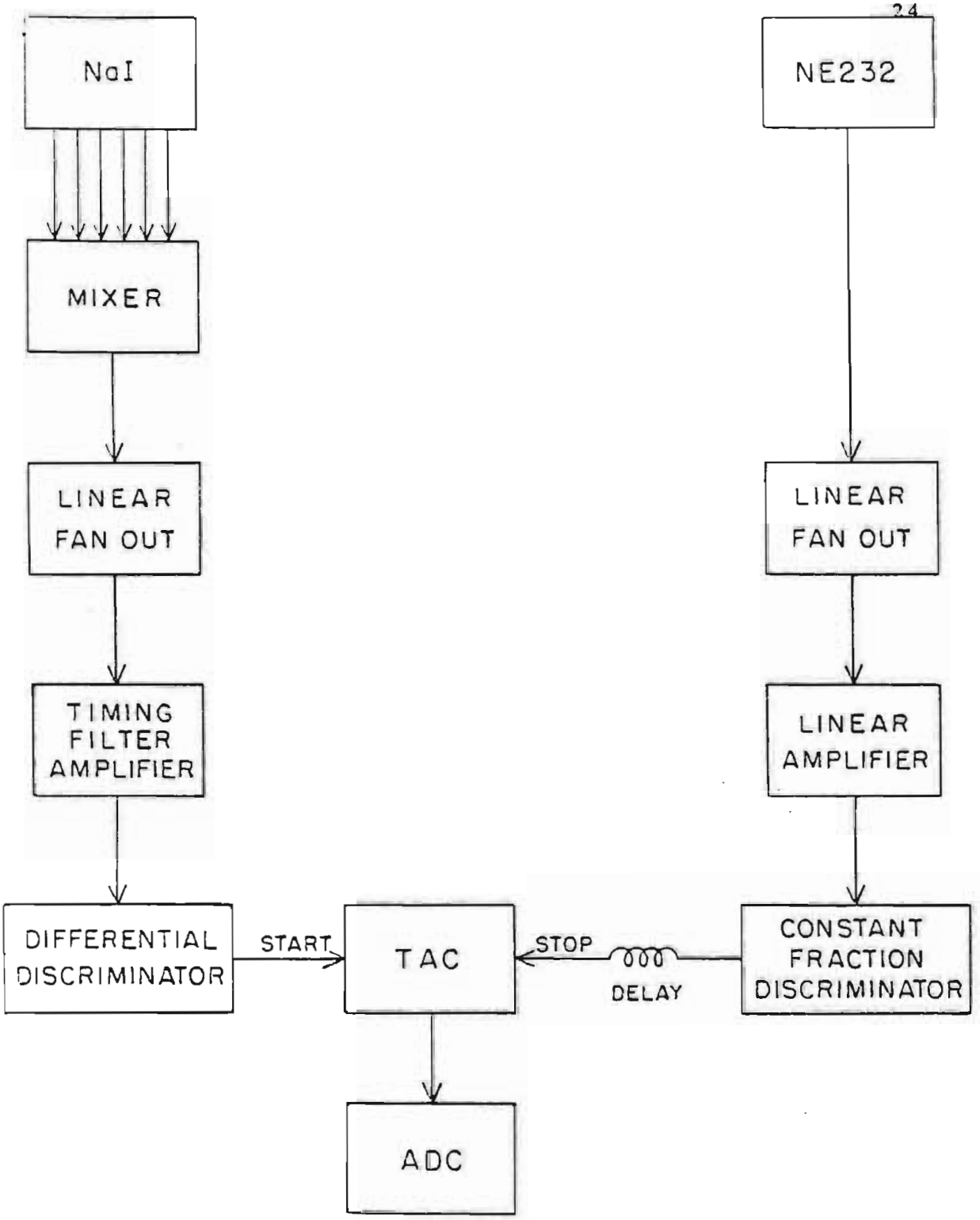

Figure 2-6. Coincidence electronics between detector and target.

scintillator electronics. By storing an LED generated signal of constant amplitude, a gradual deterioration of the gain was observed (down about 10% per day). This loss was traced to the photomultiplier-base assembly and corrected for by regularly increasing the applied high voltage. The choice of which signals to use as starts or stops to the TAC was based on the count-rates from the discriminators which were typically 12 Hz for NaI pulses and 0.5 MHz for scintillator pulses, depending on beam current and energy. The output of the TAC was digitized by an analog-to-digital converter (ADC) and stored in the computer.

When uncorrelated events trigger the start and stop of the TAC, the time between them is random and the output of the TAC resembles a flat background extending throughout the spectrum. However, if the triggering pulses are correlated, the time separation is constant and a spike should appear in the TAC spectrum. It is important to recognize what kind of events occurring in the target can give rise to coincidences (see Figure 2-7): (1) Desired γ-rays from $^{2}H(n,\gamma)^{3}H$ are in coincidence with the recoiling tritons; (2) γ-rays from neutron capture to states in ^{13}C (i.e. $^{12}C(n,\gamma)^{13}C$) are in coincidence with the recoiling ^{13}C nuclei; (3) γ-rays from inelastic neutron scattering off of ^{12}C are in coincidence with ^{2}H or ^{12}C recoils which the neutrons may strike after the initial scattering; and (4) neutrons which scatter into the NaI detector off of ^{2}H or ^{12}C nuclei are in coincidence with those recoils. Some of these processes were observed in the data and some were not.

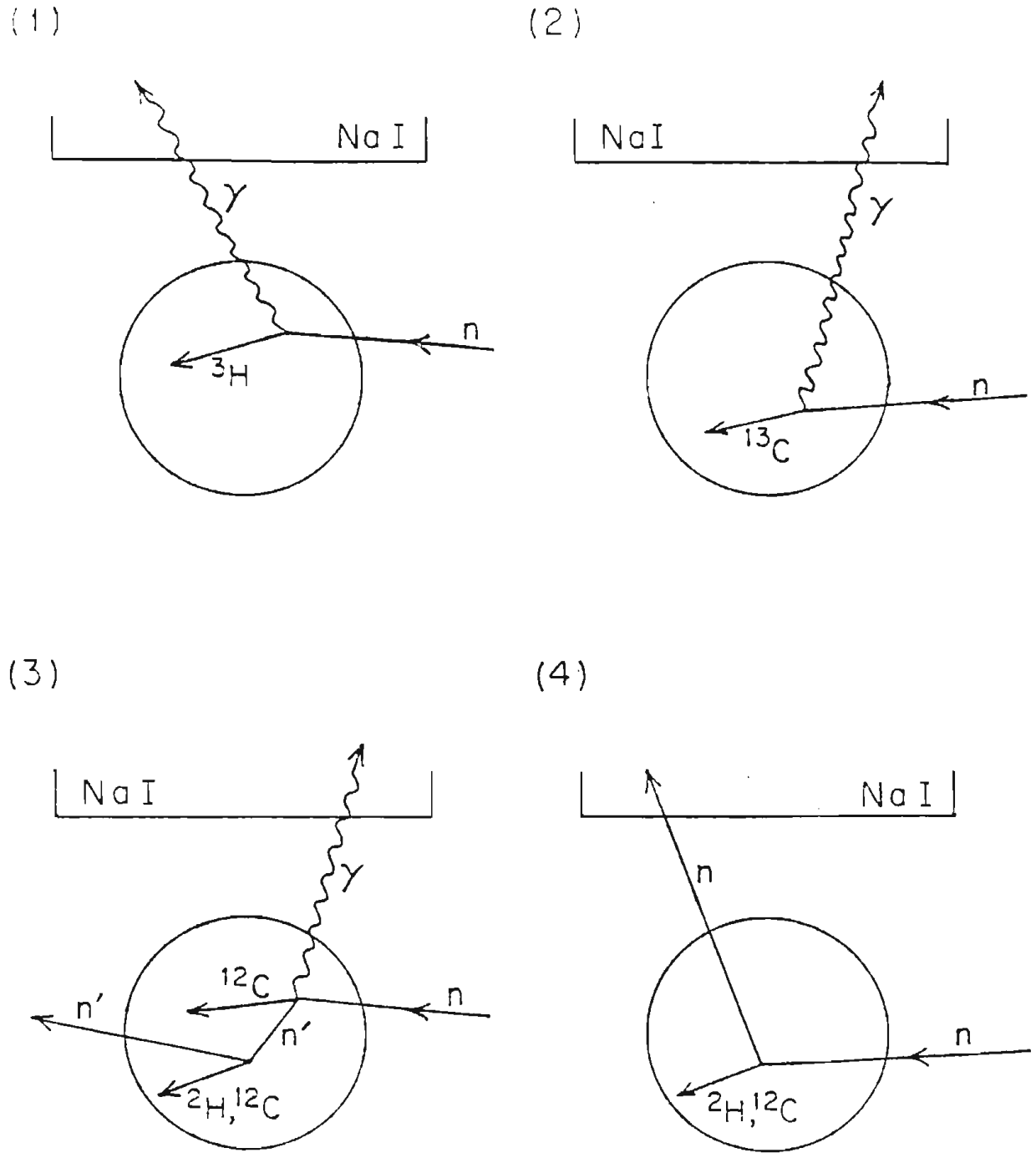

Figure 2-7. Coincidence events.

Coincidences involving carbon recoils were not seen in any spectra because the carbon recoils did not generate large enough pulses to pass through the scintillator discriminator. This is not surprising. A calculation of light output for carbon recoils (L_c) relative to triton recoils (L_t) has been performed employing the semi-empirical equation

$$2\text{-}1 \qquad L(E) = S \int_0^E \frac{d\varepsilon}{1 + kB \frac{dE}{dx}(\varepsilon) + C \left[\frac{dE}{dx}(\varepsilon)\right]^2},$$

which is derived from the theoretical work of Birks (1951, 1964), Wright (1953) and Chou (1952). In Equation 2-1 L(E) is the light emitted by the particle of incident energy E, dE/dx is the specific energy loss for the charged particle (a function of particle type and energy ε), S is the scintillation efficiency, and kB and C are adjustable parameters. The values of Craun and Smith (1970) were employed for the parameters kB and C. These values have been shown to work well in a calculation of light output for tritons relative to deuterons in NE232 (Mitev, 1984). The result of the calculation was $L_c = 10^{-4} L_t$, well below the discriminator threshold which was at approximately 0.5 L_t.

Inelastic neutron scattering off of ^{12}C produces an intense 4.44 MeV γ-ray transition from the first excited state to the ground state. Recall that inelastic neutrons may rescatter off of deuterons, hence this coincidence is observable. The TAC spectrum of Figure 2-8 represents 12 minutes of data aquisition and the large peak illustrates this coincidence. Note that the time scale is backwards. This is because the start signal to the TAC from the NaI detector in reality

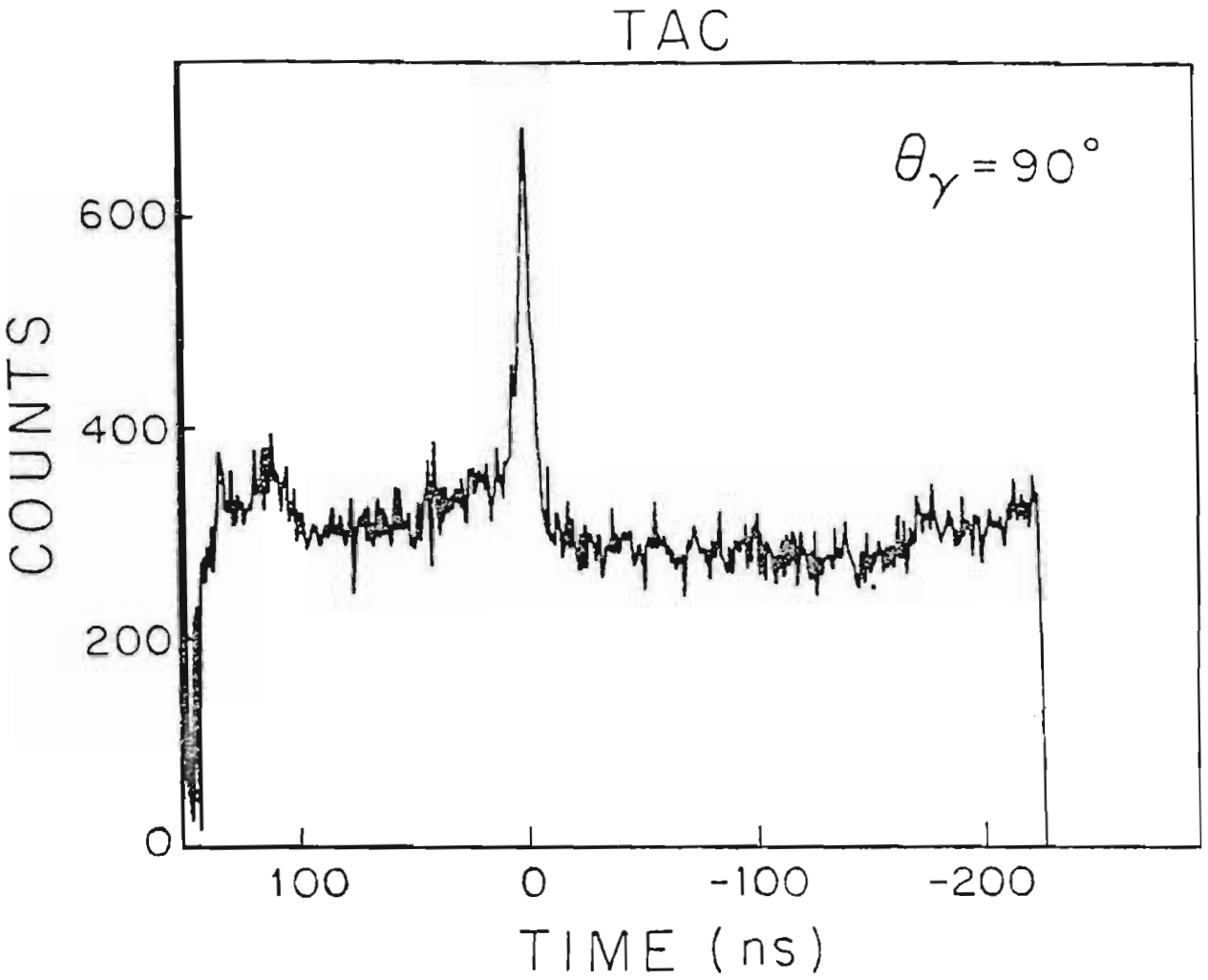

Figure 2-8. TAC spectrum at E_n = 9.0 MeV. The peak at TIME = 0 corresponds to coincidences between $^{12}C(n,n'\gamma)^{12}C$ γ-rays detected in NaI and recoiling deuterons in NE232 which have been struck by n' neutrons.

occurs later than the delayed stop signal from the target, turning shorter time differences into larger output pulses. The time calibration was measured by routing delayed start pulses into the stop of the TAC, creating a sharp coincidence spike in the spectrum. Varying the amount of delay by a known value determined the calibration.

Observing $^{2}H(n,\gamma)^{3}H$ coincidences in the presence of the $^{12}C(n,n'\gamma)^{12}C$ coincidences would be impossible since their respective timings are approximately equal (i.e. they overlap within the resolution of the TAC). This was not a problem, though, because the NaI discriminator threshold was set well above 4.44 MeV. However, due to the low counting rate of the experiment, the $^{2}H(n,\gamma)^{3}H$ TAC peak was still buried in the flat background of random events. It was necessary to impose a condition on the TAC spectrum in order to reveal the desired peak. Since each event stored in the computer had associated with it both time and energy information (see Appendix A), it was possible to store a TAC spectrum resulting from γ-rays in a particular energy range. A full TAC and its energy-gated part, accumulated for about an hour at γ-ray detection angles of 122.8° and 70°, are displayed in Figure 2-9. The energy gating extracts a clearly visible peak corresponding to $^{2}H(n,\gamma)^{3}H$ coincidences. This peak is present in the full TAC, but is almost indistinguishable from the background. The resolution of the coincidence spike was typically 0.5% to 1.0% (2 to 4 ns FWHM on a full scale of 400 ns).

The 70° E-gated TAC spectrum of Figure 2-9 also displays a broader peak at TIME = +35 ns. This corresponds to neutrons which scattered

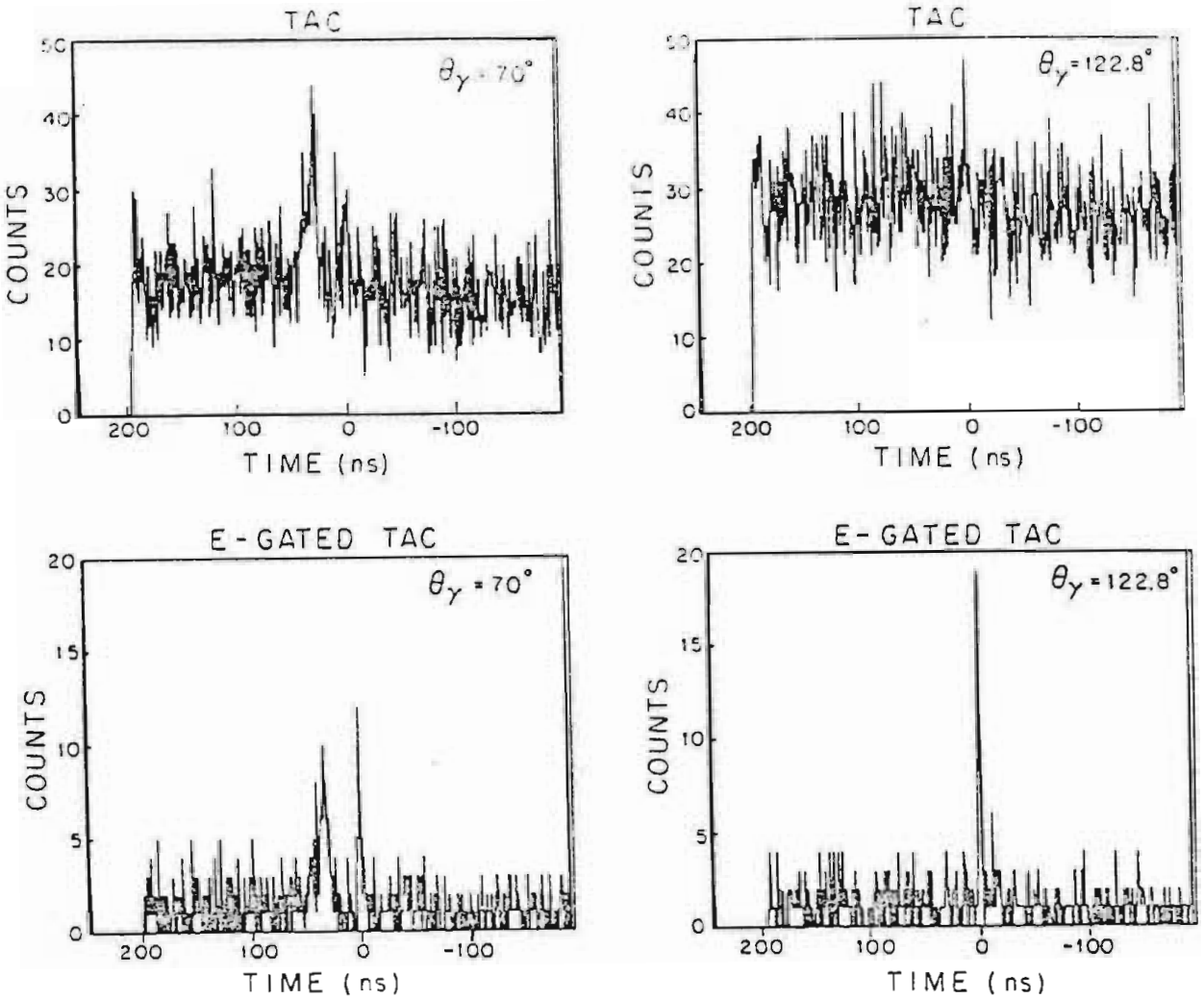

Figure 2-9. Full and energy-gated TAC spectra at lab detection angles of 70° and 122.8°. The energy-gated spectra display a sharp peak at TIME = 0 corresponding to coincidences between γ-rays and tritons from the $^{2}H(n,\gamma)^{3}H$ reaction at E_n = 9.0 MeV.

elastically from deuterons in the target, were thermalized in paraffin and were captured by the NaI crystal. The resulting capture γ-rays were in coincidence with the recoiling deuterons in the NE232 scintillator. The width of the peak results from kinematic energy spreads in the scattering processes. Because an elastically scattered neutron retains most of its energy only at forward laboratory angles (a kinematic effect), the coincidence peak at TIME = +35 ns was not visible at the detection angle of 122.8°.

2.6 Energy Spectra

Examples of the types of γ-ray spectra acquired will illustrate some of the γ-ray production processes present in the experiment and also demonstrate the importance of coincidence gating. The top spectrum of Figure 2-10 displays the γ-rays detected by the NaI crystal above a relatively low discriminator threshold. Outstanding features are the two strong lines at 4.44 MeV and 6.83 MeV (from inelastic neutron scattering off of ^{12}C in the target and from thermal neutron capture by ^{127}I within the detector itself) and a spike at the far right due to saturation of the spectroscopy amplifier (from γ-rays and cosmic-rays of energy greater than 14.5 MeV). Shown also in the figure is the energy spectrum obtained by accepting only data within the narrow window of the TAC spectrum. Note that the peak at 6.83 MeV, which can have only accidental coincidences with the target, is almost completely missing, while the 4.44 MeV γ-rays from the scintillator are still present. The number of 4.44 MeV γ-rays in the bottom spectrum is less than the number

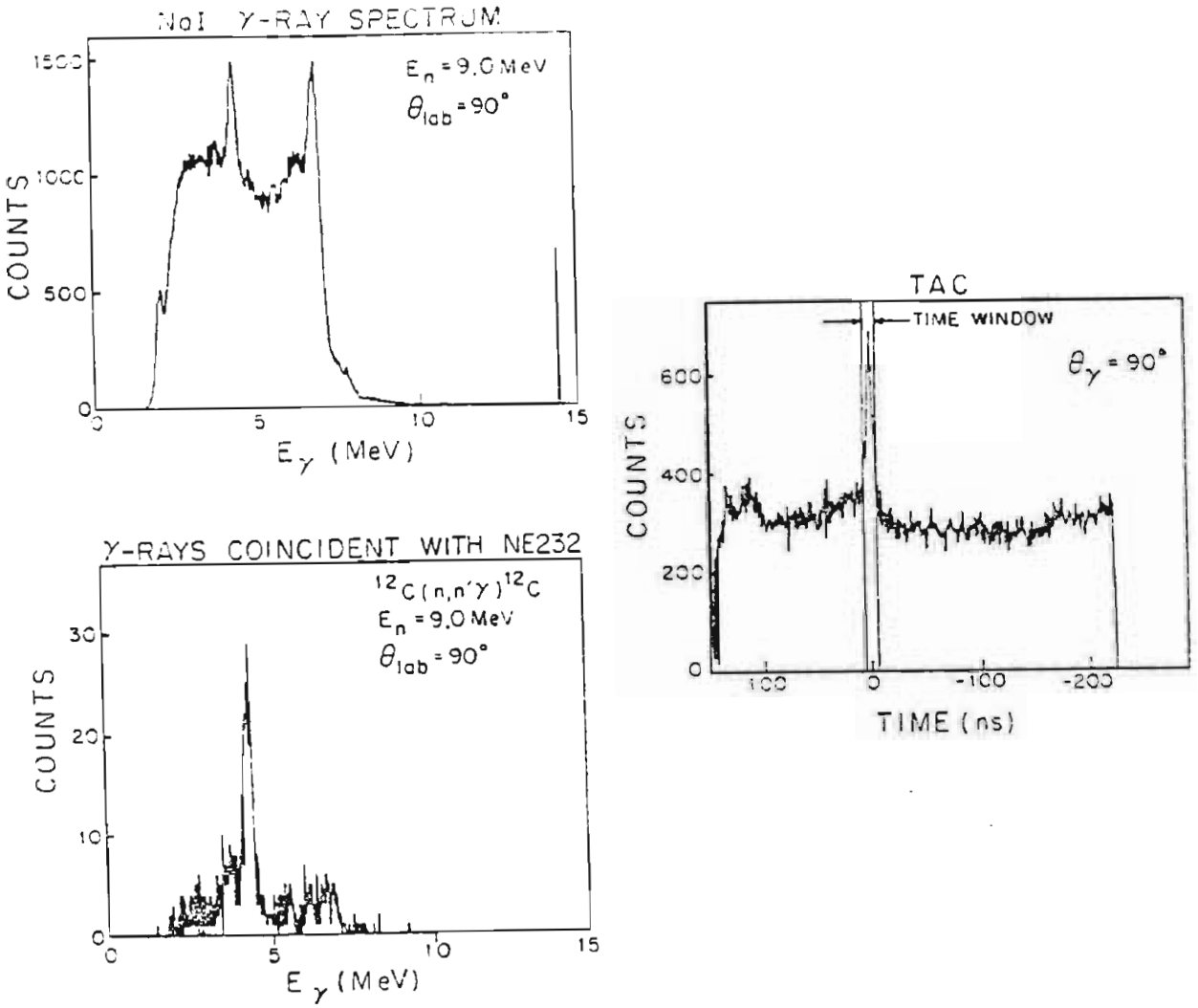

Figure 2-10. Energy and time spectra. When the top γ-ray energy spectrum is gated by the time window displayed in the TAC, the bottom spectrum results. The 4.44 MeV γ-rays from $^{12}C(n,n'\gamma)^{12}C$ are coincident with the target but 6.83 MeV γ-rays from $^{127}I(n,\gamma)^{128}I$ are not.

in the top spectrum. This is because the $^{12}C(n,n'\gamma)^{12}C$ scattered neutron must rescatter from a deuteron in order to generate a signal from the target.

A pair of γ-ray spectra, acquired over a period of 5.5 hours, are displayed in Figure 2-11. The bottom one is restricted to events within the TAC gate. Comparing these spectra shows the stunning effect of the coincidence requirement in extracting the $^{2}H(n,\gamma)^{3}H$ data (at 12.1 MeV) from the tremendous background. The apparent peak near 9 MeV is the result of the discriminator threshold cutting into the huge background. It should be recognized that the scintillating target was the key ingredient to the success of this experiment. Details about extracting sums and backgrounds from the spectra are discussed in Chapter 3.

In addition to γ-ray energy spectra, scintillator energy spectra have been stored in the computer. A block diagram of the electronics employed to process the energy signal from the target scintillator is shown in Figure 2-12. The primary reason for storing an energy spectrum from the scintillator was to witness the recoiling tritons from the $^{2}H(n,\gamma)^{3}H$ reaction (a fact which would confirm that the correct γ-rays were being detected by the NaI crystal). One difficulty encountered was that the tremendously large event-rate in the target caused intolerable ADC dead time in the absence of gating. This problem was solved by using the output pulses of the NaI discriminator to gate the scintillator energy signals. Since to each recoiling triton there was a corresponding coincident γ-ray, this gating reduced the count-rate into the ADC without losing triton recoil pulses. A second reason for

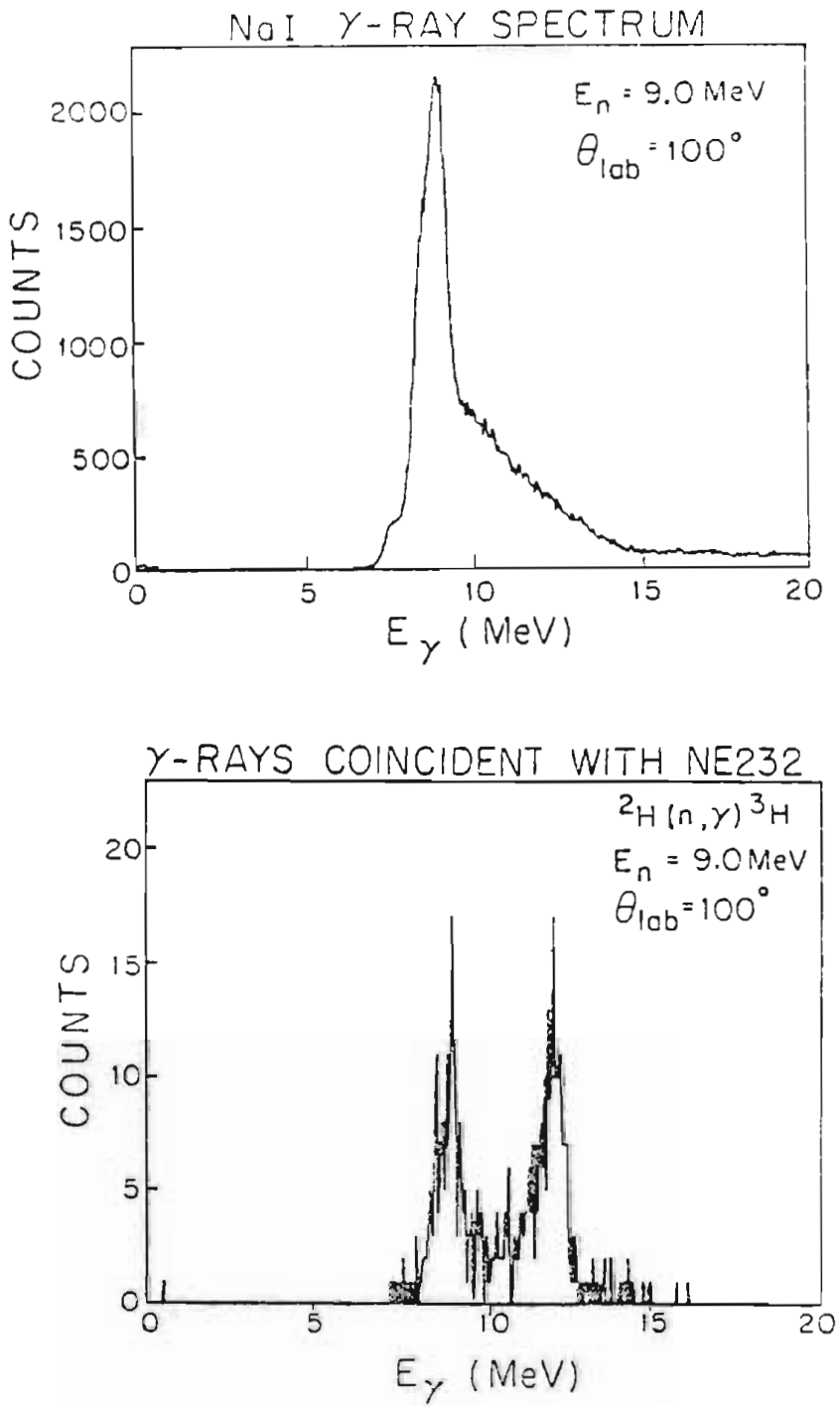

Figure 2-11. NaI energy spectra. When the top γ-ray spectrum is gated by a narrow time window containing the $^2H(n,\gamma)^3H$ coincidence, the 12.1 MeV $^2H(n,\gamma)^3H$ γ-rays are extracted from the large background.

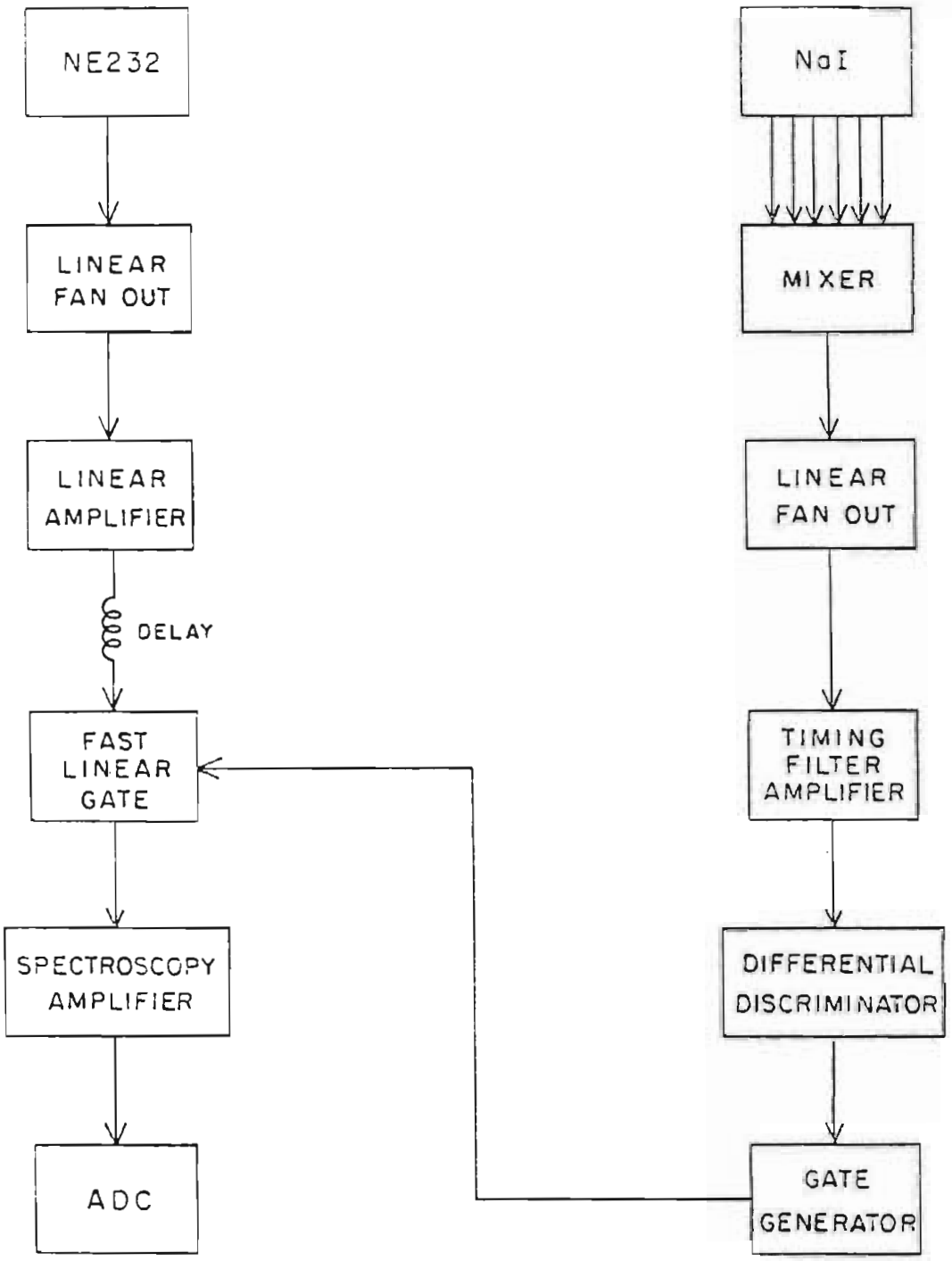

Figure 2-12. Electronics for storing scintillator energy signals.

storing an energy spectrum was to monitor the gain stability of the scintillator electronics. The LED connected to the lucite light pipe was used to pulse light into the photomultiplier tube. Although not shown in Figure 2-12, the SYNC output of the pulser module could be used to generate a gate to pass LED signals through the fast linear gate. A few times each day data were taken under these conditions and slight gain deterioration was observed. The gain was restored by increasing the voltage applied to the photomultiplier tube.

Consider now what should be seen in the scintillator spectrum. Recall that carbon recoils have insufficiently large light output to generate a pulse which will pass through the constant fraction discriminator. It is expected then that neutrons scattering off of deuterons and neutrons capturing into tritons will account for the observed data. At the top of Figure 2-13 is the energy spectrum stored with the circuit of Figure 2-12. The edge in the vicinity of channel 400 corresponds to deuterons which have the maximum possible recoil energy. Kinematics calculations indicate that the range of deuteron energies is 0 to 6.1 MeV for a neutron bombarding energy of 6.85 MeV. By sorting scintillator events in coincidence only with $^{2}H(n,\gamma)^{3}H$ capture γ-rays, the bottom spectrum is obtained. The relatively few triton recoils are extracted from the many pulses in the scintillator and form a well defined peak. Angular distributions measured at E_n = 9.0 MeV and 10.8 MeV displayed the expected kinematic energy shifts for both the γ-ray and triton peaks, a significant result. Finally, it was possible to calibrate the scintillator spectra (based on the triton

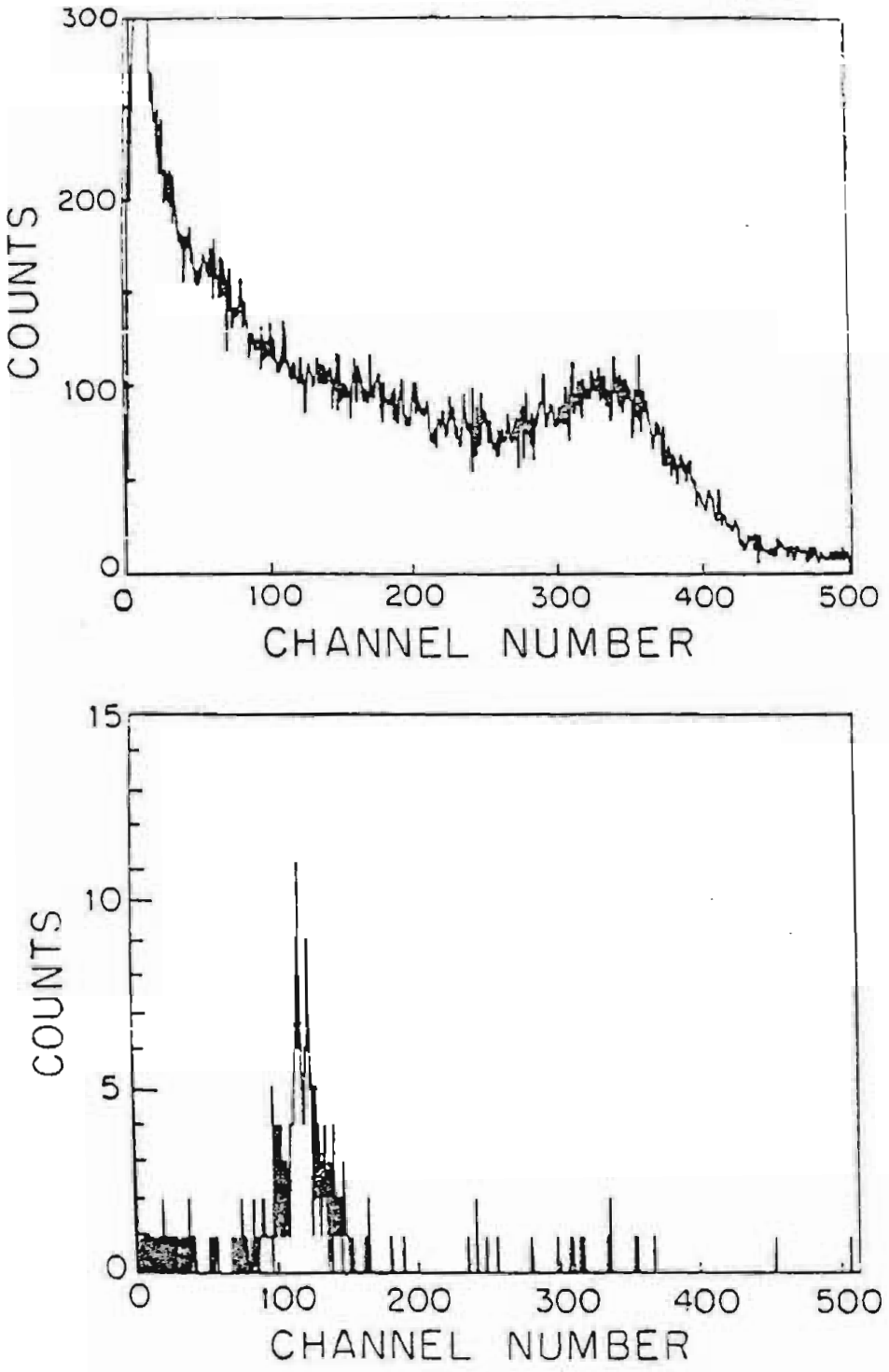

Figure 2-13. NE232 energy spectra at E_n = 6.85 MeV. The top spectrum is predominantly deuteron recoils. A coincidence requirement with $^{2}H(n,\gamma)^{3}H$ γ-rays extracts the triton recoil peak in the vicinity of channel 110.

energy shifts), thus determining the light output of tritons relative to deuterons in NE232 (Mitev, 1984).

3 DATA REDUCTION

3.1 Summing Region

Choosing the summing region in a measured γ-ray spectrum requires consistency with the method employed in the experimental determination of the detector efficiency. The adopted practice has been to sum an isolated γ-ray line from two widths below the centroid of the peak to just above the high energy edge of the peak. What is meant by a "width" is the full width at half maximum (FWHM) of the peak.

Recall the bottom spectrum of Figure 2-11. How would one decide what the width of the $^{2}H(n,\gamma)^{3}H$ peak is? In capture experiments with greater γ-ray yields it has been possible to fit the data to an experimentally determined response function which depends on the width, height and centroid of the peak (King, 1983; Weller, 1981). In general, at least 400 counts in the peak are necessary before statistical fluctuations diminish sufficiently to allow reliable determination of the peak's width, a luxury not available in the $^{2}H(n,\gamma)^{3}H$ experiment. Instead, FWHM has been calculated from the percent resolution of the detector system,

$$R(\%) = 100\,\frac{FWHM(MeV)}{E_{\gamma}(MeV)}, \tag{3-1}$$

which was measured at several γ-ray energies using a variety of (p,γ) reactions (see Figure 3-1). The equation of the linear fit to the data of Figure 3-1 is

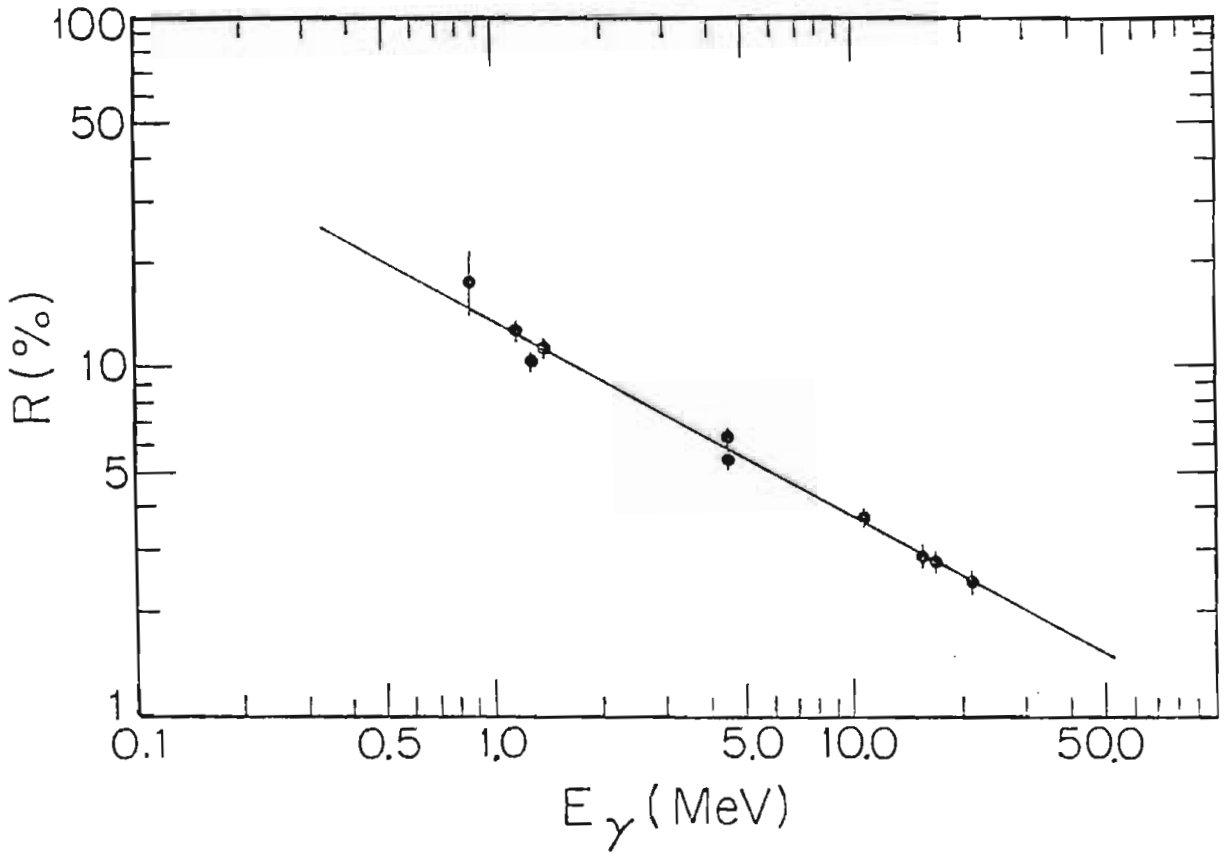

Figure 3-1. NaI detector resolution. The error bars reflect statistical uncertainties in the widths of γ-ray peaks resulting from line-shape fits to the spectra. The line is an eye-fit to the data.

3-2 $$\log(R) = 1.130 - 0.565 \log(E_\gamma).$$

In order to obtain a summing region in channels, an energy calibration was needed to convert FWHM from MeV to channels. The 4.44 MeV γ-ray from ^{12}C and the $^{2}H(n,\gamma)^{3}H$ γ-ray were used as reference points. Additional reference points were made available from angular distribution measurements because the $^{2}H(n,\gamma)^{3}H$ γ-ray was subject to kinematic energy shifts. In that case a linear least squares fit was applied to determine the energy calibration. A typical summing region, calculated in the described manner, is displayed in Figure 3-2.

It should be mentioned at this point that the resolution data of Figure 3-1 were measured for the right detector only. The left detector system, which has been in use for a shorter period of time, has not displayed the stability (in terms of efficiency and resolution) of the older system. Hence the practice has been to adjust, whenever necessary, the voltages and gains of the left detector system to produce equal counting rates in both detectors. Had it been necessary, the left detector sums in this experiment would have been normalized to those of the right detector. However, the results listed in the tables of §3.5 indicate that the two detectors agreed with each other to within statistical uncertainty and that the left detector was not consistently lower or higher than the right one.

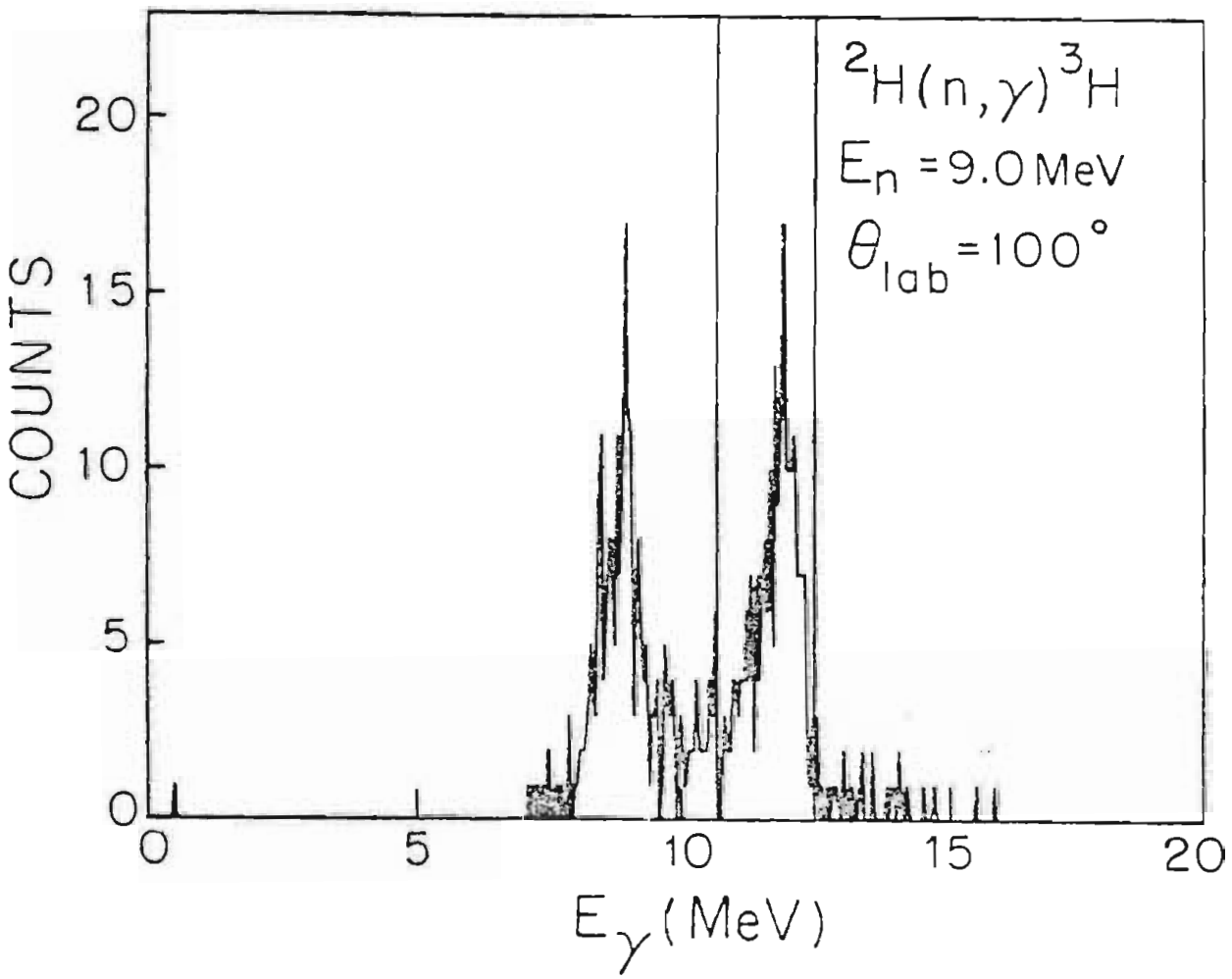

Figure 3-2. Summing region for $^2H(n,\gamma)^3H$ data.

3.2 Background Measurement

In the limit of infinitely fine resolution, a coincidence experiment would yield a spectrum with only the desired data present. In the real world, finite duration of pulses combined with large counting rates can produce accidental coincidences which create unwanted background counts. A significant feature of this coincidence experiment, which was performed using a dc (i.e. constant) beam, is that it was possible to simultaneously measure the data and its background. Furthermore, the statistical uncertainty of the measured background was much better than that of the data itself, making its error small by comparison.

During data aquisition events were sorted into different energy spectra depending on their relative timing with respect to $^{2}H(n,\gamma)^{3}H$ events. Three time windows, which would sort events into three separate energy spectra, are displayed in Figure 3-3. Gates 1 and 3, which do not envelop the $^{2}H(n,\gamma)^{3}H$ TAC peak or any other structure, were used to sort background events. They were deliberately made wide in order to reduce the statistical uncertainty in the background sums. One may ask if it is valid to assume that the background resulting from events occurring off the TAC peak is identical to the background from events in the time window containing the TAC peak. Since a dc beam was employed in the experiment, the only way they could be different would be if other reactions generated time-correlated signals between the NaI

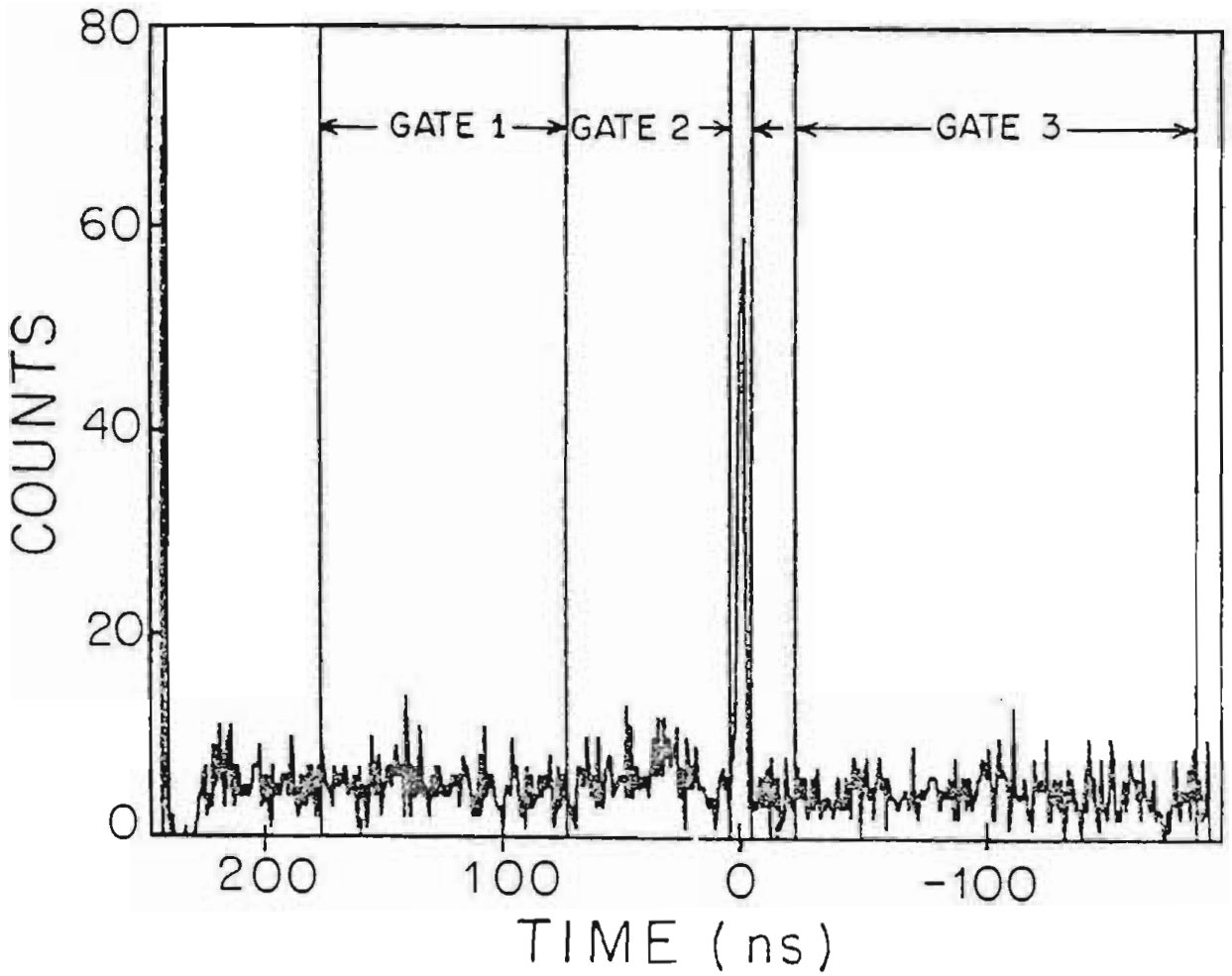

Figure 3-3. Time windows employed to sort data.

detector and scintillator (i.e. created a TAC peak). Recall which reactions can cause TAC peaks (§2.5). Neutrons which scatter into the NaI detector from deuterons in the target produce a TAC structure at around TIME = +35 ns, hence this region of the spectrum was avoided in selecting background TAC gates. Neutron capture by ^{12}C, producing γ-rays and recoiling ^{13}C nuclei, would create a TAC peak inside gate 2 if not for the fact that the signals from the recoils were not large enough to pass through the scintillator discriminator. Neutrons which inelastically scatter from ^{12}C (causing a γ-ray) and then rescatter from deuterons in the target create a TAC peak in the vicinity of gate 2. However, all the γ-rays from this process are less in energy than the $^{2}H(n,\gamma)^{3}H$ γ-ray because of the 6.3 MeV Q-value of the latter reaction. So although the inelastic scattering events may contribute to the TAC peak within gate 2, they do not create background under the $^{2}H(n,\gamma)^{3}H$ peak in the energy spectrum. In view of the above facts, what was the origin of the background in the region of the $^{2}H(n,\gamma)^{3}H$ data? A background count arises from the random pile-up of a low energy γ-ray signal with a higher energy γ-ray signal which is capable of passing through the NaI discriminator. Pile-up signals which were accidentally in coincidence with events in the scintillator were accepted by the computer and appeared in spectra. The large count-rate out of the scintillator discriminator, ~0.5 MHz, contributed to the occurrence of accidental coincidences. Since the pile-up background had no definite time correlation with the scintillating target, it was accurately measured with proper selection of TAC gates (as in Figure 3-3).

A typical background spectrum is displayed at the top of Figure 3-4. It has been normalized according to

$$3\text{-}3 \qquad \text{(normalized bkgd)} = \text{(raw bkgd)} \times \frac{\text{(width of TAC gate 2)}}{\text{(width of bkgd TAC gate)}}.$$

A superposition of the background spectrum over the corresponding $^{2}H(n,\gamma)^{3}H$ spectrum is shown underneath. It is evident from the superposition that the background in the $^{2}H(n,\gamma)^{3}H$ spectrum has been accurately measured by employing offset TAC gates.

The gate in Figure 3-4 represents the appropriate summing region for the data. An average background sum, to be subtracted from the raw $^{2}H(n,\gamma)^{3}H$ sum, was calculated as follows. First the sums from the two background spectra were normalized according to Equation 3-3. Then a linear interpolation was done, employing the centroids of TAC gates 1, 2 and 3, to project an average background for data generated by TAC gate 2. It was necessary to do this because the background from TAC gate 1 was always greater than that from TAC gate 3. This was because more accidental coincidences were registered to the left of the $^{2}H(n,\gamma)^{3}H$ TAC peak than to the right of it. In order to understand this, consider the following limiting case: As the count-rate from the scintillator discriminator (into the stop of the TAC) gets large, the channel number in which the event appears gets small. The difference between the two background sums ranged from 5 to 30% depending on experimental conditions (i.e. the count-rate out of the scintillator and the positions of TAC gates 1 and 3). Average background sums are presented in the tables of §3.5.

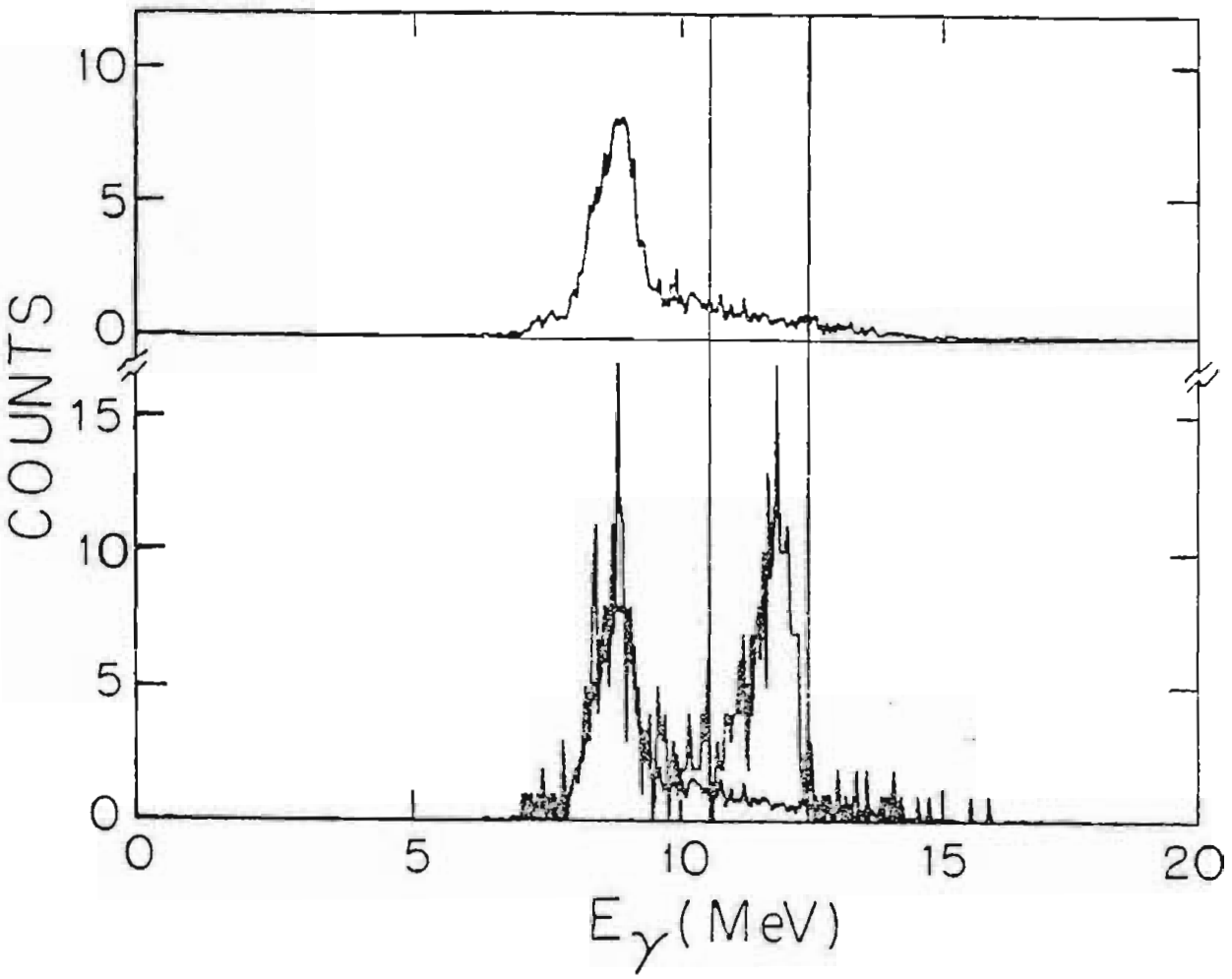

Figure 3-4. NaI energy spectra. A normalized background spectrum is displayed on top. Its superposition over the corresponding $^{2}H(n,\gamma)^{3}H$ data is displayed below.

3.3 Scaler Corrections

There are several correction factors which must be applied to the data to account for systematic loss of signals due to intrinsic characteristics of the electronics apparatus. These losses arise from system dead time associated with the processing time of an event and from accidental overlap of pulses in anti-coincidence or coincidence circuits.

During the time required to process an event the detection system electronics is blind to any incoming data. In practice, essentially all the dead time in the electronics circuit is attributable to the ADC. During the $^{2}H(n,\gamma)^{3}H$ experiment a LeCroy 2259A twelve-channel ADC, with dead time of approximately 130 μs per event, was employed in each NaI detector circuit. Since the linear γ-ray signal was gated by the output of a discriminator prior to entering the ADC, a measure of the number of events lost is simply the difference between the number of discriminator-generated gates and the number of events digitized by the ADC (i.e. stored in a spectrum). The observed data was corrected by the ratio of gates to digitized events to account for dead time. Due to the relatively small γ-ray counting rate of this capture experiment, the correction was typically 1%. Although not practical while taking data, one can measure the entire system dead time by employing an LED and pulsing light at a known rate into the NaI detector. This has been done as a test and is in excellent agreement with the gates/events ratio

(Weller, 1984).

The NaI detectors employed in this experiment were surrounded by scintillating plastic shields consisting of NE110 material. Events which were in coincidence between the detector and shield were rejected. This is an effective method of reducing background resulting from neutrons and cosmic-rays. Since the light collection efficiency of NE110 for 10 to 15 MeV γ-rays is essentially zero, the $^{2}H(n,\gamma)^{3}H$ data were not directly affected. However, there exists a nonzero probability that a random coincidence event will register at the same time that a γ-ray is detected, thus accidentally rejecting good data. The data must be corrected for this effect. In Equation 3-4 the number of total coincidences (TOT COIN) and the number of accidental coincidences (ACC COIN) are measured quantities:

$$\text{(TOT COIN)} = \text{(TRUE COIN)} + \text{(ACC COIN)}. \tag{3-4}$$

Observed and true data are related by the probability that an accidental coincidence (P(ACC COIN)) has occurred:

$$\text{(OBS DATA)} = \text{(TRUE DATA)} \left[1 - \text{P(ACC COIN)}\right], \tag{3-5}$$

where

$$\text{P(ACC COIN)} = \frac{\text{(ACC COIN)}}{\text{(TOT COIN)}}. \tag{3-6}$$

It follows that the observed data should be corrected according to

$$\text{(TRUE DATA)} = \text{(OBS DATA)} \frac{\text{(TOT COIN)}}{\text{(TOT COIN)} - \text{(ACC COIN)}} \tag{3-7}$$

to obtain the true data. The magnitude of the correction factor depends on the number of accidental coincidences relative to total coincidences. According to Evans (1955) the accidental coincidence rate R_{ac} may be expressed as

$$R_{ac} = (R_1 - R_{tc})\,(R_2 - R_{tc})\,(\tau_1 + \tau_2), \tag{3-8}$$

where R_1 is the count-rate of the NaI detector, R_2 is the count-rate of the shield, R_{tc} is the true coincidence count-rate between them and $\tau_1 + \tau_2$ is the coincidence resolving time. Thus, for a given resolving time, the accidental coincidence correction may be kept small by limiting the count-rates in the detector (R_1) and shield (R_2). In the $^2H(n,\gamma)^3H$ experiment, typical count-rates and resolving time were R_1 = 14.0 Hz, R_2 = 300 kHz, R_{tc} = 12.5 Hz, R_{ac} = 0.300 Hz and $\tau_1 + \tau_2$ = 60 ns. The correction to the data ranged from 1.01 to 1.04.

Consider now the coincidence circuit between the NaI detector and the NE232 scintillating target (recall Figure 2-6). A TAC spectrum is obtained by routing detector signals to the start of the TAC and routing target signals to the stop of the TAC. Consequently, a window is set about the $^2H(n,\gamma)^3H$ TAC peak and used in sorting the energy spectrum. The problem of accidental coincidences <u>adding</u> false counts (background) to the data is handled by sorting background spectra with offset TAC gates (see §3.2). However, there exists an additional effect which can cause the <u>loss</u> of data. Recall from previously shown TAC spectra that there is some finite time between the start signal and the stop signal of a true $^2H(n,\gamma)^3H$ coincidence (e.g. Figure 2-9). During the history

of the experiment this finite time ranged between 160 to 250 ns, varying only because different delay cables were used in setting up the experiment on different dates. Considering the huge count-rate from the scintillator discriminator, what is the probability that a random stop pulse will come before the true one, thus eliminating a good γ-ray? Equation 3-8, in the case of only accidental coincidences, is

$$R_{ac} = R_1 R_2 (\tau_1 + \tau_2), \tag{3-9}$$

where R_1 is the $^2H(n,\gamma)^3H$ count-rate, R_2 is the count-rate of the scintillator discriminator and $\tau_1 + \tau_2$ (= 160 to 250 ns) is the resolving time. The percent of good data lost is the ratio of the accidental coincidence count-rate to the $^2H(n,\gamma)^3H$ count-rate:

$$\frac{R_{ac}}{R_1} = R_2 (\tau_1 + \tau_2). \tag{3-10}$$

In the experiment this ratio ranged from 10% to 14%. The data were corrected for this effect according to:

$$(\text{TRUE DATA}) = (\text{OBS DATA}) \frac{1}{1 - R_2 (\tau_1 + \tau_2)} \tag{3-11}$$

It has been possible to experimentally test the validity of Equation 3-11 by employing the circuit of Figure 3-5. As shown, delayed start signals were fanned-in with stop signals. By forcing each start to be in coincidence with itself, one can observe exactly how many of these coincidences emerge in the TAC peak. Figure 3-6 displays the TAC spectrum obtained with this self-gated circuit. Over a data aquisition period of 277.1 s, 3166 start signals and 213.9 X 10^6 stop signals occurred. The resolving time was intentionally made large and equaled

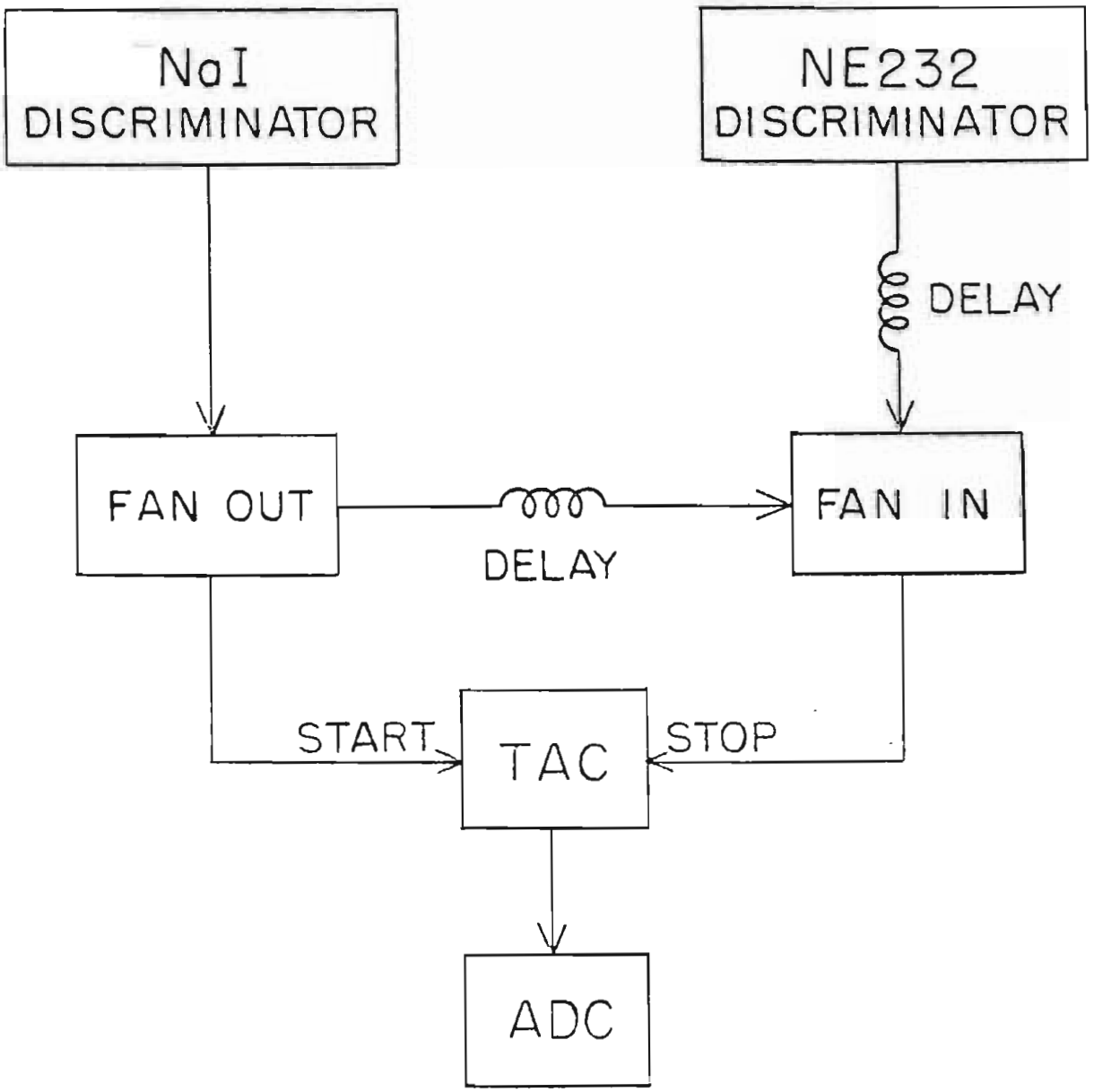

Figure 3-5. Block diagram of self-gated coincidence circuit.

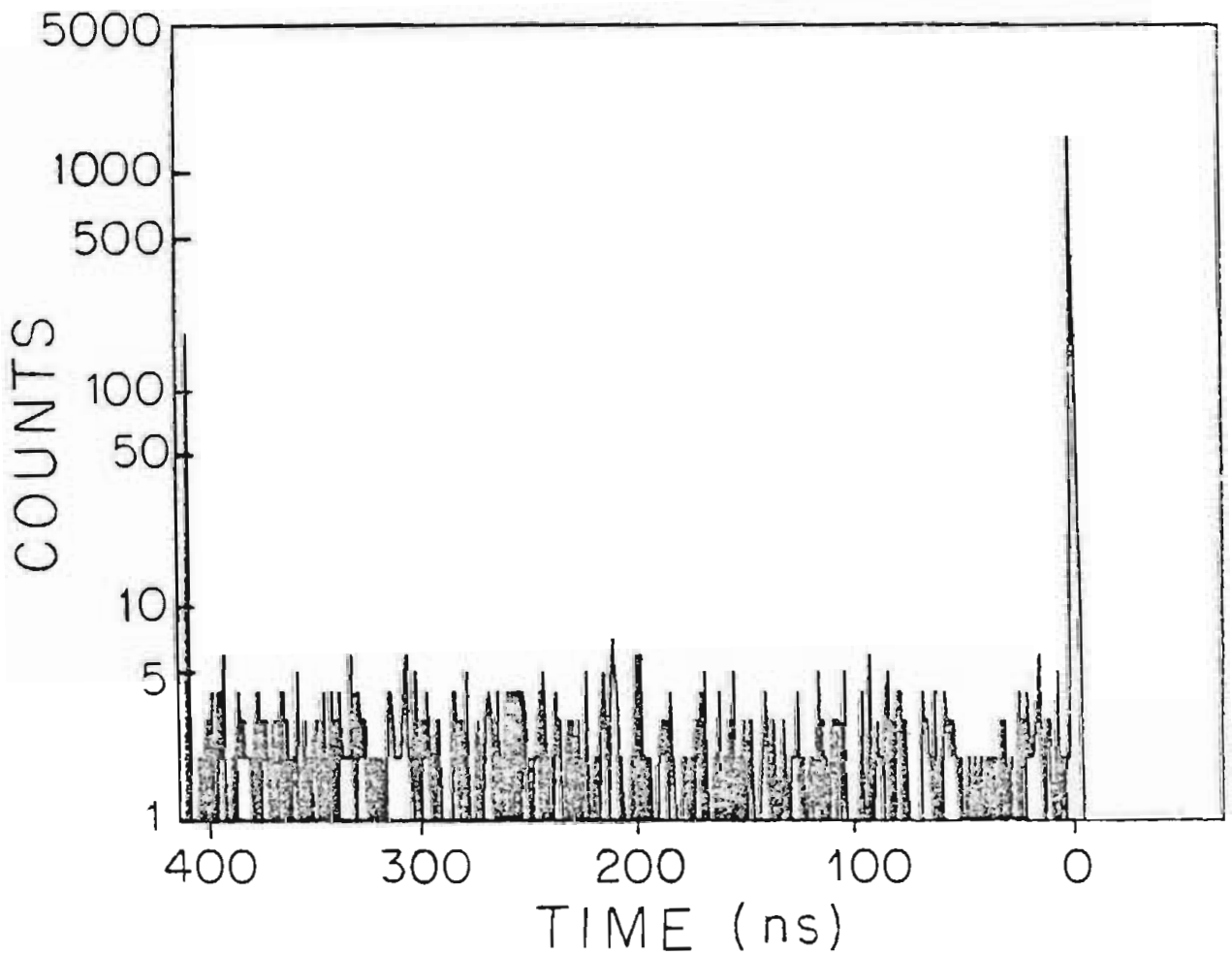

Figure 3-6. TAC spectrum resulting from the self-gated circuit of Figure 3-5. The number of counts in the peak at TIME = 0 is 2151, out of a total of 3166 in the entire spectrum.

406 ns. From these numbers the theoretically determined correction factor is

3-12 $$\frac{1}{1 - R_2 (\tau_1 + \tau_2)} = 1.46.$$

Experimentally it was found that the ratio of start pulses to the number of counts in the peak was 3166/2151 = 1.47. The agreement is excellent and supports correcting the data according to Equation 3-11.

Scaler corrections to the data for dead times and accidental coincidences are listed in the tables of §3.5.

3.4 Finite-Geometry Corrections

Thus far this chapter has been concerned with how raw data were reduced to corrected net sums. However, these sums are not physically meaningful observables. The aim of the thesis experiment was to measure angular distributions of cross sections and analyzing powers of the $^2H(n,\gamma)^3H$ reaction. Due to the finite sizes of the neutron-producing gas cell, target sample and detector, the measured count-rate of the detector must be correctly interpreted in order to extract the result for point geometry. The following effects must be accounted for: (1) Neutron flux averaging over the volume of the target and γ-ray flux averaging over the area of the detector; (2) neutron and γ-ray flux attenuation in the target; and (3) neutron multiple-scattering.

A Monte Carlo program, FIXER (Jensen, 1981), was used to calculate a correction factor relating the observed differential cross section to

the true differential cross section:

3-13 $$\sigma_{true} = R\,\sigma_{obs}.$$

Displayed in Figure 3-7 is the geometry modeled by FIXER and the logic of the program is as follows. The procedure begins with the random selection of three points: One within the gas cell (neutron source point); one within the target ($^{2}H(n,\gamma)^{3}H$ reaction point); and one on the detector face (γ-ray detection point). This defines the path traveled by the neutron and the path traveled by the γ-ray. Employing measured differential and total cross sections, and an assumed $^{2}H(n,\gamma)^{3}H$ differential cross section (σ_{guess}), FIXER proceeds to calculate a probability associated with the chosen paths: The differential $^{2}H(d,n)^{3}He$ cross section (Drösg, 1978) is used at the source point; the total neutron absorption cross section (ENDF/B-5; Seagrave, 1970; Hopkins, 1971) is used for neutron attenuation in the target; σ_{guess} is used at the $^{2}H(n,\gamma)^{3}H$ reaction point; and the total γ-ray absorption cross section (Storm, 1970) is used for γ-ray attenuation in the target. Some of the attenuated neutron flux remains in the target because of multiple-scattering and must also be included in the calculation of the correction factor. In this case another point within the target ((n,n) reaction point) is randomly selected. Here the neutron elastic scattering differential cross section is used (ENDF/B-5; Schwarz, 1983; Hopkins, 1971). Note that all the scattering and attenuation effects are treated sequentially, or in another word, <u>independently</u> by FIXER. They can be turned on or off by appropriate selection of control input.

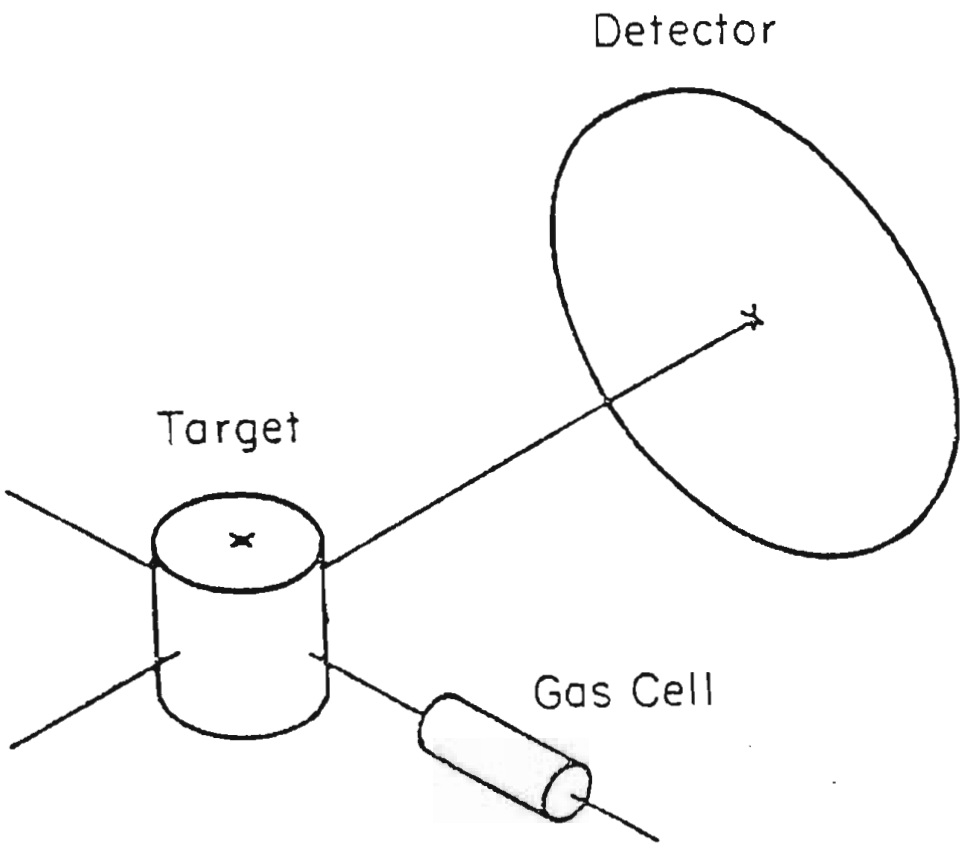

Figure 3-7. Geometry modeled by FIXER.

The algorithm just described (i.e. select a set of random points and calculate a probability associated with the defined paths) is carried out repeatedly. This repetition effectively averages the calculated probability over target volume and detector area. Convergence to what shall be called the predicted $^{2}H(n,\gamma)^{3}H$ differential cross section (σ_{pred}) occurs within 5000 histories. This prediction is compared with the observed cross section and a new guess is obtained according to

$$\sigma_{guess}^{(i+1)} = \frac{\sigma_{obs}}{\sigma_{pred}^{(i)}} \sigma_{guess}^{(i)}. \qquad 3\text{-}14$$

The initial guess ($\sigma_{guess}^{(1)}$) was taken to be the observed $^{2}H(n,\gamma)^{3}H$ γ-ray cross section (σ_{obs}). In practice, only one iteration was necessary to obtain R since $\sigma_{obs} - \sigma_{pred}^{(2)}$ was small. Hence the correction factor is given by

$$R = \frac{\sigma_{obs}}{\sigma_{pred}^{(1)}}. \qquad 3\text{-}15$$

All of the targets employed in this experiment (NE232, D_2O, H_2O) were mixtures of two nuclei. This complication necessitated the following changes in running FIXER.

Consider attenuation. Given some incident flux of uncharged particles I_o, the transmitted flux as a function of distance through the medium is

$$I = I_o e^{-\mu x}, \qquad 3\text{-}16$$

where the total attenuation coefficient $\mu(cm^2/g)$ is proportional to the total absorption cross section $\sigma(cm^2)$. Evans (1955) states that since the attenuation of neutral particles in mixtures is assumed to depend only on the sum of the cross sections resulting from all of the nuclei in the mixture, the overall attenuation coefficient is the weighted average of the individual ones,

3-17 $$\mu = \frac{\Sigma N_i \mu_i}{\Sigma N_i},$$

where N_i are the individual number densities of the nuclei. Neutron and γ-ray attenuation were treated this way in calculating R.

Neutron multiple-scattering is the remaining effect which must be treated properly for a mixed target. Since this effect depends on the kinematics of the (n,n) reaction, simple averaging of the differential cross sections is incorrect. It was necessary to run the program separately for the two types of individual nuclei and then combine the results. As stated before, neutron multiple-scattering is independent of the other processes in the program. Recall that $R = \sigma_{true}/\sigma_{obs}$. Rewrite σ_{obs} as the sum of just the multiple-scattering cross sections $(\sigma_{ms1} + \sigma_{ms2})$ plus the rest of the cross section (σ_o):

3-18 $$\sigma_{obs} = \sigma_o + \sigma_{ms1} + \sigma_{ms2}.$$

Let $\sigma_1 = \sigma_o + \sigma_{ms1}$ and $\sigma_2 = \sigma_o + \sigma_{ms2}$. Then

3-19 $$\sigma_{obs} = \sigma_1 + \sigma_2 - \sigma_o,$$

3-20 $$R = \frac{\sigma_{true}}{\sigma_1 + \sigma_2 - \sigma_o},$$

and

3-21 $$\frac{1}{R} = \frac{\sigma_1}{\sigma_{true}} + \frac{\sigma_2}{\sigma_{true}} - \frac{\sigma_o}{\sigma_{true}} = \frac{1}{R_1} + \frac{1}{R_2} - \frac{1}{R_o}.$$

Hence the correction factor R was obtained by running FIXER three times: Once including multiple-scattering for one target nucleus, once including multiple-scattering for the other target nucleus and once without multiple-scattering. In each case the average γ-ray and neutron attenuations were applied. One technical note: The number density for the entire target, $N = N_1 + N_2$, is necessary in the calculation of the γ-ray and neutron attenuations, hence σ_{ms1} and σ_{ms2} must by normalized by N_1/N and N_2/N respectively.

What remains to be considered is the contribution of the cylindrical glass shell, which contained the target material, to the solid-geometry correction. The thickness of each container which held a water target was slightly less than a millimeter. This was calculated from the measured mass and outer dimensions of each individual container, assuming uniform glass thickness throughout. The thickness of the cylindrical glass wall of the NE232 scintillator was also less than a millimeter. This was observed through its unpainted glass bottom (i.e. the end to which the light pipe was later attached). In order to calculate γ-ray and neutron attenuations it was assumed that the chemical composition of the glass was purely SiO_2, with density equal to that of pyrex, 2.3 g/cm^3. Employing the 10 MeV γ-ray attenuation

coefficients for silicon and oxygen (Storm, 1970), the average attenuation coefficient was calculated to be 0.022 cm^2/g. Consequently, $\mu x = 0.022\ cm^2/g \cdot 2.3\ g/cm^3 \cdot 0.1\ cm = 0.0051$, and the γ-ray attenuation $\left[1 - \exp(-\mu x)\right] = 0.5\%$. At higher γ-ray energies the attenuation is less. In the case of neutron attenuation a similar calculation was done employing the total neutron cross sections of Schwartz et al. (1974) and yielding an attenuation of 0.3%. Both of these effects are small and were ignored in the data reduction procedure.

The contributions to the overall R from the component effects were 18% to 35% geometry (energy dependent), 18% neutron attenuation, 2.4% γ-ray attenuation and -3.5% neutron multiple-scattering (the minus sign means that the magnitude of the correction factor decreased).

3.5 Corrected Data

The net sums, arrived at by applying the corrections discussed in this chapter, are presented in the tables at the end of this section. The uncertainties quoted are purely statistical. Systematic uncertainties are accounted for in the calculation of the $^2H(n,\gamma)^3H$ cross sections which are presented in §4.4.

Tables 3-1 through 3-3 are the data measured with the scintillating target. Five point polarized and unpolarized angular distributions were measured at neutron bombarding energies of 9.00 and 10.80 MeV respectively. A $\theta_\gamma(c.m) = 90^\circ$ yield measurement was made at

E_n(lab) = 6.85 MeV.

Water target results for E_n(lab) = 14.00 MeV are presented in Table 3-4. Data were taken at two angles, θ_γ(lab) = 65° and 125°. Two differences exist between the correction factors in the water case versus those which have been discussed for the scintillating target. One stems from a different approach to obtaining a TAC spectrum and the other from the use of a separate target for background measurements.

The water data of this experiment were measured with a pulsed beam. This enabled the use of a time-of-flight criterion to reduce background. A TAC spectrum was generated by start signals from the NaI detector and stop signals from a capacitive "pick-off" near the end of the beam line (Weller, 1981; Wender, 1980). Because γ-rays and neutrons have different flight times from the target to the detector, the neutron TAC peak is well resolved from the "gamma-flash". By employing a narrow sorting window about the "gamma-flash", fast neutron generated background is eliminated. The stop signal to the TAC comes from a single pick-off pulse per beam burst, hence the problem of accidental stops (see §3.3) does not exist. Instead, pick-off pulses may occasionally be missed because they do not exceed the discriminator threshold set at the noise level. The data are corrected for this effect according to

$$f_4 = \frac{T\gamma}{N_{po}}, \qquad 3\text{-}22$$

where T is the beam integration time, γ is the frequency of the beam pulsing and N_{po} is the number of pick-off pulses from the discriminator

counted during time T.

Background measurements were performed by replacing the deuterated water with distilled water. It is evident from the appearance of the spectra that the background at 125° was from the tails of $^{16}O(n,\gamma_0)^{17}O$ and $^{16}O(n,\gamma_1)^{17}O^*$ γ-rays, while the background at 65° was primarily due to pile-up. Since the number of oxygen nuclei was 5% less in the distilled water target than in the deuterated target, the background at 125° was corrected accordingly ($f_5 = 1.05$).

Table 3-1. Data measured at E_n(lab) = 10.80 MeV. The counts detected at various lab angles by the right (R) and left (L) detectors are listed. Uncertainties shown are purely statistical. Correction factors f_1, f_2, f_3 and R are for accidental coincidences with the shield, dead time in the electronics, accidental stop signals in the TAC and finite geometry.

θ_γ	DET	Q(mC)	SUM	BACKGROUND	f_1	f_2	f_3	R	CORRECTED COUNTS PER mC
52.7°	R	1.51	219 ± 14.8	70.6 ± 1.72	1.039	1.009	1.129	1.52	177 ± 17.8
52.7°	R	1.06	143 ± 12.0	53.1 ± 1.49	1.038	1.009	1.142	1.52	154 ± 20.7
52.7°	L	2.88	342 ± 18.5	108.9 ± 2.14	1.039	1.009	1.117	1.52	144 ± 11.5
70.0°	R	2.01	278 ± 16.7	60.2 ± 1.59	1.028	1.009	1.142	1.53	196 ± 15.2
70.0°	L	1.96	278 ± 16.7	52.0 ± 1.48	1.030	1.009	1.129	1.53	206 ± 15.3
87.1°	R	1.67	243 ± 15.6	28.8 ± 1.09	1.023	1.010	1.130	1.53	229 ± 16.7
87.1°	L	1.67	253 ± 15.9	35.3 ± 1.21	1.025	1.009	1.117	1.53	230 ± 16.8
110.0°	R	1.96	259 ± 16.1	27.8 ± 1.08	1.020	1.010	1.142	1.53	212 ± 14.8
110.0°	L	2.01	265 ± 16.3	26.9 ± 1.06	1.024	1.009	1.127	1.53	211 ± 14.5
135.0°	R	2.88	243 ± 15.6	35.2 ± 1.21	1.020	1.010	1.130	1.50	126 ± 9.5
135.0°	L	1.51	149 ± 12.2	19.7 ± 0.91	1.024	1.009	1.116	1.50	148 ± 14.0
135.0°	L	1.06	95 ± 9.7	12.7 ± 0.72	1.023	1.010	1.129	1.50	136 ± 16.2

Table 3-2. Polarized data measured at E_n(lab) = 9.00 MeV. The counts detected at various lab angles by the right (R) and left (L) detectors are listed. Uncertainties shown are purely statistical. Polarized neutron spins "+" and "−" correspond to up and down in the laboratory. In terms of the right hand convention $\vec{n} = \vec{k}_{in} \times \vec{k}_{out}$, "+" and "−" mean $+\vec{n}$ and $-\vec{n}$ respectively for the left detector, but they mean $-\vec{n}$ and $+\vec{n}$ respectively for the right detector. Correction factors f_1, f_2, f_3 and R are for accidental coincidences with the shield, dead time in the electronics, accidental stop signals in the TAC and finite geometry.

θ_γ	DET	SPIN	Q(mC)	SUM	BACKGROUND	f_1	f_2	f_3	R	CORRECTED COUNTS PER mC
52.9°	R	+	1.35	213 ± 14.6	79.0 ± 1.77	1.016	1.010	1.114	1.42	161 ± 17.7
52.9°	R	−	1.35	211 ± 14.5	80.2 ± 1.79	1.017	1.010	1.115	1.42	158 ± 17.6
52.9°	L	+	1.35	270 ± 16.4	119.5 ± 2.18	1.013	1.037	1.103	1.42	183 ± 20.2
52.9°	L	−	1.35	258 ± 16.1	115.2 ± 2.14	1.013	1.036	1.104	1.42	174 ± 19.8
70.0°	R	+	1.40	264 ± 16.2	52.7 ± 1.44	1.007	1.010	1.111	1.45	247 ± 19.1
70.0°	R	−	1.40	255 ± 16.0	57.9 ± 1.52	1.008	1.010	1.111	1.45	231 ± 18.8
70.0°	L	+	1.40	291 ± 17.1	65.2 ± 1.61	1.011	1.028	1.104	1.45	268 ± 20.4
70.0°	L	−	1.40	254 ± 15.9	62.4 ± 1.57	1.011	1.027	1.104	1.45	227 ± 19.0

Table 3-2. Continued.

θ_γ	DET	SPIN	Q(mC)	SUM	BACKGROUND	f_1	f_2	f_3	R	CORRECTED COUNTS PER mC
100.0°	R	+	1.20	202 ± 14.2	26.1 ± 1.02	1.007	1.009	1.121	1.43	239 ± 19.4
100.0°	R	−	1.20	217 ± 14.7	28.5 ± 1.07	1.008	1.010	1.114	1.43	255 ± 20.0
100.0°	L	+	1.20	216 ± 14.7	36.8 ± 1.21	1.010	1.031	1.114	1.43	248 ± 20.4
100.0°	L	−	1.20	205 ± 14.3	33.8 ± 1.16	1.010	1.028	1.114	1.43	236 ± 19.8
122.8°	R	+	1.50	234 ± 15.3	25.2 ± 1.00	1.006	1.009	1.106	1.40	219 ± 16.0
122.8°	R	−	1.50	203 ± 14.2	28.8 ± 1.06	1.007	1.010	1.111	1.40	184 ± 15.0
122.8°	L	+	1.50	229 ± 15.1	30.9 ± 1.11	1.010	1.066	1.100	1.40	219 ± 16.8
122.8°	L	−	1.50	210 ± 14.5	32.2 ± 1.13	1.010	1.064	1.105	1.40	197 ± 16.1
135.0°	R	+	1.35	147 ± 12.1	20.9 ± 0.91	1.007	1.009	1.100	1.36	142 ± 13.7
135.0°	R	−	1.35	168 ± 13.0	25.0 ± 1.00	1.008	1.009	1.111	1.36	163 ± 14.8
135.0°	L	+	1.35	148 ± 12.2	34.2 ± 1.16	1.011	1.078	1.106	1.36	138 ± 14.8
135.0°	L	−	1.35	143 ± 12.0	36.9 ± 1.21	1.010	1.078	1.107	1.36	129 ± 14.6

Table 3-3. Data measured at E_n(lab) = 6.85 MeV. The counts detected at a lab angle of 87.7^o by the right (R) and left (L) detectors are listed. Uncertainties shown are purely statistical. Correction factors f_1, f_2, f_3 and R are for accidental coincidences with the shield, dead time in the electronics, accidental stop signals in the TAC and finite geometry.

θ_γ	DET	Q(mC)	SUM	BACKGROUND	f_1	f_2	f_3	R	CORRECTED COUNTS PER mC
87.7^o	R	7.05	820 ± 28.6	58.8 ± 1.20	1.033	1.008	1.095	1.36	167 ± 6.3
87.7^o	R	3.40	435 ± 20.9	87.0 ± 2.04	1.028	1.008	1.130	1.36	163 ± 9.8
87.7^o	R	1.60	222 ± 14.9	66.1 ± 1.66	1.024	1.011	1.121	1.36	154 ± 14.8
87.7^o	L	7.05	978 ± 31.3	220.8 ± 4.32	1.025	1.008	1.107	1.36	167 ± 7.0
87.7^o	L	1.60	525 ± 22.9	158.9 ± 2.85	1.028	1.009	1.125	1.36	171 ± 10.8
87.7^o	L	1.60	300 ± 17.3	95.9 ± 1.99	1.030	1.010	1.110	1.36	200 ± 17.1

Table 3-4. Data measured at E_n(lab) = 14.00 MeV. The counts detected at lab angles 65^o and 125^o by the right (R) and left (L) detectors are listed. Uncertainties shown are purely statistical. Spins "+" and "−" are defined in Table 3-2. Background was measured by replacing the D_2O target with H_2O. The result at right reflects background subtraction. Correction factors f_1, f_2, f_4, f_5 and R are for accidental coincidences with the shield, dead time in the electronics, beam pick-off losses, target number density and finite geometry.

θ_γ	DET	SPIN	TARGET	Q(mC)	SUM	f_1	f_2	f_4	f_5	R	CORRECTED COUNTS PER mC
65.0^o	R	+	D_2O	2.80	1030 ± 32.1	1.053	1.006	1.005	----	1.58	72 ± 34
65.0^o	R	+	H_2O	1.20	380 ± 19.5	1.050	1.006	1.004	1.00	1.63	
65.0^o	R	−	D_2O	2.40	892 ± 29.9	1.053	1.006	1.002	----	1.58	43 ± 36
65.0^o	R	−	H_2O	1.20	402 ± 20.0	1.054	1.006	1.001	1.00	1.63	
65.0^o	L	+	D_2O	2.40	861 ± 29.3	1.050	1.011	1.005	----	1.58	20 ± 36
65.0^o	L	+	H_2O	1.20	405 ± 20.1	1.048	1.011	1.004	1.00	1.63	
65.0^o	L	−	D_2O	2.40	1012 ± 31.8	1.048	1.011	1.002	----	1.58	111 ± 37
65.0^o	L	−	H_2O	1.20	412 ± 20.3	1.053	1.011	1.001	1.00	1.63	

Table 3-4. Continued.

θ_γ	DET	SPIN	TARGET	Q(mC)	SUM	f_1	f_2	f_4	f_5	R	CORRECTED COUNTS PER mC
125.0^o	R	+	D_2O	2.40	240 ± 15.5	1.045	1.006	1.002	----	1.56	49 ± 17
125.0^o	R	+	H_2O	1.00	65 ± 8.1	1.044	1.005	1.001	1.05	1.61	
125.0^o	R	−	D_2O	2.40	298 ± 17.3	1.048	1.006	1.001	----	1.56	103 ± 18
125.0^o	R	−	H_2O	1.00	57 ± 7.5	1.043	1.006	1.001	1.05	1.61	
125.0^o	L	+	D_2O	2.40	279 ± 16.7	1.048	1.017	1.002	----	1.56	70 ± 18
125.0^o	L	+	H_2O	1.00	69 ± 8.3	1.042	1.016	1.001	1.05	1.61	
125.0^o	L	−	D_2O	2.40	286 ± 16.9	1.050	1.017	1.001	----	1.56	66 ± 19
125.0^o	L	−	H_2O	1.00	74 ± 8.6	1.043	1.016	1.001	1.05	1.61	

4 DATA ANALYSIS AND EXPERIMENTAL RESULTS

4.1 Overview

The results presented in this chapter represent the first measurements of $^{2}H(n,\gamma)^{3}H$ angular distributions of cross sections and analyzing powers at non-thermal neutron energies. New insight into properties of the three-nucleon system and the nuclear force stand to be gained from these original data. Comparisons with theory and with results from other photonuclear reactions involving ^{3}H and ^{3}He have proved both interesting and surprising.

Previous measurements of the photodisintegration of ^{3}H have been performed by three groups. Bösch et al. (1964, 1965) reported one angular distribution of cross sections and three total cross sections obtained by detecting neutrons. Kosiek et al. (1966) and Pfeiffer (1968) measured 90^{o} deuteron yields at numerous energies. Faul et al. (1980, 1981) determined the total cross section as a function of energy by detecting neutrons. Measurements of the electrodisintegration of ^{3}H are reported by Skopik et al. (1981), from which fore-aft asymmetries and 90^{o} differential cross sections have been obtained by detecting deuterons.

The ^{3}He system has been extensively investigated by many groups through capture, photodisintegration and electrodisintegration reactions. See Faul et al. (1981) and King (1983) for a comprehensive set of references.

Observables presented in this chapter were obtained from analyses which can be classified as either model-independent or model-dependent. Angular distribution coefficients (§4.2), fore-aft asymmetries (§4.3) and absolute cross sections (§4.4) were obtained from a model-independent analysis. Electromagnetic transition matrix elements (§4.5) were extracted from fits to the polarized data on the basis of several physical assumptions.

4.2 Angular Distributions of Cross Sections and Analyzing Powers

Angular distributions of cross sections may be expanded in terms of Legendre polynomials according to (Weller, 1980)

$$\text{4-1} \qquad \sigma(\theta) = A_0 \left[1 + \sum_{k=1}^{kmax} a_k P_k(\theta) \right].$$

See Appendix B for a list of Legendre (P_k) and associated Legendre (P_k^1) polynomials through order four. Experimental values for the expansion coefficients A_0 and a_k were obtained by searching for a minimum χ^2 on the basis of a least-squares. A good fit to the data determines useful physical observables such as fore-aft asymmetry, ninety degree cross section and total cross section. Similarly, angular distributions of analyzing powers times normalized cross sections may be expanded in terms of associated Legendre polynomials according to

$$\text{4-2} \qquad A_y(\theta) \frac{\sigma(\theta)}{A_0} = \sum_{k=1}^{kmax} b_k P_k^1(\theta),$$

where the vector analyzing power is

$$4\text{-}3 \qquad A_y(\theta) = \frac{1}{P}\,\frac{N_+(\theta) - N_-(\theta)}{N_+(\theta) + N_-(\theta)}.$$

Here $N_+(\theta)$ and $N_-(\theta)$ are the number of spin up and spin down counts as defined by the Madison convention (Barschall, 1970). The neutron beam polarization (P), resulting from polarization transfer in the $^2H(\vec{d},n)^3He$ reaction, may be written

$$4\text{-}4 \qquad P = P_{y'}(0^\circ) = \frac{1.5\ p_3\ K_y^{y'}(0^\circ)}{1 - 0.25\ p_{33}\ A_{zz}(0^\circ)}.$$

This is according to the Cartesian coordinate representation of Ohlsen (1972). The zero degree vector polarization transfer coefficient $K_y^{y'}(0^\circ)$ and tensor analyzing power $A_{zz}(0^\circ)$ were determined experimentally by Lisowski et al. (1975) to be 0.64 ± 0.03 and -0.461 ± 0.010 for the energy range E_n = 6.85 to 14.00 MeV. The polarization of the deuteron beam used in the $^2H(\vec{n},\gamma)^3H$ experiment was 0.69 ± 0.04, as measured by the quench-ratio method (Ohlsen, 1971). Thus the vector and tensor polarizations were $p_3 = p_{33} = 0.69 \pm 0.04$ and the neutron beam polarization was $P = 0.61 \pm 0.05$.

In the $^2H(n,\gamma)^3H$ experiment five differential cross sections were measured at both E_n = 9.0 MeV and E_n = 10.8 MeV, along with two measurements at E_n = 14.0 MeV. Fitting a set of N data points to the Legendre expansion of Equation 4-1 determines, at best, N - 1 coefficients. If statistical uncertainties in the measurements are large, one may not be able to determine the higher order coefficients to significant accuracy. Fits to specific terms of the Legendre expansion have been applied to the differential cross sections at E_n = 9.0 and

10.8 MeV in order to obtain: (1) A_0 and a_2 only; (2) A_0, a_1 and a_2; and (3) A_0, a_1, a_2 and a_3 (see Table 4-1). At both energies it is evident that including the first order term of the expansion (P_1), in addition to the second order term (P_2), improves the reduced χ^2 considerably. This implies the existence of an asymmetry about ninety degrees in the angular distribution. Including the third order term of the expansion results in a significant a_3 coefficient at 10.8 MeV but worsens the fit at 9.0 MeV. The fitting results presented in Table 4-1 show that, in all cases but one, the fit has either an unacceptable χ^2 or yields the unphysical result of negative cross section at some forward angles. If reliable results are to be obtained from these data, constraints must be applied to the fitting procedure.

Previous photonuclear experiments involving ^3H do not provide more precise angular distribution data than those of this experiment. However, experiments involving the ^3He three-body system are a source of numerous and precise measurements of angular distributions of cross sections. In the absence of charge-symmetry breaking force effects, the ^3He results can be reliably used to provide constraints for fitting the ^3H data. The ^3He experiments include, among others, measurements in the energy region of the $^2H(n,\gamma)^3H$ experiment. These are King's (1983) $^2H(p,\gamma)^3He$ measurements detecting γ-rays and Belt's (1970) $^1H(d,^3He)\gamma$ measurements detecting ^3He nuclei. The agreement among these data, obtained employing different experimental techniques, is excellent. Furthermore, superior counting statistics make the precision of the data excellent. The shape of the angular distributions is primarily

Table 4-1. Coefficients obtained by least-squares fitting of Legendre polynomials to center-of-mass angular distributions of cross sections. The data are listed in the tables of §3-5.

E_n = 9.00 MeV	A_0 and a_2	A_0 through a_2	A_0 through a_3
A_0	379. ± 8.0	361. ± 9.1	362. ± 11.6
a_1		-0.21 ± 0.05	-0.19 ± 0.12
a_2	-0.68 ± 0.08	-0.92 ± 0.11	-0.91 ± 0.14
a_3			0.02 ± 0.16
χ^2	2.36	0.96	3.84
Comments	Unacceptable reduced χ^2.	Cross section negative at some forward angles.	Cross section negative at some forward angles. Unacceptable reduced χ^2.

E_n = 10.80 MeV	A_0 and a_2	A_0 through a_2	A_0 through a_3
A_0	166. ± 4.3	161. ± 4.5	165. ± 6.2
a_1		-0.22 ± 0.06	-0.10 ± 0.12
a_2	-0.64 ± 0.09	-0.85 ± 0.11	-0.76 ± 0.14
a_3			0.18 ± 0.18
χ^2	1.71	0.24	0.01
Comments	Unacceptable reduced χ^2.	Cross section negative at some forward angles.	

characterized by a $\sin^2(\theta)$ radiation pattern. This is due to the E1 transition from the continuum state to the predominantly L = 0 ground state of ^{3}He. On the basis of this information, $\sigma(0^\circ) = 0$ and $\sigma(180^\circ) = 0$ would be appropriate constraints applicable to fitting the $^2H(n,\gamma)^3H$ data. However, fits to King's $^2H(p,\gamma)^3He$ data indicate that there exists a small isotropic component to the angular distribution. This is accountable by the E1 transition from the continuum state to the L = 2 component (a few percent) of the ^{3}He ground state. The implication here is that fits to the $^2H(n,\gamma)^3H$ data should be constrained to yield small, but nonzero, cross sections at 0° and 180°. Since either of the aforementioned pairs of constraints are reasonable, both have been applied in the $^2H(n,\gamma)^3H$ analysis. In both cases fictitious data at 0° and 180°, with errors comparable to the measured $^2H(n,\gamma)^3H$ points, were added to the angular distributions being fitted.

Values for nonzero constraints at 0° and 180° were determined as follows. Unconstrained fits to King's $^2H(p,\gamma)^3He$ differential cross sections indicate (to within statistical precision) that, in the energy domain of this work, 0° and 180° cross sections are equal to each other. Consequently, normalization factors based on King's data at E_p = 8.00, 10.93 and 14.96 MeV were calculated according to

$$N(E_p) = \frac{\sigma_{p,\gamma}(E_p,0^\circ) + \sigma_{p,\gamma}(E_p,180^\circ)}{2\,\sigma^{max}_{p,\gamma}(E_p)}, \qquad 4\text{-}5$$

where $\sigma^{max}_{p,\gamma}(E_p)$ is the maximum of the differential cross section at energy E_p. Linear interpolation to the energies of the $^2H(n,\gamma)^3H$

experiment yielded normalization factors of 3%, 3% and 6% corresponding to E_n = 9.0, 10.8 and 14.0 MeV.

With 0.03 $\times$ $\sigma_{n,\gamma}^{max}(E_n)$ constraints at 0° and 180° applied to the angular distributions at E_n = 9.0 and 10.8 MeV, the data were refit to include higher order terms in the Legendre expansion. At both energies it was found that including the fifth order term increased χ^2 and resulted in an a_5 coefficient which was within error of zero. This implies that statistical uncertainties in the measurements are too large to determine a significant a_5 coefficient. What are considered to be the "best fit" results, through order four, are listed in Table 4-2. With the 0.06 $\times$ $\sigma_{n,\gamma}^{max}(E_n)$ constraints at 0° and 180° applied to the heavy water data at E_n = 14.0 MeV, a fit through P_2 was possible. However, Equation 4-7 (§4.3) implies that the a_3 coefficient is extremely significant in determining the fore-aft asymmetry of the angular distribution. Consequently, a fit through P_3 was desirable. This was achieved by imposing the additional constraint $a_3 = -a_1$, which is true if the $^2H(n,\gamma)^3H$ reaction is dominated by E1 and E2 transitions (see Equations 4-19) and which is consistent with the results at 9.0 and 10.8 MeV. See Table 4-2 for a list of the coefficients arising from the fit. The graphs of constrained fits to all the angular distributions are displayed in Figure 4-1.

Forcing the fits to be zero at 0° and 180° had little effect on the expansion coefficients in comparison to the results for nonzero constraints. A_0, a_1, a_3 and the fore-aft asymmetry were not different than in the case of nonzero constraints. The coefficients a_2 and a_4

Table 4-2. Coefficients obtained by constrained[a] least-squares fitting of Legendre polynomials to angular distributions of cross sections and fitting of associated Legendre polynomials to an angular distribution of analyzing powers. The coefficients correspond to fits in the center-of-mass coordinate system. The data are listed in the tables of §3-5.

E_n (MeV)	9.0	10.8	14.0
A_0	362. ± 7.5	161. ± 3.9	119. ± 18.
a_1	-0.12 ± 0.03	-0.15 ± 0.04	-0.36 ± 0.24
a_2	-0.90 ± 0.05	-0.88 ± 0.05	-0.90 ± 0.08
a_3	0.12 ± 0.03	0.15 ± 0.04	0.36 ± 0.28[b]
a_4	-0.06 ± 0.05	-0.08 ± 0.05	
χ^2	0.96	0.02	0.10
b_1	0.034 ± 0.046		
b_2	-0.003 ± 0.034		
b_3	-0.003 ± 0.038		
χ^2	0.34		

[a] All three fits to cross sections were constrained at 0° and 180°. See text.

[b] The 14.0 MeV fit to cross sections was also constrained such that $a_3 = -a_1$.

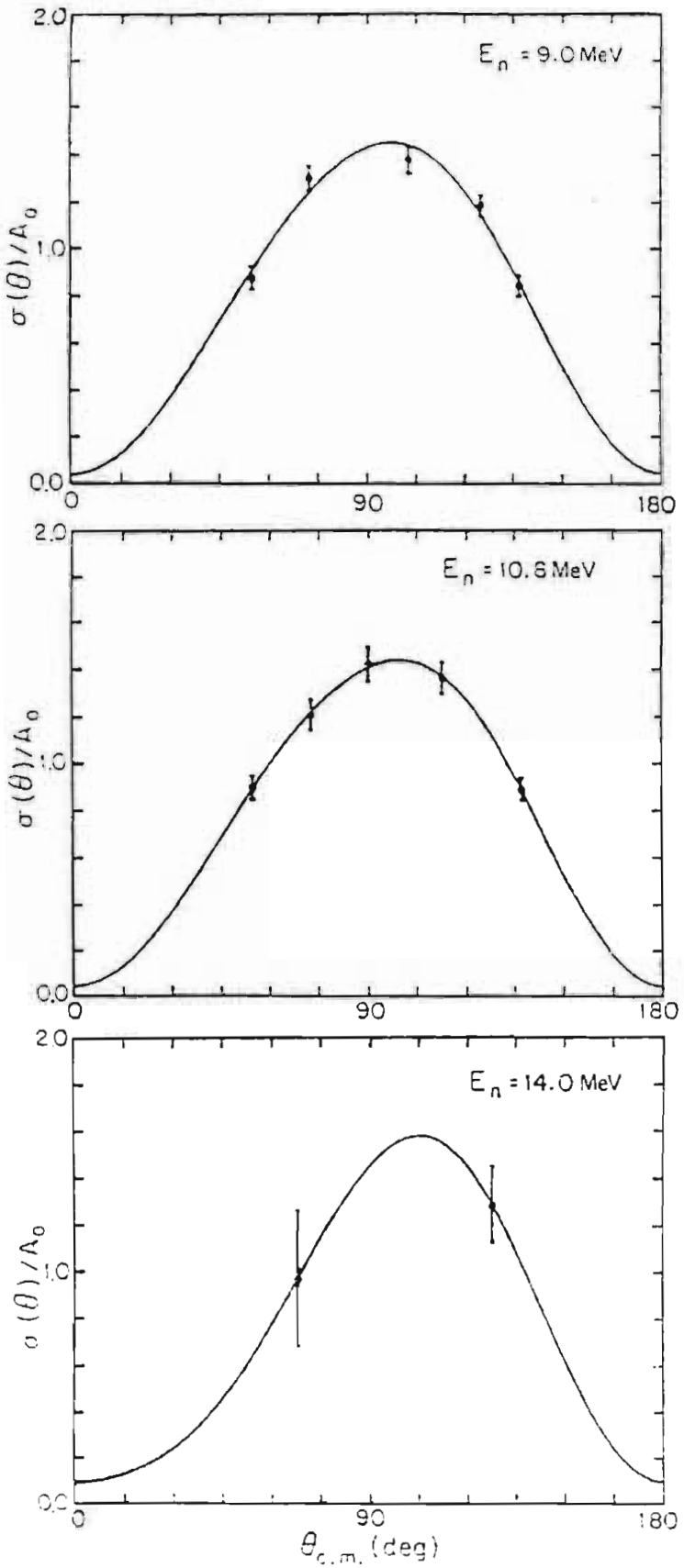

Figure 4-1. Constrained fits to angular distributions of cross sections. The uncertainties are statistical.

changed slightly because $\sigma(0^{\circ}) = \sigma(180^{\circ}) = 0$ requires that $a_2 + a_4 = -1$. The results were $a_2 = -0.92 \pm 0.04$ and $a_4 = -0.08 \pm 0.04$ at $E_n = 9.0$ MeV, and $a_2 = -0.90 \pm 0.05$ and $a_4 = -0.10 \pm 0.05$ at $E_n = 10.8$ MeV.

In the $^2H(\vec{n},\gamma)^3H$ experiment five analyzing powers were measured at $E_n = 9.0$ MeV. Fits to different combinations of associated Legendre polynomials have been performed in order to determine the significance of various b_k coefficients. It was found that fitting through P_4^1 resulted in a b_4 coefficient which was within error of zero and a χ^2 which was greater than that in the fit through P_3^1. Furthermore, including the fourth order term influenced the values of b_1, b_2 and b_3. Consequently, the fit through order three was accepted as the "best fit" and the values of the corresponding b_k coefficients are listed in Table 4-2. Although all the coefficients are within error of zero the virtue of fitting through order three, versus lower order, is that the resulting uncertainties imply a limit to the magnitude of each individual coefficient. The graph of the corresponding fit is displayed in Figure 4-2.

4.3 Fore-aft Asymmetries

Measurements of the fore-aft asymmetry in angular distributions of cross sections have yielded anomalously large values in the $^2H(n,\gamma)^3H$ experiment. When the results were compared to $^2H(p,\gamma)^3He$ measurements, significant deviation from the ratio of -1/5 was found. This ratio is predicted by direct capture calculations in the case where the recoil

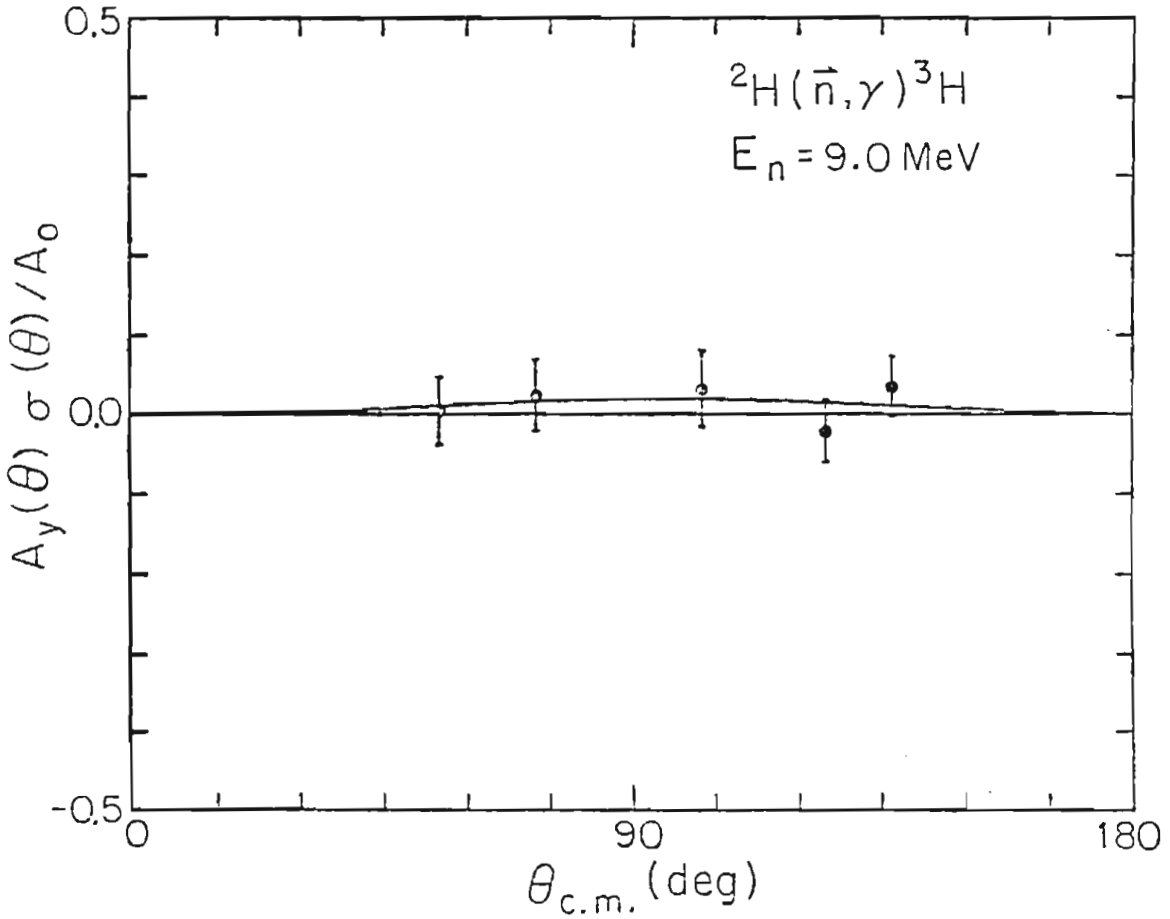

Figure 4-2. Fit to the angular distribution of analyzing powers. The error bars represent statistical uncertainties.

effective charge includes single-particle terms only (Hayward, 1970; Buck, 1977). A detailed discussion of the direct capture formalism and theoretical predictions for the asymmetry ratio is presented in Chapter 5. Besides the $^{2}H(n,\gamma)^{3}H$ results of this work, $^{3}H(e,e'd)n$ measurements at thirteen energies by Skopik et al. (1981) also show a significant enhancement of the asymmetry. However, a $^{3}H(\gamma,n)^{2}H$ measurement near threshold (Bösch, 1965) is quoted by Wölfli et al. (1966) to be in agreement with the ratio of -1/5.

The fore-aft asymmetry is defined according to

$$4\text{-}6 \qquad a_s = \frac{\sigma(\theta_f) - \sigma(\theta_a)}{\sigma(\theta_f) + \sigma(\theta_a)},$$

where the fore and aft angles θ_f and θ_a are the zeros of the Legendre polynomial P_2. These angles are approximately 55° and 125°. In terms of the Legendre polynomial expansion of Equation 4-1 (with kmax = 4), the fore-aft asymmetry is

$$4\text{-}7 \qquad a_s = \frac{a_1 - \frac{2}{3} a_3}{\sqrt{3}\,(1 - \frac{7}{18} a_4)}.$$

The $^{2}H(n,\gamma)^{3}H$ asymmetries resulting from constrained fits to angular distributions of cross sections at E_n = 9.0, 10.8 and 14.0 MeV are tabulated in Table 4-3.

In earlier studies of the three-nucleon system, angular distributions of cross sections have been fit to an expansion in terms of sines and cosines according to

$$4\text{-}8 \qquad \sigma(\theta) = a + b\,(\sin^2\theta + \beta \sin^2\theta \cos\theta + \gamma \sin^2\theta \cos^2\theta + \varepsilon \cos\theta).$$

Table 4-3. $^{2}H(n,\gamma)^{3}H$ asymmetries obtained from constrained fits to the data.

E_n (MeV)	E_γ (MeV)	a_s
9.00	12.2	-0.115 ± 0.028
10.80	13.4	-0.136 ± 0.032
14.00	15.5	-0.344 ± 0.195

The relationships between the expansion coefficients of Equation 4-8 and the Legendre coefficients are presented in Appendix B. In terms of the coefficients of Equation 4-8, the fore-aft asymmetry is

$$4\text{-}9 \qquad a_s = \frac{\beta + \frac{3}{2}\varepsilon}{\sqrt{3}\,(1 + \frac{3}{2}\frac{a}{b} + \frac{1}{3}\gamma)}.$$

The $^3H(\gamma,n)^2H$ angular distribution of Bösch et al. (1965) was obtained by detecting emitted neutrons with BF_3 photomultiplier tubes embedded in paraffin. The technique employed was to compare experimentally observed count rates from the $^3H(\gamma,n)^2H$ and $^2H(\gamma,n)^1H$ reactions, the latter known from previous experiments. The resulting angular distribution for the $^3H(\gamma,n)^2H$ reaction was fit to a truncated version of Equation 4-8, with $\gamma = \varepsilon = 0$. Although not given explicitly, β and a/b can be read from Figure 7 of their paper and used to determine a_s.

The asymmetries of Skopik et al. (1981) were calculated directly from measurements of differential cross sections at 55° and 125°. The cross sections were obtained by detecting emitted deuterons from the electrodisintegration reaction $^3H(e,e'd)n$. At some energies a Ta foil was inserted as a radiator in order to generate a real photon beam and observe the deuteron count rate from the photodisintegration reaction $^3H(\gamma,d)n$. The two measurements are reported to have agreed to within 10%. The results of the asymmetry measurements are presented in their Figure 3 as β, where

$$4\text{-}10 \qquad \beta = \frac{a_s}{\cos(55^\circ)}.$$

This is not to be confused with β of Equation 4-8, although they may be equal under certain conditions ($a/b = \gamma = \varepsilon = 0$).

Because the fore-aft asymmetry is defined according to Equation 4-6, its sign depends on the reaction involved and the particle detected. However, it is possible to transform to a representation in which asymmetries involving the ^{3}He nucleus are positive, whereas those involving the ^{3}H nucleus are negative. This is the adopted representation in this dissertation.

Displayed in Figure 4-3 is a set of existing asymmetry measurements from threshold to 40 MeV excitation energy. An expanded view, up to 20 MeV, is shown in Figure 4-4. The aforementioned data of Skopik et al. (1981), Bösch et al. (1965) and two points from this work are shown. The E_γ = 15.5 MeV ^{2}H(n,γ)^{3}H point has not been plotted due to its large uncertainty. The predominant feature of the ^{3}H data is the disagreement between the capture data of this work and the electrodisintegration measurements between 10 and 15 MeV of Skopik. Interestingly, this work agrees with the trend of Skopik's data above 15 MeV. There is reason to believe that the two electrodisintegration points at low energies should not be compared to data from real photons. The analysis of these points is currently being reviewed (Skopik, 1984). It is possible that at low energies the virtual photon spectrum, corresponding to the detected deuterons, contained enhanced E2 strength relative to real photons. Consequently, the electrodisintegration measurements may display enhanced asymmetry when compared to ^{2}H(n,γ)^{3}H data.

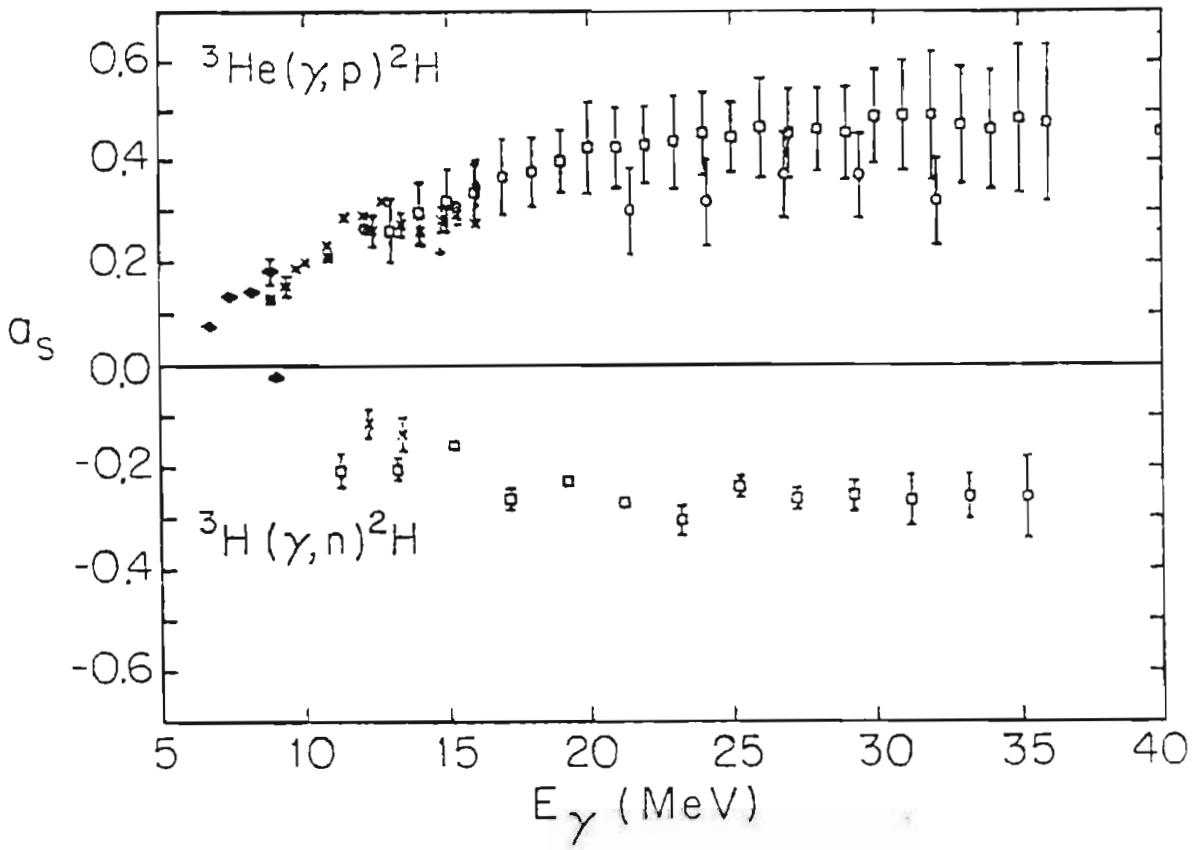

Figure 4-3. Fore-aft asymmetries in angular distributions of cross sections. The $^3H(\gamma,n)^2H$ values are data of this work (X), Skopik et al. (1981) (open squares) and Bösch et al. (1964) (diamond). The $^3He(\gamma,p)^2H$ values are data of King (1983) (X), Kundu et al. (1971, 1972) (open squares), Wölfli et al. (1966) (diamonds), Belt et al. (1970) (dark circles), Skopik et al. (1979) (asterisks), Skopik et al. (1983) (+), Matthews et al. (1974) (triangle) and Anghinolfi et al. (1983) (open circles). The error bars represent statistical uncertainties and are smaller than the symbol in some cases.

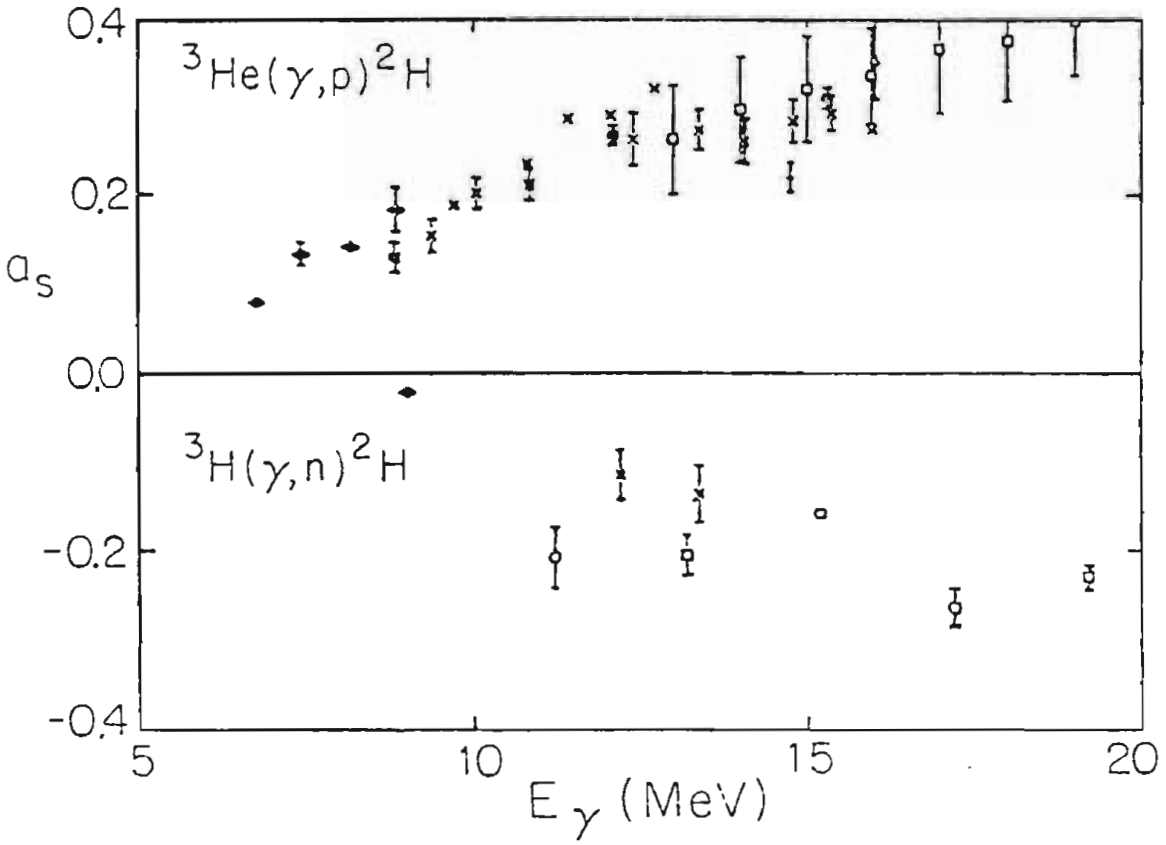

Figure 4-4. Fore-aft asymmetries in angular distributions of cross sections. This is an expanded view of Figure 4-3.

Numerous angular distributions of cross sections have been measured in the ^{3}He case. Published angular distribution coefficients have been employed to calculate, by means of Equations 4-7 and 4-9, the fore-aft asymmetries plotted in Figure 4-3. In most cases only the uncertainties in the coefficients were available, not the full error matrix. Consequently, the uncertainties plotted are only approximately correct. King's ^{3}He asymmetries were calculated directly from measurements of differential cross sections at 55° and 125° and display appropriate uncertainties. Shown in the figure are fifteen $^2H(p,\gamma)^3He$ points from TUNL (King, 1983; Skopik, 1979), nine other $^2H(p,\gamma)^3He$ points (Anghinolfi, 1983; Wölfli, 1966), three $^1H(d,^3He)\gamma$ points (Matthews, 1974; Belt, 1970) and numerous $^3He(e,e'd)^1H$ points (Skopik, 1983; Kundu, 1971). Not shown is the E_γ = 9.83 MeV asymmetry of Skopik et al. (1979) which has been superseded by King's measurement, and the data of Van der Woude et al. (1971) which were claimed to be evidence for a resonance in ^{3}He but later retracted.

The $^2H(n,\gamma)^3H$ data of this work and the $^2H(p,\gamma)^3He$ data of King were measured concurrently at TUNL, over a period of about one year, and employed the same NaI detector systems. This presents the opportunity to compare results of two experiments performed under similar conditions. Ratios of $^2H(n,\gamma)^3H$ to $^2H(p,\gamma)^3He$ asymmetries, at equivalent γ-ray energies, are listed in Table 4-4. The same comparison may be made of the $^3H(e,e'd)n$ data of Skopik et al. (1981) versus $^3He(e,e'd)^1H$ data of Kundu et al. (1971), both measured at the University of Saskatchewan. Displayed in Figure 4-5 are these capture

Table 4-4. Asymmetry ratios of $^{2}H(n,\gamma)^{3}H$ to $^{2}H(p,\gamma)^{3}He$ data.

This work		Xing (1983)		
E_x (MeV)	$a_s(n,\gamma)$	E_x (MeV)	$a_s(p,\gamma)$	$\frac{a_s(n,\gamma)}{a_s(p,\gamma)}$
12.2	-0.115 ± 0.028	12.1	0.290 ± 0.009	-0.40 ± 0.10
13.4	-0.136 ± 0.032	13.4	0.273 ± 0.023	-0.50 ± 0.12

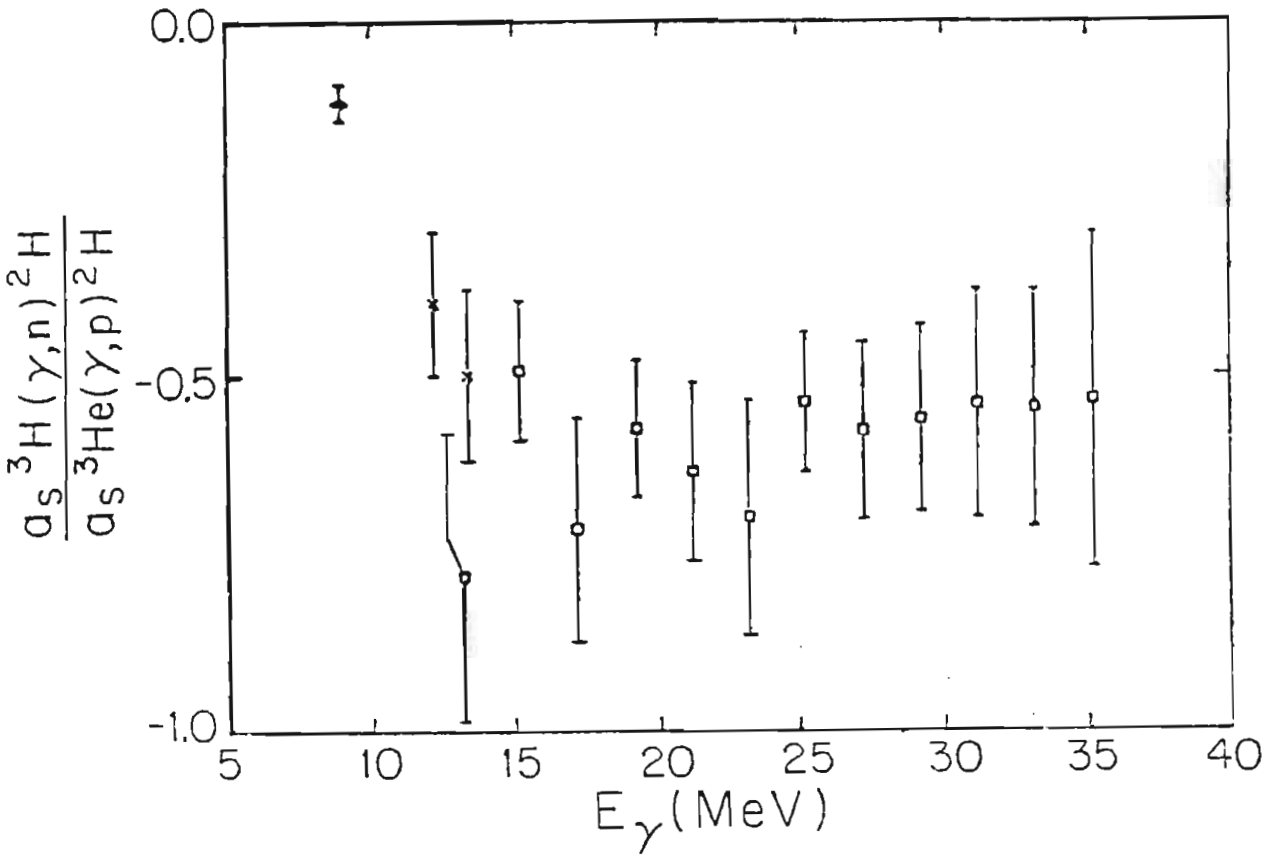

Figure 4-5. $^3H(\gamma,n)^2H$ to $^3He(\gamma,p)^2H$ ratios of fore-aft asymmetries. Asymmetry measurements of this work divided by those of King (1983) (X), Skopik et al. (1981) divided by Kundu et al. (1971, 1972) (open squares) and Bösch et al. (1964) divided by Wölfli et al. (1966) (diamond) are displayed. The error bars represent statistical uncertainties.

and electrodisintegration asymmetry ratios, and one additional point at a γ-ray energy near threshold. This point is derived from $^{3}H(\gamma,n)^{2}H$ data of Bösch et al. (1965) and $^{2}H(p,\gamma)^{3}He$ data of Wölfli et al. (1966). It is the only ratio close to a value of -1/5. The rest of the measurements have approximately the value -1/2. Since two-body direct capture calculations imply the former value, a three-body calculation has been pursued in an effort to obtain -1/2. These calculations are presented in the next chapter.

4.4 Absolute Cross Sections

After correction for electronic and finite-geometry effects (see Chapter 3), the number of corrected γ-rays counts is related to the absolute cross section according to

$$N_{\gamma}(E,\theta) = \sigma_{n,\gamma}(E,\theta)\ \varepsilon_{d}(E)\ \Omega_{d}\ \varepsilon_{t}(E_{r},\theta_{r})\ r_{t}^{-2}\ N_{t}\ N_{n}(E_{d},0^{o}). \qquad 4\text{-}11$$

The symbols of Equation 4-11 are defined in Table 4-5 and their experimental values are listed in Table 4-6. How the values of Table 4-6 were determined is discussed next, followed by a presentation of the resulting absolute cross sections.

The number of target nuclei (N_t) in NE232 was calculated from the manufacturer's specified chemical composition (C_6D_{12}), volume (45 cm^3), density (0.89 g/cm^3) and purity ($N_D/N_C = 1.96$). Since the density and purity could not be reliably determined without extracting the C_6D_{12} from the enclosed glass container, they were accepted at face value. An

Table 4-5. Definitions of symbols in Equation 4-11.

Symbol	Definition
$\varepsilon_d(E)$	Detector efficiency (function of γ-ray energy).
Ω_d	Detector solid angle.
$\varepsilon_t(E_r, \theta_r)$	Scintillating target efficiency for detecting triton recoils (function of recoil energy and angle).
r_t	Distance from the center of the gas cell to the center of the target.
N_t	Number of target nuclei.
$N_n(0^o)$	Number of neutrons incident on the target at 0^o.

Table 4-6. Experimental values of cross section variables applicable to data taken at four neutron bombarding energies. See Table 4-5 for definitions and Table 4-9 for estimated uncertainties.

E_n (MeV)	6.85	9.00	10.80	14.00
ε_d	0.212	0.275	0.214	0.215
Ω_d (msr)	4.50	4.50	4.50	2.27
ε_t	1.00	1.00	1.00	1.00†
r_t (cm)	8.89	8.89	8.89	8.89
$N_t/10^{24}$	2.95	2.95	2.95	2.87
$N_n/10^{11}$	3.54	4.27	5.27	5.28

†Non-scintillating target.

estimate of the volume was obtained by measuring the outer dimensions of the container and assuming uniform thickness throughout. The thickness could be observed through the unpainted bottom of the holder. Agreement with the manufacturer (to 4%) was achieved from this crude estimate. A large uncertainty for the number of target nuclei in NE232 has been employed in calculations of absolute cross sections because some of the manufacturers specifications have not been independently verified. In the case of heavy water, the number of target nuclei was calculated from the measured mass and the manufacturer's specified purity (D_2O/H_2O = 0.9975).

The efficiency (ε_t) of NE232 for detecting a recoiling triton depends on the amount of light collected as the triton radiates away its kinetic energy. It is known that a recoil which remains within the scintillating volume of the target creates a signal large enough to pass through the scintillator discriminator and generate a TAC pulse. Consequently, a calculation of the probability that a recoiling triton remains in the target is an estimate of the scintillator efficiency. A Monte-Carlo program has been written for this purpose. As with FIXER (§3.4), this program randomly selects a neutron source point in the gas cell and a $^2H(n,\gamma)^3H$ reaction point in the target. Since the recoiling tritons were concentrated in a forward cone of less than 5^o relative to the incident-neutron direction, the program approximates that all collisions have a recoil angle $\theta_r = 0^o$. The range of tritons in NE232 was obtained by employing the Bethe-Bloch equation. Table 4-7 presents the calculated efficiency of the scintillator at several recoil

Table 4-7. Results of a Monte Carlo calculation estimating the probability that a recoiling triton will remain in the scintillator. All energies and angles are in the laboratory frame of reference. At neutron bombarding energies of 9.00 MeV and 10.80 MeV only the "worst case" (i.e. greatest recoil energy) results are shown.

E_n (MeV)	θ_γ (degrees)	E_r (MeV)	Range (cm)	Probability
6.85	87.7	2.30	0.007	0.998
9.00	135.0	3.44	0.012	0.997
10.80	135.0	4.12	0.017	0.995

energies. These results are believed to overestimate the loss of tritons from the scintillator. First of all, neutron attenuation has been ignored, an effect which causes more tritons to be born near the incident face of the target, and at the center, than in regions where the tritons are likely to escape the scintillator. Secondly, a triton can exit the scintillator and still deposit much of its energy within. Consequently, the corresponding signal may be large enough to pass through the scintillator discriminator and generate a TAC pulse. The conclusion is that the efficiency of the scintillator was 1.000 ± 0.005 for all the data of the $^{2}H(n,\gamma)^{3}H$ experiment.

Although a 25.4 cm × 25.4 cm NaI detector has an intrinsic efficiency of nearly 100% for detecting γ-rays in the energy domain of this experiment (10.8–15.5 MeV), the efficiency of the overall detection system is substantially less. This is due to γ-ray attenuation in shielding materials between the target and the detector (see Figure 2-3), rejection by the anti-coincidence shield, the solid angle defined by lead collimation and the choice of summing region. The efficiency of the overall system has been measured experimentally by comparing the known yield of a particular resonance to the detected γ-ray yield. The $^{12}C(p,\gamma_0)^{13}N$ reaction has a resonance at $E_p = 14.26$ MeV which produces 15.1 MeV γ-rays. Marrs *et al.* (1975) have reported that the yield at $\theta_\gamma = 125^\circ$ is $(6.83 \pm 0.22) \times 10^{-9}$ γ_0's per incident proton. Wagenaar (1981) has employed this reaction to measure the efficiencies of the NaI detectors. The results for the right detector, as a function of gain in the anti-coincidence circuit, are displayed in

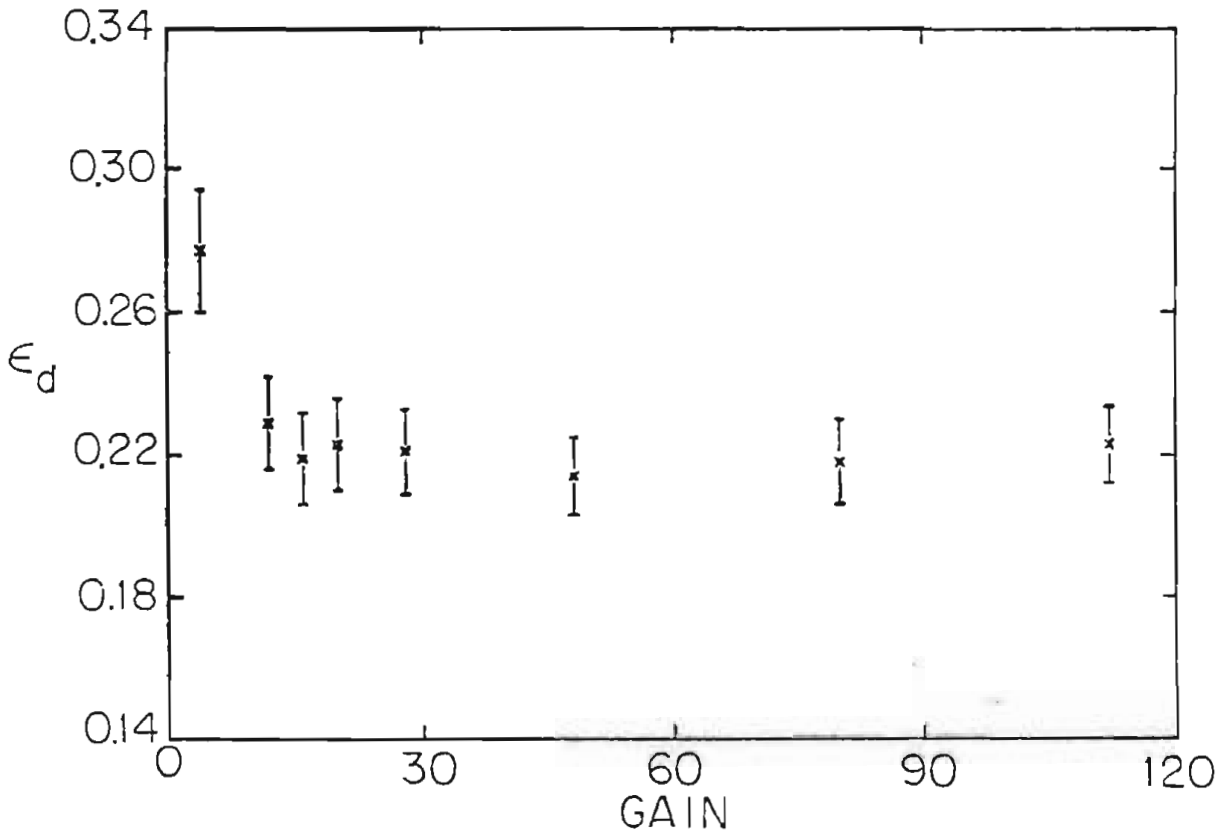

Figure 4-6. Efficiency of NaI detector system as a function of gain in the rejection circuit. The error bars include statistical and systematic uncertainties.

Figure 4-6. In the $^{2}H(n,\gamma)^{3}H$ experiment, the gain of the left detector anti-coincidence circuit was adjusted so that the efficiency of the left detector equaled that of the right detector. Data at neutron bombarding energies 6.85, 10.80 and 14.00 MeV have been taken with the so-called "high rejection" gain of 48, while data at 9.00 MeV were taken with a "low rejection" gain of 4. Finally, the change in detection efficiency as a function of γ-ray energy has been measured with the $^{3}H(p,\gamma)^{4}He$ and $^{13}C(p,\gamma)^{14}N$ reactions (Weller, 1980). The effect is slight between 10.8 and 15.5 MeV, but has been accounted for nonetheless.

The number of neutrons incident on the target at 0° may be expressed as

$$4\text{-}12 \qquad N_n(0^{\circ}) = \frac{Q\,\rho_g\,\ell_g\,\sigma_{d,n}(E_d,0^{\circ})\,f_p(E_d,0^{\circ})}{1.6022 \times 10^{-19}\ C},$$

where Q is the integrated charge of the deuteron beam passing through the gas cell, ρ_g is the density of deuterium atoms in the cell, ℓ_g is the length of the cell, $\sigma_{d,n}(E_d,0^{\circ})$ is the $^{2}H(d,n)^{3}He$ zero degree cross section as a function of deuteron beam energy (Drösg, 1978) and $f_p(E_d,0^{\circ})$ is the correction to the zero degree flux applicable to polarized beams. This last factor is the ratio I/I_p of unpolarized to polarized beam flux. In the Cartesian coordinate representation of Ohlsen (1972), these fluxes are related by

$$4\text{-}13 \qquad I_p = I\,(1 - 0.25\,p_{33}\,A_{zz}(0^{\circ})).$$

As mentioned in §4.2, $p_{33} = 0.69 \pm 0.04$ and $A_{zz}(0^{\circ}) = -0.461 \pm 0.010$ at the deuteron energies corresponding to $E_n = 9.0$ and 14.0 MeV. This

implies that $f_p = 0.93 \pm 0.02$.

Experimental $^2H(n,\gamma)^3H$ ninety degree differential cross sections and total cross sections, which will be compared with data of other photonuclear experiments, are listed in Table 4-8. All differential cross sections measured in this work are presented in Appendix C. The cross sections of Table 4-8 are either the result of direct measurement or the result of a constrained fit to an angular distribution. Assumptions about a_2 and a_4 were made in calculating the total cross section at $E_\gamma = 10.81$ MeV. In all cases the uncertainties shown are statistical. On the assumption of time reversal invariance, cross sections for the inverse reaction $^3H(\gamma,n)^2H$ may be calculated from capture cross sections via detail balance. The relationship has the form (see Hayward (1970))

$$4\text{-}14 \qquad \sigma_{\gamma,n_0} = 2\, m_n\, c^2 \frac{(2\, J_{A-1} + 1)}{(2\, J_A + 1)} \frac{(A - 1)}{A} \frac{(E_x - Q)}{E_x^2} \sigma_{n,\gamma_0}.$$

Values applicable in this case are $A = 3$, $J_A = 1/2$, $J_{A-1} = 1$, $Q = 6.257$ MeV, $E_x = E_\gamma$ and $m_n c^2 = 939.6$ MeV. The calculated photodisintegration cross sections corresponding to the measured capture cross sections are in parentheses in Table 4-8. They will be useful in comparing with results from other experiments.

Besides statistical uncertainties, systematic uncertainties must be considered when absolute measurements are performed in an experiment. Estimates of the systematic uncertainties affecting the absolute cross section in the $^2H(n,\gamma)^3H$ experiment are listed in

Table 4-8. $^{2}H(n,\gamma)^{3}H$ 90^{o} (c.m.) differential cross sections and total cross sections. Uncertainties are statistical. Shown in parentheses are the corresponding $^{3}H(\gamma,n)^{2}H$ cross sections obtained from a detail balance calculation.

E_γ (MeV)	$\sigma(90^o)^a$ (μb/sr)	$\sigma(90^o)^b$ (μb/sr)	σ^c (μb)	σ^d (μb)
10.81	1.33 ± 0.029			11.5 ± 0.25
	(104. ± 2.3)			(902. ± 20.)
12.23		1.31 ± 0.046	11.5 ± 0.23	
		(105. ± 3.7)	(925. ± 18.)	
13.43	1.21 ± 0.062	1.20 ± 0.045	10.7 ± 0.25	
	(96.9 ± 5.0)	(96.1 ± 3.6)	(857. ± 20.)	
15.50		0.92 ± 0.15	7.98 ± 1.23	
		(71.3 ± 12.)	(618. ± 95.)	

[a] Measured directly.

[b] From the constrained fit to the angular distribution.

[c] $\sigma = 4\pi A_0$.

[d] $\sigma = \dfrac{4\pi\,\sigma(90^o)}{1 - \frac{1}{2}(-0.9)}$.

Table 4-9. Sources of systematic uncertainty in the $^{2}H(n,\gamma)^{3}H$ experiment.

Source of Uncertainty	Uncertainty (%)
Choice of summing region	3
Correction for accidental stops in TAC	2
Correction for finite geometry	5
$\varepsilon_d\Omega_d$ (high rejection; low rejection)	4; 8
ε_t (NE232)	2
r^{-2}	2
N_t (NE232; D_2O)	5; 1
Q	3
ρ_g	2
f_g	2
$\sigma_{d,n}$	2
f_p	2

Table 4-9. These have been added, in percent quadrature, to the previously quoted statistical uncertainties and the overall values are used in the following comparisons.

The total cross sections of this work are displayed in Figure 4-7. They are presented as photodisintegration cross sections for comparison with other experimental results. Total cross sections of Skopik et al. (1981) were calculated from measurements at 55° and 125° according to $\sigma_T = 2\ \pi\ [\sigma(55^{\circ}) + \sigma(125^{\circ})]$, while those of Kosiek et al. (1966) and Pfeiffer (1968) were calculated from 90° measurements according to $\sigma_T = (8/3)\ \pi\ \sigma(90^{\circ})$. The data of Bösch et al. (1965) and Faul (et al.) (1980, 1981) were $4\ \pi$ measurements. The agreement of the capture data of this work with the photodisintegration data of Faul is excellent.

Ratios of $^3He(\gamma,p)^2H$ to $^3H(\gamma,n)^2H$ 90° (c.m.) differential cross sections, at equivalent γ-ray energies, are listed in Table 4-10. The ratios are derived from the neutron capture measurements of this work and the proton capture measurements of Skopik et al. (1979). These data are plotted in Figure 4-8 along with electrodisintegration ratios reported by Skopik et al. (1981). Most of the points lie within one standard deviation of the value 1.0.

4.5 Transition Matrix Element Analysis

Experimental values of Legendre and associated Legendre expansion coefficients have been extracted from fits to angular distributions of

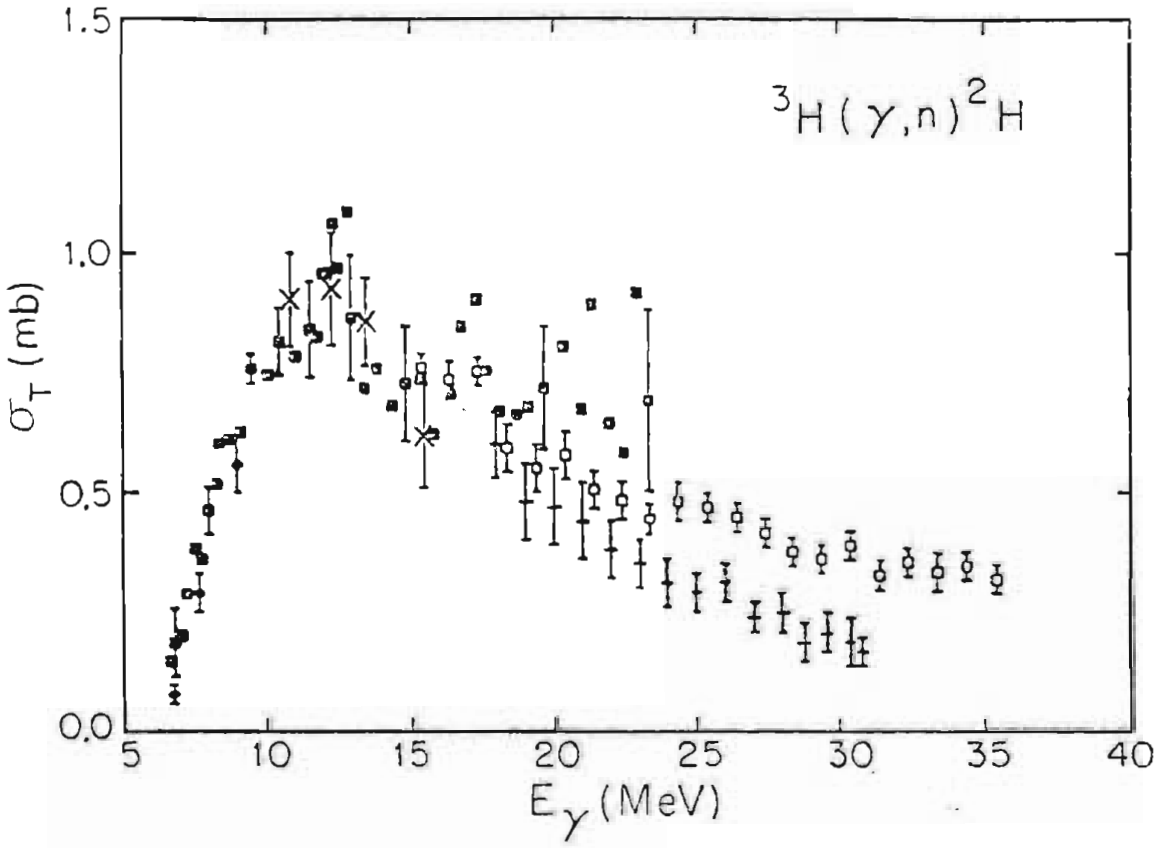

Figure 4-7. Total cross sections. The $^2H(n,\gamma)^3H$ cross sections of this work (X) are compared, after detail balancing, with $^3H(\gamma,n)^2H$ cross sections of Bösch et al. (1964) (diamonds), Faul et al. (1980, 1981) (dark squares), Skopik et al. (1981) (open squares), Kosiek et al. (1966) (+) and Pfeiffer (1968) (+). The error bars include statistical and systematic uncertainties. For clarity, only selected error bars of Faul's data are shown.

Table 4-10. $^{3}He(\gamma,p)^{2}H$ to $^{3}H(\gamma,n)^{2}H$ differential cross section ratios at 90° in the center of mass.

This work		Skopik (1979)		$\frac{\sigma(90^{\circ})(\gamma,p)}{\sigma(90^{\circ})(\gamma,n)}$
E_x (MeV)	$\sigma(90^{\circ})$ (μb/sr)	E_x (MeV)	$\sigma(90^{\circ})$ (μb/sr)	
10.8	104. ± 11.0	10.8	117. ± 9.4	1.12 ± 0.15
12.2	105. ± 13.6	12.1	113. ± 9.0	1.03 ± 0.16
13.4	96.1 ± 10.6	13.4	103. ± 10.3	1.07 ± 0.16
15.5	71.3 ± 13.5	15.3	88.7 ± 8.9	1.24 ± 0.27

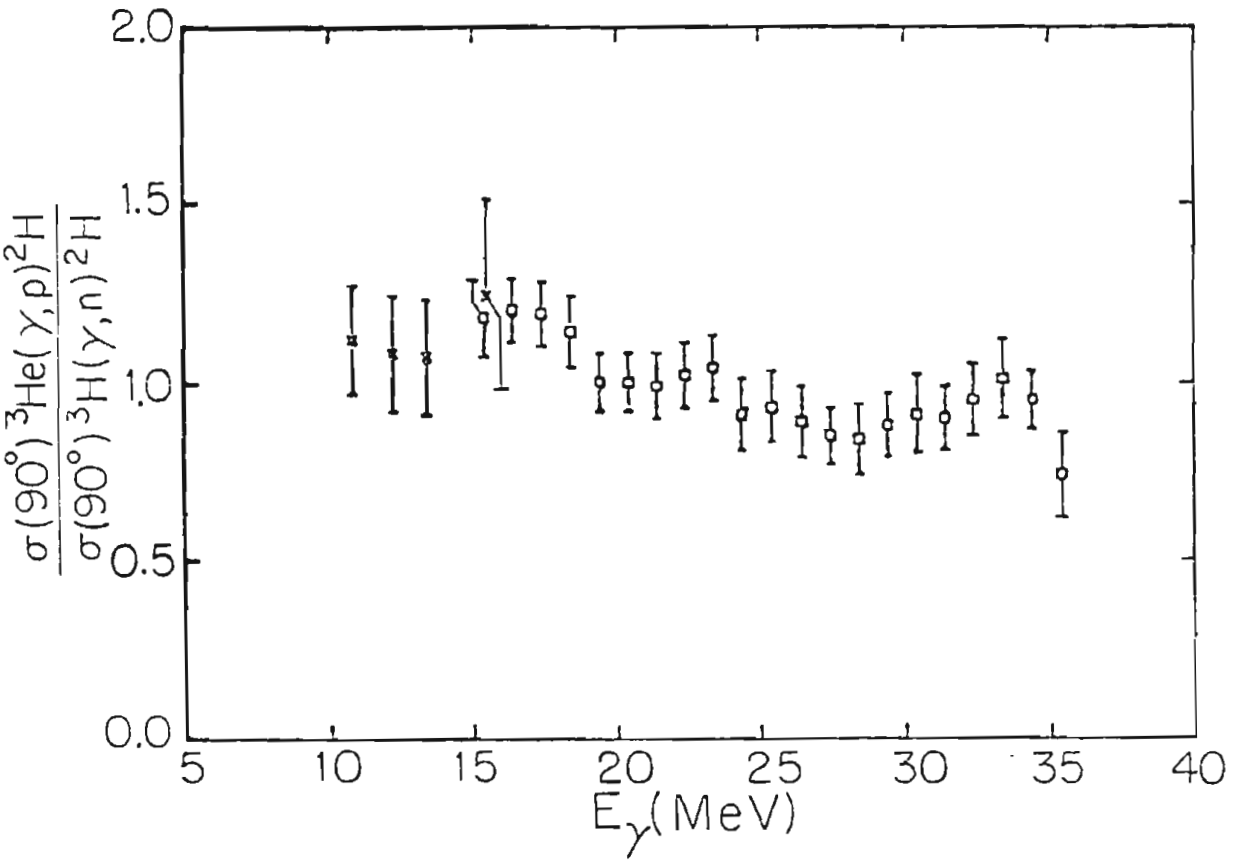

Figure 4-8. $^3H(\gamma,n)^2H$ to $^3He(\gamma,p)^2H$ ratios of differential cross sections at 90° (c.m.). Measurements of this work divided by data of King (1983) (see Table 4-10) have been detail balanced and are displayed as (X). Ratios quoted by Skopik et al. (1981) are also shown (open squares). The error bars include statistical and systematic uncertainties.

cross sections and analyzing powers (§4.2). It is possible to extend the analysis of the angular distributions a step further. Transition amplitudes and phases can be determined from a transition matrix element analysis of the data (Seyler, 1979; Weller, 1980). Because of the large number of amplitudes and phases consistent with angular momentum conservation in the $^{2}H(n,\gamma)^{3}H$ reaction, it was necessary to make some simplifying physical assumptions.

The relationships between transition matrix elements and observables depend on the selected angular momentum coupling representation. The channel spin coupling scheme has been employed in the analysis of the polarized E_n = 9 MeV data of this experiment. Let the angular momenta of the $^{2}H(\vec{n},\gamma)^{3}H$ reaction be specified as $\vec{a}(\vec{x},\vec{L})\vec{c}$, where $\vec{a}$ is the spin of the target, $\vec{x}$ the spin of the incident projectile, $\vec{L}$ the multipolarity of the emitted γ-ray and $\vec{c}$ the spin of the residual nucleus. Then

$$\vec{x} + \vec{a} = \vec{s}$$
$$\vec{l} + \vec{s} = \vec{j} \qquad (4\text{-}15)$$
$$\vec{L} + \vec{c} = \vec{j},$$

where $\vec{s}$ is the channel spin of the reaction, $\vec{l}$ is the orbital angular momentum of the incident projectile and $\vec{j}$ is the total angular momentum of the system. With this coupling scheme the a_k and b_k coefficients are (Seyler, 1979; Weller, 1980)

$$a_k = \sum_t \sum_{t'} C_1(t,t',c,k)\ \mathrm{Re}(RR'^{*}) \qquad (4\text{-}16)$$

and

$$4\text{-}17 \qquad b_k = \frac{3\left[x(2x+1)(2k+1)\right]^{1/2}}{\left[(x+1)k(k+1)\right]^{1/2}} \sum_t \sum_{t'} C_2(t,t',c,k)\ \mathrm{Re}(iRR'^*),$$

where R is the reduced transition matrix element, C_1 and C_2 are constants of the angular momentum algebra, and the sum over t represents sums over L, j, ℓ, s and the two modes of radiation (electric and magnetic). The reduced transition matrix element is proportional the radial matrix element,

$$4\text{-}18 \qquad R \propto \langle f|H_{int}|i\rangle,$$

where $|i\rangle$ represents the continuum initial state (neutron plus deuteron), $\langle f|$ represents the bound final state (^{3}H) and H_{int} is the electromagnetic operator. Since R is a complex number, it is common to decompose it into a real amplitude, $^{2s+1}\ell_j$, times the exponential of the corresponding real phase, $\exp(i\phi_{^{2s+1}\ell_j})$.

The electromagnetic transition operator which connects the initial and final states of the ^{2}H(n,γ)^{3}H reaction may be separated into an electric part and a magnetic part (see next chapter). The electric part of the operator reduces to a form proportional to $(kr)^L$ (Blatt, 1952) if one invokes Siegert's Theorem (Siegert, 1937) and the long wavelength approximation. The latter requires that for r $\simeq$ nuclear size and k the wave number of the γ-ray, kr<<1. At the energies of this experiment kr $\simeq 0.05\ \mathrm{fm}^{-1} \times 2\ \mathrm{fm} = 0.1$. Amplitudes of electric transition matrix elements rapidly diminish as the photon multipolarity increases because of $(kr)^L$. A direct capture calculation (see Chapter 5) shows that E3

amplitudes are negligibly small in the $^{2}H(\vec{n},\gamma)^{3}H$ reaction at 9 MeV. Consequently, only electric dipole (E1) and electric quadrupole (E2) transitions have been considered in this analysis. The $\sin^{2}(\theta)$ shape of the angular distribution of cross sections is indicative of predominantly E1 radiation, while the asymmetry about 90° implies the presence of E2 radiation.

The magnetic part of the electromagnetic operator similarly decreases with increasing multipolarity (Blatt, 1952). In addition, there exists an extra factor of $\sqrt{10}\hbar/(McR)$, where M is the projectile mass and R is the radius of the nucleus (DeBenedetti, 1964). This factor is approximately $(hc)/(Mc^{2}R) = (200\ \text{MeV-fm})/(2 \times 10^{3}\ \text{MeV} \cdot 2\ \text{fm}) = 1/20$. Magnetic transition amplitudes are more than an order of magnitude smaller than electric amplitudes of the same L. Hence M2 and higher magnetic multipoles are not expected to contribute significant transition strength. Furthermore, measurements of this experiment have shown that the a_{3} Legendre coefficient is equal to minus the a_{1} coefficient, implying little or no M1 strength. Hendry and Phillips (1973) have calculated the M1 strength in the energy domain of this experiment and have determined it to be negligibly small.

The extraction of amplitudes and phases from fits to the polarized data at $E_{n} = 9$ MeV has been restricted to simply E1 and E2 radiation. Displayed in Figure 4-9 are the allowed amplitudes arising from E1 and E2 transitions in the $^{2}H(\vec{n},\gamma)^{3}H$ reaction. Direct capture calculations indicate that the E2(s=3/2) transitions and the E1(ℓ=3) transition may be neglected. This is not surprising. The ^{3}H wave function is

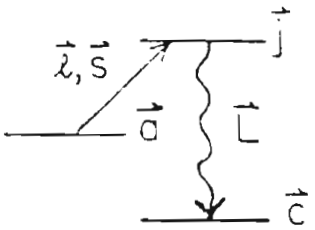

$$\vec{\nu} + \vec{a} = \vec{s}$$
$$\vec{l} + \vec{s} = \vec{j}$$
$$\vec{L} + \vec{c} = \vec{j}$$

E1

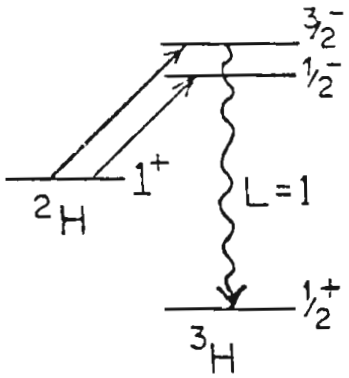

l	s	j	amp
1	1/2	1/2	$^2p_{1/2}$
1	1/2	3/2	$^2p_{3/2}$
1	3/2	1/2	$^4p_{1/2}$
1	3/2	3/2	$^4p_{3/2}$
3	3/2	3/2	$^4f_{3/2}$

E2

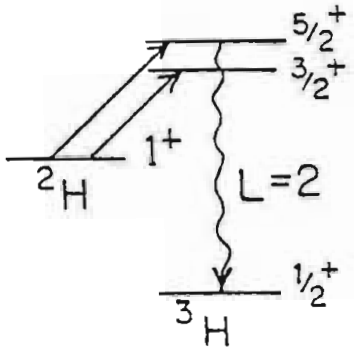

l	s	j	amp
0	3/2	3/2	$^4s_{3/2}$
2	1/2	3/2	$^2d_{3/2}$
2	1/2	5/2	$^2d_{5/2}$
2	3/2	3/2	$^4d_{3/2}$
2	3/2	5/2	$^4d_{5/2}$
4	3/2	5/2	$^4g_{5/2}$

Figure 4-9. Allowed E1 and E2 transitions in the $^2H(n,\gamma)^3H$ reaction.

predominantly $^2S_{1/2}$ with less than 10% $^4D_{1/2}$ (§1.2). The important transitions should therefore be E1 to the $^2S_{1/2}$ state, E1 to the $^4D_{1/2}$ state and E2 to the $^2S_{1/2}$ state. In addition, spin-flip ($\Delta s \neq 0$) strength is weak in the $^2H(n,\gamma)^3H$ reaction. This is because the electric operator (see Equation 5-1) does not couple states of different spin and because spin-orbit interactions are weak in both the initial continuum state (King, 1983) and the final ^3H state (Derrick, 1960). Since the E2(s=3/2) to $^2S_{1/2}$ transitions are spin-flip transitions, they may be neglected. The $^4f_{3/2}$ amplitude is small due to the angular momentum barrier.

There remain six amplitudes ($^2p_{1/2}$, $^2p_{3/2}$, $^4p_{1/2}$, $^4p_{3/2}$, $^2d_{3/2}$ and $^2d_{5/2}$) with five relative phases among them - a total of eleven unknowns. From previously discussed Legendre and associated Legendre fits, it is evident that the data at E_n = 9 MeV are not precise enough to determine eleven unknowns. Only eight parameters were determinable from those fits - A_0, a_1, a_2, a_3, a_4, b_1, b_2 and b_3. The number of unknowns can be reduced by combining some of the amplitudes. On the basis of the weak spin-orbit coupling in the $^2H(n,\gamma)^3H$ reaction, the relative phase between amplitudes of the same ℓ and s, but different j, may be assumed to be equal. Therefore, define $^2p \equiv {}^2p_{1/2} + {}^2p_{3/2}$, $^4p \equiv {}^4p_{1/2} + {}^4p_{3/2}$ and $^2d \equiv {}^2d_{3/2} + {}^2d_{5/2}$. In terms of these three amplitudes and their two relative phases the angular distribution coefficients are

4-19 $\quad 1. = 6.00\ (^2p)^2 + 6.00\ (^4p)^2 + 10.00\ (^2d)^2$ Normalization

$$a_1 = 20.78\ {}^2p\ {}^2d \cos(\phi_{2_d} - \phi_{2_p})$$

$$a_2 = -6.00\ (^2p)^2 + 7.14\ (^2d)^2 + 2.87\ (^4p)^2$$

$$a_3 = -20.78\ ^2p\ ^2d \cos(\phi_{2_d} - \phi_{2_p})$$

$$a_4 = -17.14\ (^2d)^2$$

$$b_1 = -6.80\ ^4p\ ^2d \sin(\phi_{2_d} - \phi_{4_p})$$

$$b_2 = 3.92\ ^2p\ ^4p \sin(\phi_{4_p} - \phi_{2_p})$$

$$b_3 = -4.52\ ^4p\ ^2d \sin(\phi_{2_d} - \phi_{4_p})$$

$$b_4 = 0.00.$$

The polarized $^2H(\vec{n},\gamma)^3H$ angular distribution data at E_n = 9.00 MeV were fit to the three amplitudes and two phases via the relationships of Equations 4-19 and the angular distribution expansions of Equations 4-1 and 4-2. This analysis is identical to the transition matrix analysis performed by King for $^2H(\vec{p},\gamma)^3He$ data at E_p = 8.00 and 15.94 MeV. The results of this work and those of King (1984) are listed in Table 4-11, where the amplitudes are presented as percentage contributions to the cross section and the phases are relative to the ^2p matrix element. Comparison of the $^2H(n,\gamma)^3H$ and $^2H(p,\gamma)^3He$ results indicates that corresponding amplitudes of the two reactions are approximately equal to each other. On the basis of two-body direct capture calculations, this is expected for the E1 amplitudes but surprising for the E2 amplitude. The theory predicts a ratio of $\sigma_{n,\gamma}(E2)/\sigma_{p,\gamma}(E2) = (-1/5)^2 = 1/25$.

Theoretical calculations relevant to this $^2H(n,\gamma)^3H$ study shall now be considered.

Table 4-11. Transition amplitudes (as a percentage of cross section) and their relative phases obtained from fits to angular distributions of cross sections and analyzing powers.

	This work $^2H(n,\gamma)^3H$	King (1984) $^2H(p,\gamma)^3He$	
E_x (MeV)	12.2	10.8	16.1
$\sigma(^2p)$ (%)	94.0 ± 3.4	95 ± 3	92 ± 2
$\sigma(^4p)$ (%)	2.7 ± 2.5	3 ± 2	5 ± 3
$\phi_{4_p} - \phi_{2_p}$ (degrees)	3 ± 16 or 177 ± 16	8 ± 6 or 172 ± 13	7 ± 6 or 173 ± 12
$\sigma(^2d)$ (%)	3.3 ± 2.7	2 ± 1	3 ± 2
$\phi_{2_d} - \phi_{2_p}$ (degrees)	-105 ± 8 or 105 ± 8	-26 ± 29 or 26 ± 20	-2 ± 26 or 3 ± 26
χ^2	0.9	1.0	1.0

5 THEORETICAL CALCULATIONS

5.1 Introduction

The $^{2}H(n,\gamma)^{3}H$ reaction is a transition from an initial scattering state to the ground state of ^{3}H via interaction with the electromagnetic field. The theory of direct capture reactions (Brown, 1964; Rolfs, 1973; Dietrich, 1977) describes such transitions. In this theory the initial state may be described by a distorted plane wave, the final state by a standing wave with specific orbital angular momentum and the interaction Hamiltonian by the electromagnetic operator. Reaction observables are expressed in terms of transition matrix elements according to angular distribution relations such as Equations 4-16 and 4-17. This chapter is devoted to: (1) Describing the form of the electromagnetic operator; (2) presenting the results of two-body direct capture calculations which treat the nucleon-deuteron system as two point particles; and (3) presenting the results of a three-body direct capture calculation which includes the internal coordinates of the deuteron.

5.2 The Electromagnetic Operator

The electromagnetic operator commonly employed in direct capture calculations at low energies is derived from the general form by: (1) Splitting the operator into an electric and magnetic part; (2) replacing the nuclear current density with the charge density in the electric part

of the operator (Siegert's Theorem); (3) expanding in terms of Bessel functions; and (4) applying the long wavelength approximation. In the case of the electric operator this derivation leads to a simplified form proportional to $q_L^{(eff)} \rho^L$ (Weller, 1980), where ρ is the distance between the incident-projectile and target-nucleus, $q_L^{(eff)}$ is the effective charge of the projectile and L is the multipolarity of the emitted γ-ray. The two-body calculations described in §5.3 were performed with the program HIKARI (Kitazawa, 1980) and employed this form of the electric operator.

One may equally well arrive at a usable form of the operator by expanding in a Taylor series instead of in Bessel functions. This form has proved more suitable for the three-body calculation of this work because of the wave functions involved (see §5.4). In addition, this approach has the virtue of clearly displaying the difference between effective charges in the two-body versus three-body calculations. For this reason the derivation of the operator presented here will be according to the method of Foldy (1953) which employs the Taylor series expansion. The reader is referred to Blatt (1955) and the above references on direct capture theory for more detail about the Bessel function approach.

The emission of one photon in a particle-capture reaction may be described by an interaction Hamiltonian of the form

$$H_{int} = -\int \vec{j}(\vec{r}) \cdot \vec{A}(\vec{r}) \, d\vec{r}, \qquad 5\text{-}1$$

where $\vec{j}(\vec{r})$ is the nuclear current density, $\vec{A}(\vec{r})$ is the vector potential

and $\vec{r}$ is the position coordinate with respect to the center-of-mass of the system. In the radiation gauge the vector potential is

$$\vec{A} = \vec{\varepsilon}\, e^{i\vec{k}\cdot\vec{r}}, \tag{5-2}$$

where $\vec{\varepsilon}$ and $\vec{k}$ are the polarization and wave vectors respectively of the emitted photon. $\vec{A}(\vec{r})$ satisfies the gauge condition

$$\nabla\cdot\vec{A}(\vec{r}) = 0. \tag{5-3}$$

In addition, the following transversality condition holds,

$$\vec{k}\cdot\vec{\varepsilon} = 0. \tag{5-4}$$

Substituting for $\vec{A}(\vec{r})$ in Equation 5-1 gives

$$H_{int} = -\int \vec{j}(\vec{r})\cdot\vec{\varepsilon}\, e^{i\vec{k}\cdot\vec{r}}\, d\vec{r}. \tag{5-5}$$

Making use of the identity

$$\vec{\varepsilon}\, e^{i\vec{k}\cdot\vec{r}} = \int_0^1 \left[\nabla(\vec{\varepsilon}\cdot\vec{r}\, e^{is\vec{k}\cdot\vec{r}}) - is\vec{r}\times(\vec{k}\times\vec{\varepsilon})\, e^{is\vec{k}\cdot\vec{r}} \right] ds, \tag{5-6}$$

one separates the operator into an electric part (first term) and a magnetic part (second term). Magnetic transitions do not contribute significantly in the $^2H(n,\gamma)^3H$ reaction at the energies of this experiment (see §4.5), so only the first term shall be considered further. The electric part of the interaction Hamiltonian is

$$H^e_{int} = -\int_0^1\int \vec{j}(\vec{r})\cdot\nabla(\vec{\varepsilon}\cdot\vec{r}\, e^{is\vec{k}\cdot\vec{r}})\, ds\, d\vec{r}. \tag{5-7}$$

Making use of the vector identity $\vec{F}\cdot\nabla f = -f\nabla\cdot\vec{F} + \nabla\cdot f\vec{F}$ one obtains

$$5\text{-}8 \qquad H^{e}_{int} = -\int_{0}^{1}\int \left[-(\vec{\varepsilon}\cdot\vec{r}\; e^{is\vec{k}\cdot\vec{r}})\; \nabla\cdot\vec{j}(\vec{r}) + \nabla\cdot(\vec{\varepsilon}\cdot\vec{r}\; e^{is\vec{k}\cdot\vec{r}})\vec{j}(\vec{r})\right] ds\; d\vec{r}.$$

Applying the divergence theorem to the second term of H^{e}_{int} one obtains a surface integral involving $\vec{j}\cdot\vec{n}$, where $\vec{n}$ is normal to the surface. Since charge is conserved in the $^{2}H(n,\gamma)^{3}H$ reaction, this integral vanishes. Hence,

$$5\text{-}9 \qquad H^{e}_{int} = \int_{0}^{1}\int (\vec{\varepsilon}\cdot\vec{r}\; e^{is\vec{k}\cdot\vec{r}})\; ds\; \nabla\cdot\vec{j}(\vec{r})\; d\vec{r},$$

or after evaluating the integral over the dummy variable s,

$$5\text{-}10 \qquad H^{e}_{int} = \int \frac{\vec{\varepsilon}\cdot\vec{r}}{i\vec{k}\cdot\vec{r}}\,(e^{i\vec{k}\cdot\vec{r}} - 1)\; \nabla\cdot\vec{j}(\vec{r})\; d\vec{r}.$$

The current density in Equation 5-10 may be replaced by employing the continuity equation

$$5\text{-}11 \qquad \nabla\cdot\vec{j}(\vec{r}) + \frac{i}{\hbar c}\left[H,\rho(\vec{r})\right] = 0$$

as suggested by Siegert (1937). Here H is the nuclear Hamiltonian and $\rho(\vec{r})$ is the nuclear charge density. So

$$5\text{-}12 \qquad H^{e}_{int} = \frac{-i}{\hbar c}\int \frac{\vec{\varepsilon}\cdot\vec{r}}{i\vec{k}\cdot\vec{r}}\,(e^{i\vec{k}\cdot\vec{r}} - 1)\left[H,\rho(\vec{r})\right] d\vec{r}$$

and the transition matrix element is

$$5\text{-}13 \qquad \langle f|H^{e}_{int}|i\rangle = \langle f|\left[H,\ \frac{-i}{\hbar c}\int\rho(\vec{r})\ \frac{\vec{\varepsilon}\cdot\vec{r}}{i\vec{k}\cdot\vec{r}}\,(e^{i\vec{k}\cdot\vec{r}} - 1)\ d\vec{r}\right]|i\rangle$$

$$\propto -\frac{i(E_f - E_i)}{\hbar c}\langle f|\int\rho(\vec{r})\ \frac{\vec{\varepsilon}\cdot\vec{r}}{i\vec{k}\cdot\vec{r}}\,(e^{i\vec{k}\cdot\vec{r}} - 1)\ d\vec{r}|i\rangle.$$

Since $\vec{k}\cdot\vec{r} \ll 1$ at the energies of this experiment, one may expand the exponential in a Taylor series. The integral thus becomes

$$5\text{-}14 \qquad I = \int \rho(\vec{r}) \, \frac{\vec{\varepsilon}\cdot\vec{r}}{i\vec{k}\cdot\vec{r}} \left(1 + i\vec{k}\cdot\vec{r} + \frac{1}{2}\,(i\vec{k}\cdot\vec{r})^2 + \ldots - 1\right) d\vec{r}$$

$$= \int \rho(\vec{r}) \; \vec{\varepsilon}\cdot\vec{r} \left(1 + \frac{1}{2}\,(i\vec{k}\cdot\vec{r}) + \ldots\right) d\vec{r}.$$

The first term is the dipole part of the electric operator, the second the quadrupole part, etc. Substituting point charges for $\rho(\vec{r})$ and neglecting terms higher than quadrupole one obtains

$$5\text{-}15 \qquad I \simeq \sum_{j=1}^{j=A} \frac{e}{2}\,(1 + \tau_3^j)\;(\vec{\varepsilon}\cdot\vec{r}_j + \frac{i}{2}\,\vec{\varepsilon}\cdot\vec{r}_j\;\vec{k}\cdot\vec{r}_j),$$

where the sum is over all nucleons and the isospin projection τ_3^j equals +1 for protons and -1 for neutrons.

Now consider the particular case of nucleon capture to a final state of either ^{3}H or ^{3}He. In order to demonstrate the difference between the two-body versus the three-body forms of the operator it is convenient to define the following coordinates. Let $\vec{\rho}$ be the position vector from the center-of-mass of the deuteron to the incident-projectile, and let $\vec{r}$ be the internal coordinate of the deuteron pointing towards the same-type nucleon as the incident-projectile (see Figure 5-1). Although these definitions of $\vec{\rho}$ and $\vec{r}$ may seem arbitrary (as applied to ^{3}H versus ^{3}He), they are consistent with the isospin formalism which was employed in the three-body calculation described in §5.4 (Lehman, 1984). In terms of these new coordinates the center-of-mass coordinates $\vec{r}_j$ of Equation 5-15 are

$$5\text{-}16 \qquad \vec{r}_1 = \frac{2}{3}\,\vec{\rho}$$

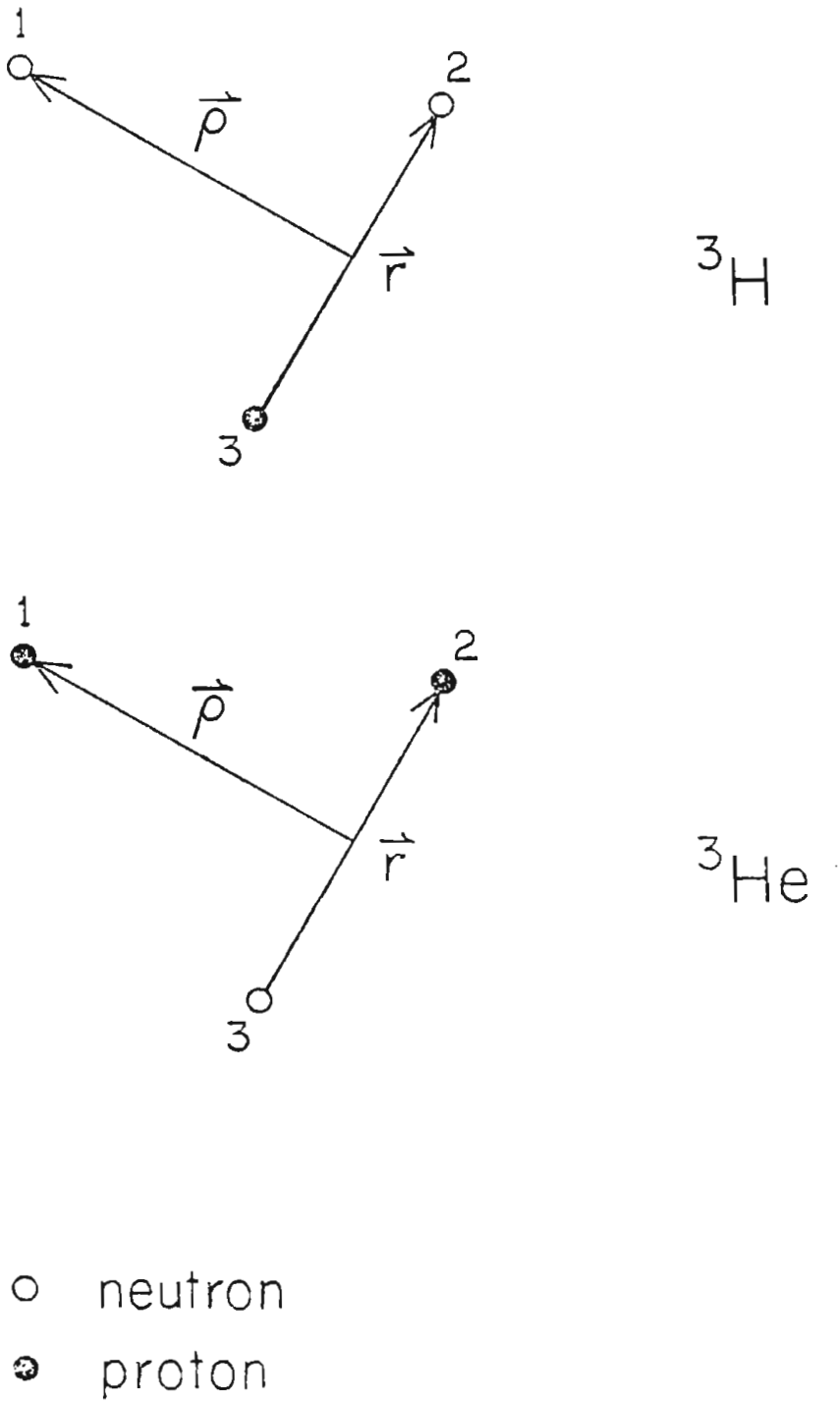

Figure 5-1. Coordinates for the ^{3}H and ^{3}He three-body systems.

$$\vec{r}_2 = \frac{1}{2}\vec{r} - \frac{1}{3}\vec{\rho}$$

$$\vec{r}_3 = -\frac{1}{2}\vec{r} - \frac{1}{3}\vec{\rho},$$

where the labeling (1, 2, and 3) is according to Figure 5-1. After substitution for $\vec{r}_j$ in Equation 5-15 the dipole plus quadrupole parts of the integrand are

5-17 $$(-\frac{1}{3}\vec{\varepsilon}\cdot\vec{\rho} - \frac{1}{2}\vec{\varepsilon}\cdot\vec{r}) + \frac{i}{2}\left[\frac{1}{9}\vec{\varepsilon}\cdot\vec{\rho}\,\vec{k}\cdot\vec{\rho} + \frac{1}{6}\vec{\varepsilon}\cdot\vec{\rho}\,\vec{k}\cdot\vec{r} + \frac{1}{6}\vec{\varepsilon}\cdot\vec{r}\,\vec{k}\cdot\vec{\rho} + \frac{1}{4}\vec{\varepsilon}\cdot\vec{r}\,\vec{k}\cdot\vec{r}\right]$$

in the case of ^{3}H, and

5-18 $$(\frac{1}{3}\vec{\varepsilon}\cdot\vec{\rho} + \frac{1}{2}\vec{\varepsilon}\cdot\vec{r}) + \frac{i}{2}\left[\frac{5}{9}\vec{\varepsilon}\cdot\vec{\rho}\,\vec{k}\cdot\vec{\rho} - \frac{1}{6}\vec{\varepsilon}\cdot\vec{\rho}\,\vec{k}\cdot\vec{r} - \frac{1}{6}\vec{\varepsilon}\cdot\vec{r}\,\vec{k}\cdot\vec{\rho} + \frac{1}{4}\vec{\varepsilon}\cdot\vec{r}\,\vec{k}\cdot\vec{r}\right]$$

in the case of ^{3}He.

Two-body direct capture calculations treat the target nucleus of the initial state, and the core of the final state, as point particles. In the A=3 case this corresponds to the internal coordinate of the deuteron being zero ($\vec{r} = 0$). Consequently the dipole and quadrupole terms of the two-body electromagnetic operator are

5-19 $$-\frac{1}{3}\vec{\varepsilon}\cdot\vec{\rho} + \frac{i}{2}\left[\frac{1}{9}\vec{\varepsilon}\cdot\vec{\rho}\,\vec{k}\cdot\vec{\rho}\right]$$

in the case of ^{3}H, and

5-20 $$\frac{1}{3}\vec{\varepsilon}\cdot\vec{\rho} + \frac{i}{2}\left[\frac{5}{9}\vec{\varepsilon}\cdot\vec{\rho}\,\vec{k}\cdot\vec{\rho}\right]$$

in the case of ^{3}He. The factors -1/3 and 1/9 are the so-called dipole and quadrupole effective charges, respectively, of the incident-neutron in the $^{2}H(n,\gamma)^{3}H$ reaction. Similarly, 1/3 and 5/9 are the dipole and quadrupole effective charges, respectively, of the incident-proton in the $^{2}H(p,\gamma)^{3}He$ reaction. It is clear from Equations 5-19 and 5-20 that if the same initial and final state nuclear wave functions are employed in calculations of $^{2}H(n,\gamma)^{3}H$ and $^{2}H(p,\gamma)^{3}He$ matrix elements, E1 matrix elements of the two reactions should be of the same magnitude but different sign, while the $^{2}H(n,\gamma)^{3}H$ E2 matrix elements should be 1/5 those of the $^{2}H(p,\gamma)^{3}He$ reaction. There are also energy-dependent factors which enter into the calculations, however they are approximately equal in the two reactions at most γ-ray energies. Variations appear only at low γ-ray energies because of the difference in reaction Q-values (6.257 MeV for $^{2}H(n,\gamma)^{3}H$ versus 5.494 MeV for $^{2}H(p,\gamma)^{3}He$). It shall be shown that a discrepancy exists between the E2 predictions of two-body direct capture calculations and the E2 strength implied by experimental observables.

5.3 Two-Body Direct Capture Calculations

Two-body direct capture calculations have been performed for the $^{2}H(n,\gamma)^{3}H$ and $^{2}H(p,\gamma)^{3}He$ reactions in order to compare theoretical predictions with the experimental measurements discussed in Chapter 4. The program HIKARI (Kitazawa, 1980) was employed to compute angular distribution coefficients, fore-aft asymmetries and cross sections. This program evaluates transition matrix elements of the form

$\langle f|H_{int}|i\rangle$, and then calculates observables from the matrix elements according to the angular distribution theory of particle-capture reactions (see §4.5). The two-body form of the interaction Hamiltonian was discussed in the previous section. A description of the wave functions employed in the calculations is presented next.

Gibson and Lehman (1984) have generated three-body bound state wave functions from a phenomenological nucleon-nucleon potential via the Faddeev formalism. Various sets of nucleon-nucleon potential parameters were employed, hence numerous wave functions were generated. These wave functions satisfy the symmetry requirements of the three-nucleon system (see §1.2) and are consistent with experimentally determined properties of ^{3}H and ^{3}He. Although the wave functions were generated for the ^{3}H nucleus, they may also be used to represent the ^{3}He nucleus. This is because the Coulomb interaction does not significantly alter the nuclear bound state wave function (Friar, 1982). The observables calculated for the nucleon-on-deuteron capture reactions should not depend on the presence or absence of the Coulomb force in the bound three-nucleon system (Lehman, 1984). Consequently, both the ^{2}H(n,γ)^{3}H and ^{2}H(p,γ)^{3}He calculations of this work employed the same final state wave functions.

In a two-body direct capture calculation, the final state single-particle wave function represents a nuclear system in which the captured particle orbits a point-like nuclear core. A two-body (neutron plus deuteron) wave function may be projected out of the three-body ^{3}H wave function by integrating over the proper internal coordinates. Lehman has performed the overlap integrals necessary to extract the n+d

wave function. Three such wave functions, corresponding to deuteron D-state probabilities of $P_D(d) = 0\%$, 4% and 7%, were made available to us. The probabilities of the partial states which make up the ^3H and projected n+d wave function, as a function of the above deuteron D-state probabilities are presented in Table 5-1. It is evident from this table that the two-body wave functions are, in general, made up of a dominant S-state part with a small admixture of D-state.

The S-state and D-state radial components, $u_S(\rho)$ and $u_D(\rho)$ respectively, of the two body wave functions are displayed in Figure 5-2. The functions $u_i(\rho)$ are related to radial wave functions according to $u_i(\rho)/\rho = \psi_i(\rho)$ and have normalization

$$\sum_i \int u_i^2(\rho)\, d\rho = 1, \qquad 5\text{-}21$$

where ρ is the distance between the point-neutron and point-deuteron of the two-body system. The $u_S(\rho)$ functions differ among each other in their peak region (1 to 2 fm) and in part of the tail region (3 to 12 fm). The $u_D(\rho)$ functions are more similar and differ only in the vicinity of their peaks (at 2 fm). The D-state wave function corresponding to $P_D(d) = 0$ is identically zero.

In the direct capture model the single-particle final state has a specific orbital angular momentum. Since the electric operator (i.e. the form employed in these calculations) is spin-independent, transitions to final states of different orbital angular momenta do not interfere (Weller, 1980). Consequently, each two-body calculation was performed in two parts, once employing an S-state wave function and

Table 5-1. Calculated admixture probabilities of states in various wave functions as a function of the D-state probability of the deuteron. Listed are the S-state, S'-state and D-state probabilities of three-body ^3H wave functions, and the S-state and D-state probabilities of projected two-body (neutron plus deuteron) wave functions. The latter probabilities are presented as a percentage of the total three-body wave functions and also as a percentage of the projected two-body wave functions (normalized in the latter case according to $P_S + P_D = 1$). The individual i-state probability, P_i, is defined in Equation 1-1.

$P_D(d)$ (%)	0	4	7
$P_S(^3H)$ (%)	98.26	93.16	89.08
$P_{S'}(^3H)$ (%)	1.74	1.74	1.74
$P_D(^3H)$ (%)	0.00	5.08	9.12
$P_S(n+d)$ (%)	43.0	43.1	43.2
$P_D(n+d)$ (%)	0.0	0.51	0.65
$P_S(n+d)$ (norm. %)	100.0	98.8	98.5
$P_D(n+d)$ (norm. %)	0.0	1.2	1.5

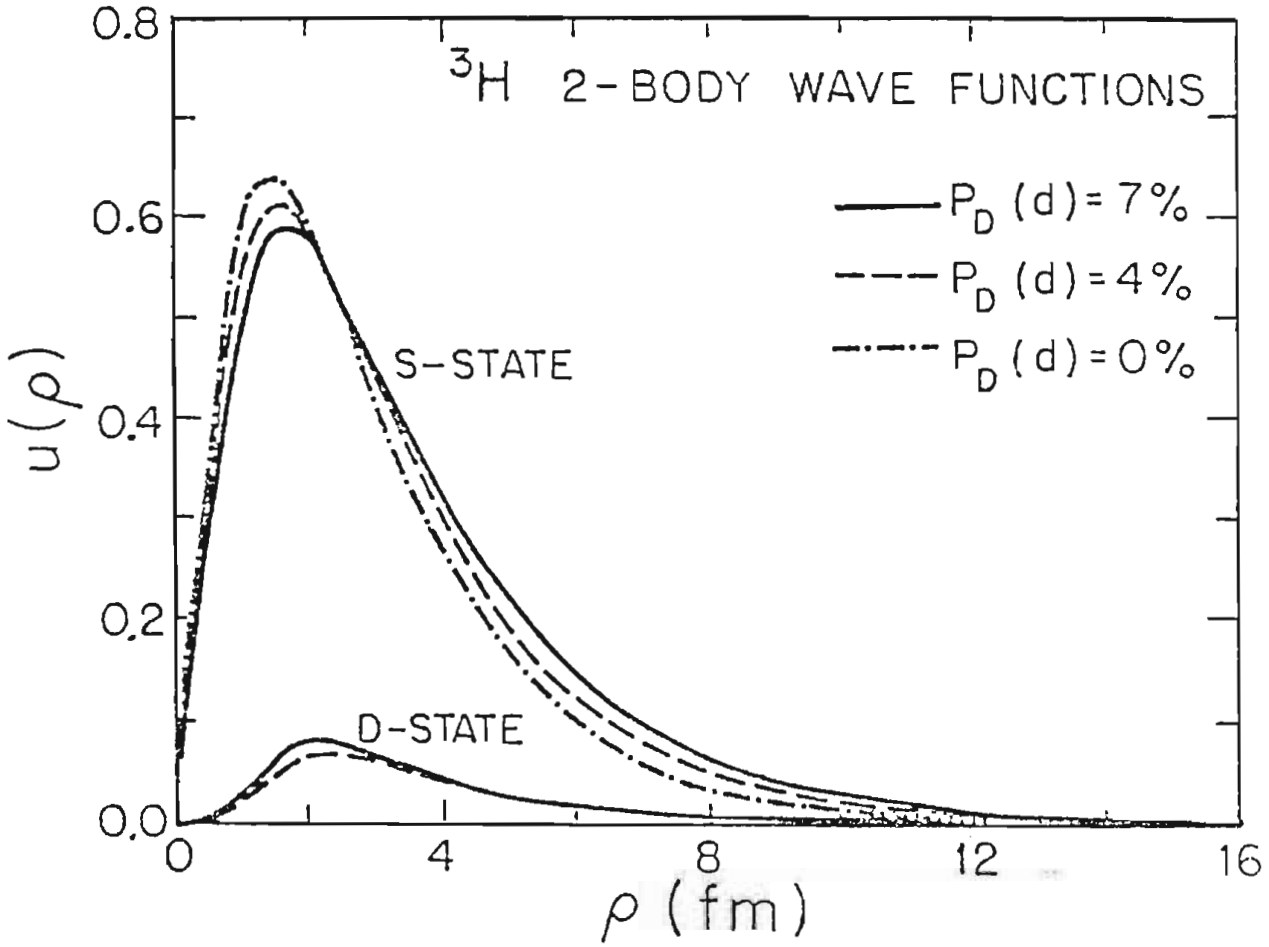

Figure 5-2. Bound state radial wave functions. These wave functions are two-body (neutron plus deuteron) projections of three-body wave functions derived from the Faddeev formalism. The S-state and D-state components of the wave functions are displayed for 0%, 4% and 7% deuteron D-state probabilities.

secondly employing the corresponding D-state wave function. The resulting cross sections were simply added together while angular distribution coefficients (a_k's and b_k's) were weighted by A_0's according to

$$5\text{-}22 \qquad a_k(S+D) = \frac{a_k(S)\ A_0(S) + a_k(D)\ A_0(D)}{A_0(S) + A_0(D)}.$$

Consider now the continuum initial state wave function. The program HIKARI generates the initial state wave function from an optical model potential by solving the Schrödinger equation. The optical model potential is made up of a central term, an absorption term and a spin-orbit term. It has the form

$$5\text{-}23 \qquad V(\rho) = -V_o\ f(r_o,a_o,\rho) + i\ 4\ a_d\ W_d\ \frac{d}{d\rho}\ f(r_d,a_d,\rho)$$
$$+ \left(\frac{h}{m_\pi c}\right)^2 V_{so}\ \frac{1}{\rho}\ \frac{d}{d\rho}\ f(r_o,a_o,\rho)\ \vec{l}\cdot\vec{s},$$

where f is the Woods-Saxon form factor

$$5\text{-}24 \qquad f(r,a,\rho) = \frac{1}{1 + \exp\left(\frac{r\ A^{1/3} - \rho}{a}\right)},$$

and the various V's, r's and a's are parameters. Two sets of optical model parameters were employed to generate initial state wave functions (see Table 5-2). DeVries et al. (1972) measured unpolarized $^2H(p,p)^2H$ elastic scattering angular distributions at E_p = 35 and 46.3 MeV. They determined the parameters of the central and absorptive terms of the optical model potential from fits to the data. The energy dependence of the potential was derived from the data. Guss (1982) measured a

Table 5-2. Optical model potential parameters. These two sets of parameters were employed to generate continuum initial state wave functions for two-body direct capture calculations.

Parameter	DeVries *et al.* (1972)	Guss (1982)
V_o (MeV)	76.9 - 0.55 E_n	90.75 - 0.4871 E_n
r_o (fm)	1.00	1.153
a_o (fm)	0.402	0.454
V_d (MeV)	2.49 - 0.03 E_n	4.54 + 0.1 E_n (E_n<10)
		6.54 - 0.1 E_n (E_n>10)
r_d (fm)	1.9	1.104
a_d (fm)	0.9612	0.691
V_{so} (MeV)		2.408 - 0.0331 E_n
r_{so} (fm)		1.049
a_{so} (fm)		1.119

polarized $^2H(\vec{n},n)^2H$ elastic scattering angular distribution at E_n = 14 MeV. Parameters for all three terms of the optical model potential were determined from fits to the polarized data. The energy dependence of the Guss potential is based on global parameters for light ion scattering.

The results of the two-body calculations, which employed three different final state wave functions and two different initial state wave functions, shall now be compared with measured angular distribution coefficients, fore-aft asymmetries and cross sections. The $^2H(n,\gamma)^3H$ a_k and b_k data, determined from fits to angular distributions of cross sections and analyzing powers at E_n = 9.0 and 10.8 MeV (see Table 4-2), are displayed in Figure 5-3. Recall that the data are not precise enough to determine a significant b_4 coefficient (§4.2). The theoretical curves were calculated with an initial state wave function generated from the DeVries potential and with final state wave functions corresponding to $P_D(d)$ = 0% (dot-dashed curves), 4% (dashed curves) and 7% (solid curves). In the a_2 calculation the $P_D(d)$ = 4% and 7% curves overlap and are indistinguishable, whereas the $P_D(d)$ = 0% curve is essentially equal to −1 over the entire energy range shown. In the a_4, b_1, b_2, and b_3 calculations all three curves overlap. The calculations of the b_k coefficients are identically zero because the DeVries potential has no spin-orbit term. The fact that the b_k data are in good agreement with zero implies that spin-orbit coupling in the $^2H(n,\gamma)^3H$ reaction is weak. This justifies the approach taken in the transition matrix analysis of the data which combined matrix elements of equal l

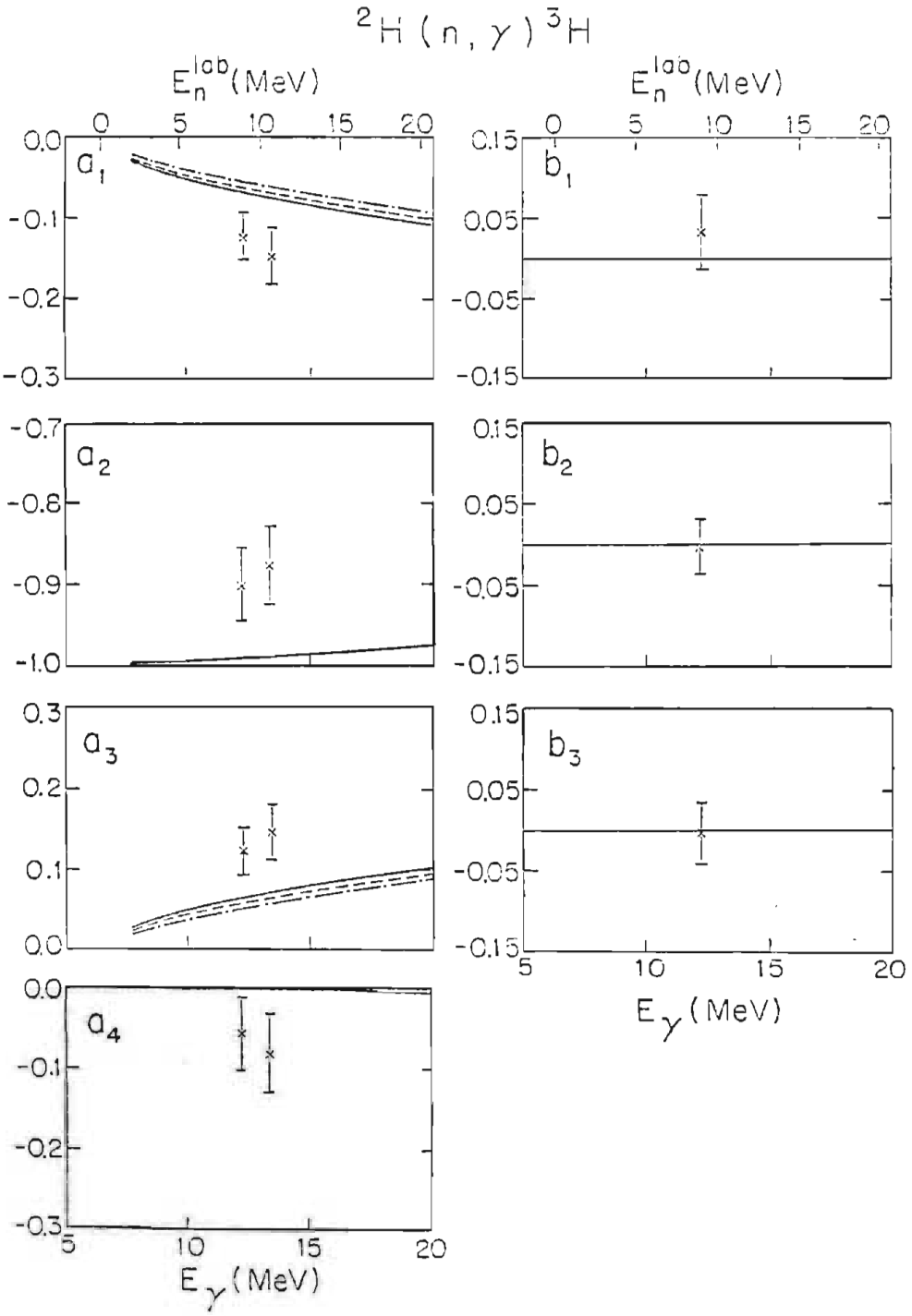

Figure 5-3. $^2H(n,\gamma)^3H$ angular distribution coefficients (see Table 4-2). The error bars represent statistical uncertainties. The curves are two-body direct capture calculations employing the DeVries potential and the bound state wave functions of Figure 5-2.

but different j (§4.5). In the case of the a_k coefficients there is clearly disagreement between the data and theory. The same data, but with calculations resulting from employment of the Guss potential, are displayed in Figure 5-4. Here too all three theoretical curves overlap in the a_4, b_1 and b_3 calculations. Due to the presence of a spin-orbit term in the Guss potential, the b_2 curves are nonzero. As with the calculations which employed the DeVries potential, there is disagreement between theory and experiment in the a_k coefficients, but agreement in the case of the b_k's.

What do the significant discrepancies between experimental and theoretical a_k coefficients indicate about the physics of the $^2H(n,\gamma)^3H$ reaction? If the $^2H(n,\gamma)^3H$ reaction is dominated by E1 and E2 transitions, it follows from Equations 4-19 that a_1 and a_3 are due to (E1)(E2) interference, a_2 is related to $(E2)^2$ and $(E1)^2$, and a_4 is proportional to $(E2)^2$. From Figures 5-3 and 5-4 it is evident that the data are consistent with an E2 strength which is enhanced relative to the theoretical predictions: More E2 strength implies (1) a more negative a_1 coefficient; (2) a less negative a_2 coefficient; and (3) greater a_3 and a_4 coefficients.

Consider now another observable which describes the shape of the angular distribution of cross sections. Displayed in Figure 5-5 and Figure 5-6 are fore-aft asymmetry data and theoretical curves corresponding to calculations with the DeVries and Guss potentials respectively. Shown are not only the data of this work, but also other photonuclear data involving the ^3H and ^3He nuclei. The two-body direct

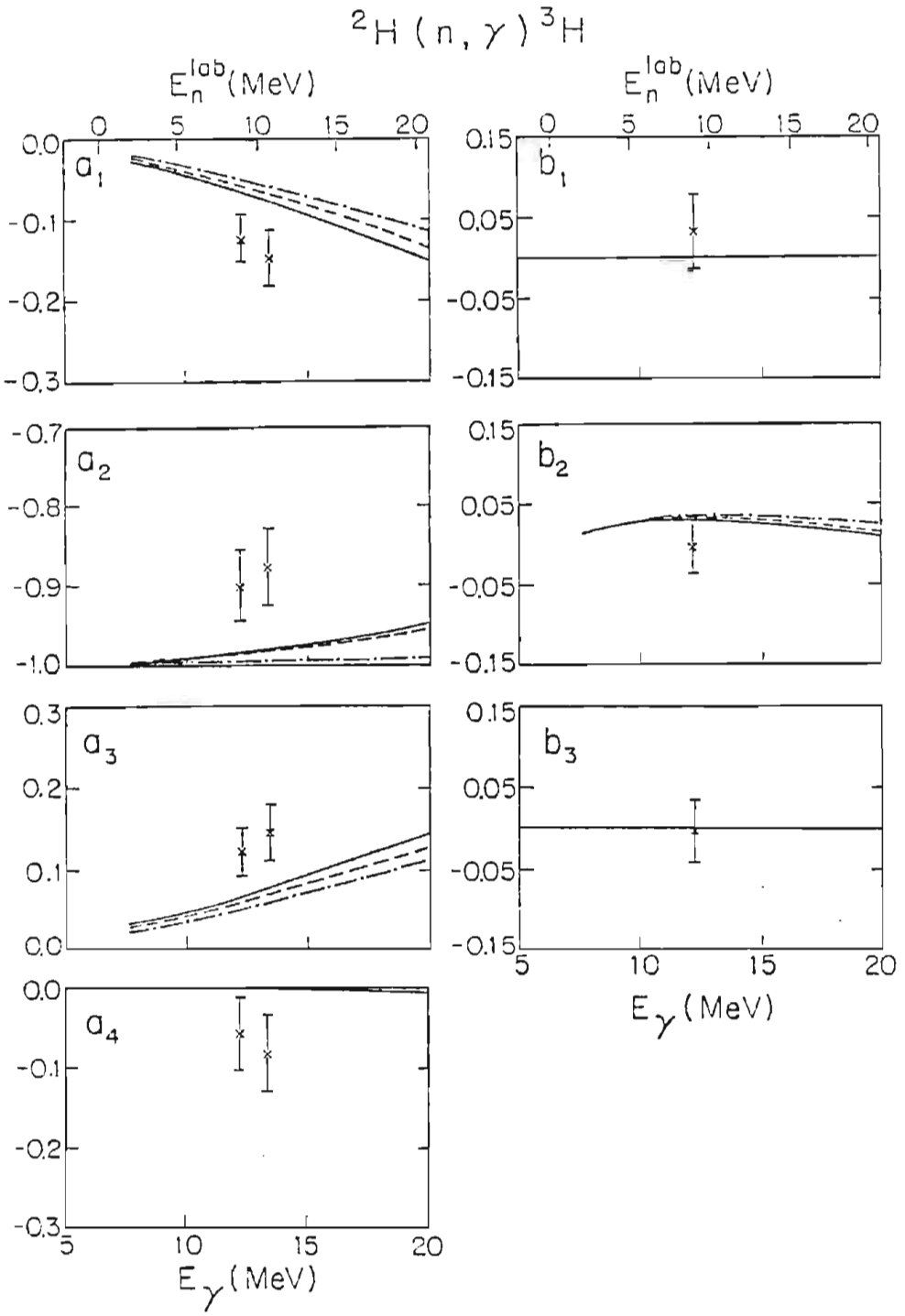

Figure 5-4. Same as Figure 5-3 except that the Guss potential was employed in the calculation to generate the continuum state wave function.

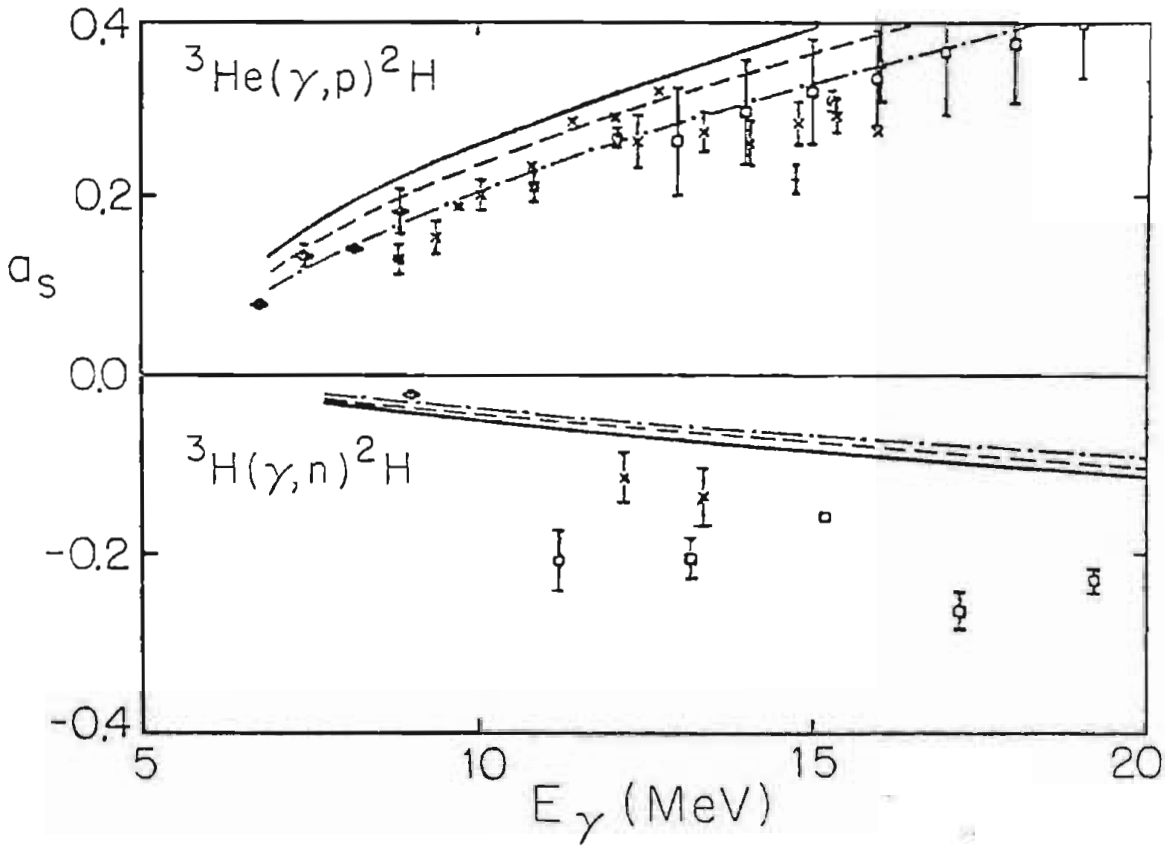

Figure 5-5. Fore-aft asymmetry data of Figure 4-4. The curves are two-body direct capture calculations employing the DeVries potential and the bound state wave functions of Figure 5-2.

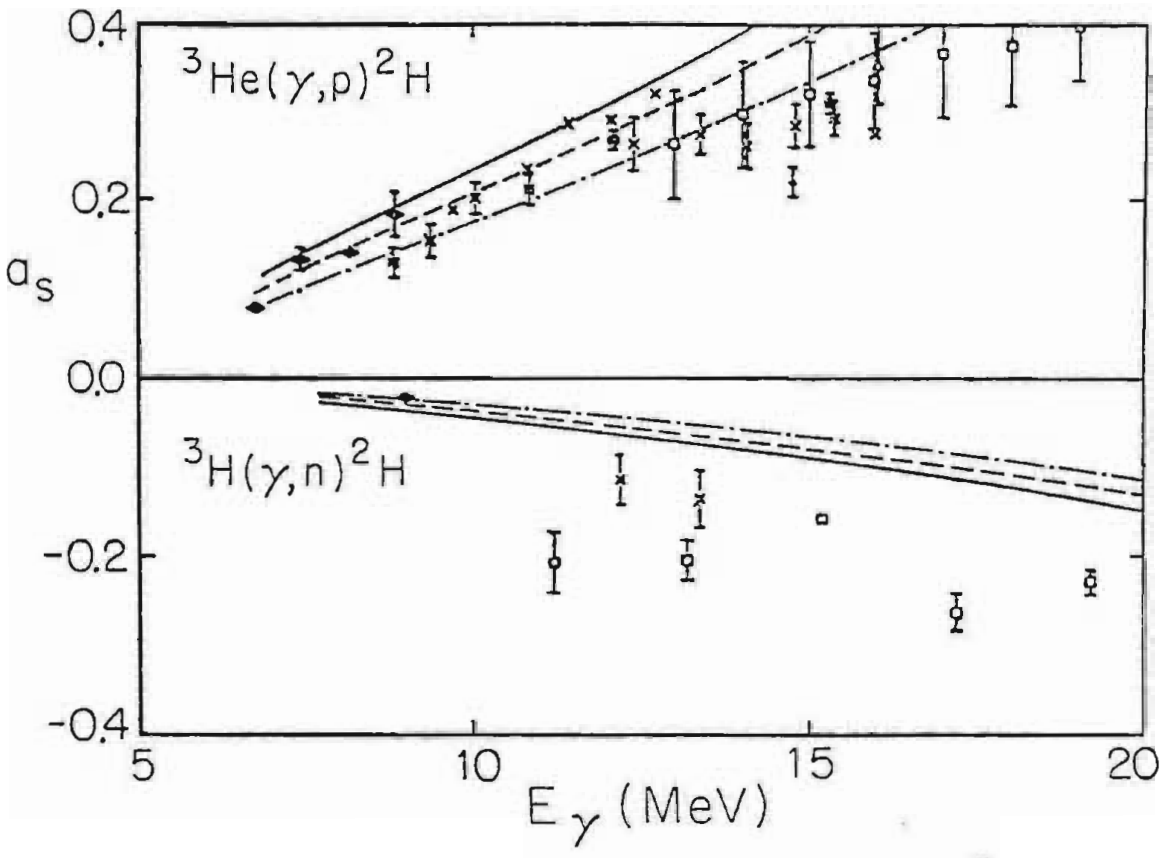

Figure 5-6. Same as Figure 5-5 except that the Guss potential was employed in the calculation to generate the continuum state wave function.

capture calculations agree well with ^{3}He measurements but are inconsistent with the $^{2}H(n,\gamma)^{3}H$ data of this work (X's) and the $^{3}H(e,e'd)n$ data of Skopik et al. (1981) (open squares). Recall that the expression for the asymmetry in terms of Legendre expansion coefficients is

$$5\text{-}25 \qquad a_s = \frac{a_1 - \frac{2}{3} a_3}{\sqrt{3}\ (1 - \frac{7}{18} a_4)}.$$

It follows from Equations 4-19 that

$$5\text{-}26 \qquad a_s \propto \frac{(E1)(E2)\cos(\phi_{E2}-\phi_{E1})}{(E1)^2 + (E2)^2} \simeq \frac{(E1)(E2)\cos(\phi_{E2}-\phi_{E1})}{(E1)^2}.$$

Since a_s is directly proportional to the E2 amplitude, the previous conclusion that the data are consistent with an E2 strength which is enhanced relative to theoretical predictions is acceptable here too.

The ^{3}H theoretical asymmetries are less in magnitude than the ^{3}He theoretical asymmetries directly as a consequence of neutron versus proton quadrupole effective charges. Recall that the form of the two-body electromagnetic operator is

$$5\text{-}27 \qquad -\frac{1}{3} \vec{\varepsilon}\cdot\vec{\rho} + \frac{i}{2}\left[\frac{1}{9} \vec{\varepsilon}\cdot\vec{\rho}\ \vec{k}\cdot\vec{\rho}\right]$$

in the case of ^{3}H, and

$$5\text{-}28 \qquad \frac{1}{3} \vec{\varepsilon}\cdot\vec{\rho} + \frac{i}{2}\left[\frac{5}{9} \vec{\varepsilon}\cdot\vec{\rho}\ \vec{k}\cdot\vec{\rho}\right]$$

in the case of ^{3}He. The factors -1/3 and 1/9 are the neutron dipole and quadrupole effective charges respectively. Similarly, 1/3 and 5/9 are the proton dipole and quadrupole effective charges respectively. On the

basis of Equations 5-26 through 5-28 one would expect the theory to predict a $^{2}H(n,\gamma)^{3}H$ to $^{2}H(p,\gamma)^{3}He$ asymmetry ratio of approximately

$$5\text{-}29 \qquad \frac{a_s(\gamma,n)}{a_s(\gamma,p)} \simeq \frac{(-1/3)(1/9)/(-1/3)^2}{(1/3)(5/9)/(1/3)^2} = -1/5.$$

In fact one sees from Figure 5-7, where the asymmetry ratios are plotted as $^{3}H(\gamma,n)^{2}H$ over $^{3}He(\gamma,p)^{2}H$, that the prediction is exactly -0.2 everywhere except at low energies near reaction thresholds (6.3 MeV for $^{3}H(\gamma,n)^{2}H$ versus 5.5 MeV for $^{3}He(\gamma,p)^{2}H$). The deviation from -0.2 at low energies is due to Coulomb and angular momentum barrier effects. The theoretical asymmetry ratio is insensitive to the choice of optical model potential or to the amount of deuteron D-state probability (0%, 4% or 7%) associated with the bound state wave function, as long as they are the same in both the $^{2}H(n,\gamma)^{3}H$ and $^{2}H(p,\gamma)^{3}He$ calculations.

The ratios of experimental asymmetries tend to lie on the line $a_s = -0.5$. Perhaps the discrepancy between theory and data arises from the assumption that one may treat the target nucleus as a point. A three-body direct capture calculation, which includes the internal coordinates of the deuteron, has been performed. That calculation is described in the next section.

The final comparisons of two-body theory with experiment are concerned with cross sections. Existing total cross sections, from photonuclear reactions involving the ^{3}H nucleus, are displayed in Figure 5-8. The capture data of this work (four X's) have been converted to photodisintegration cross sections via detailed balance. Theoretical calculations which employed the DeVries potential are

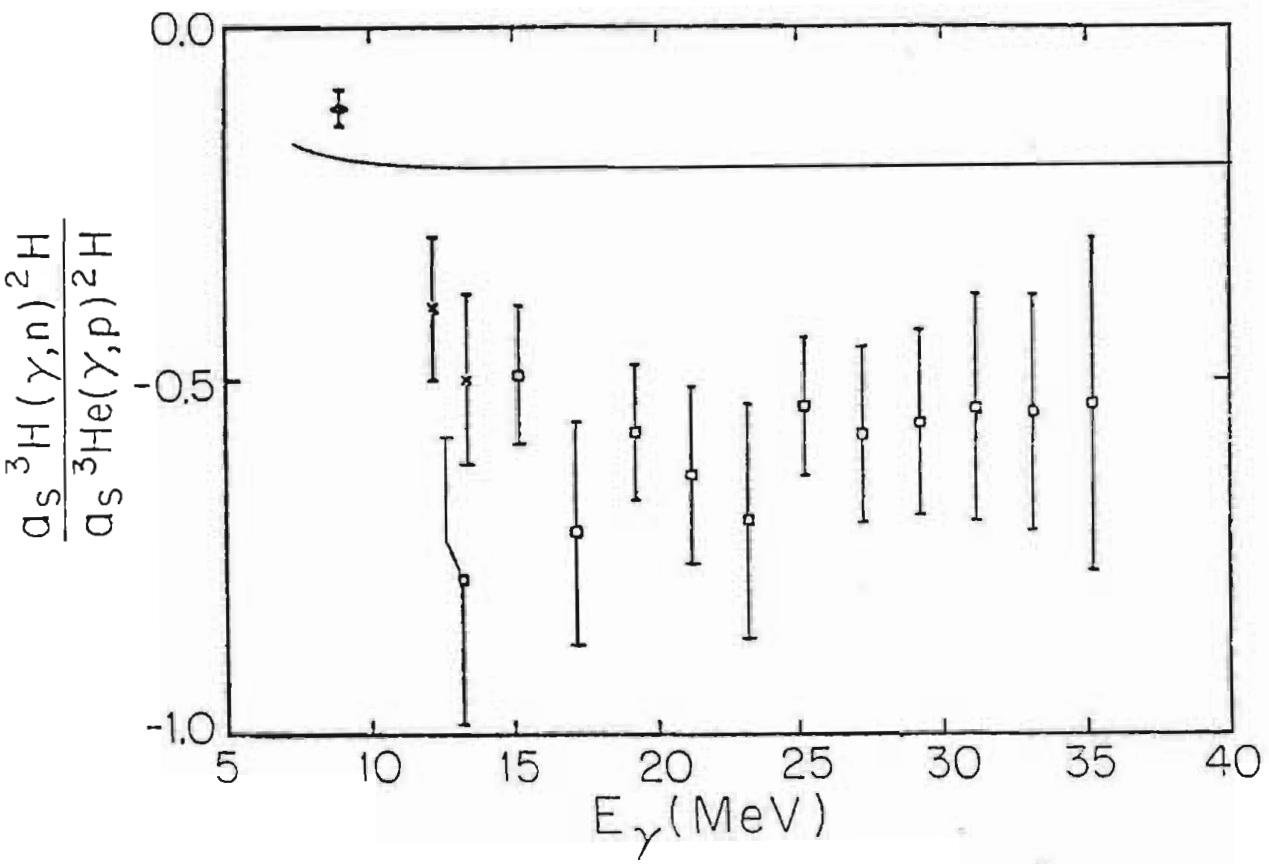

Figure 5-7. $^3H(\gamma,n)^2H$ to $^3He(\gamma,p)^2H$ fore-aft asymmetry ratios of Figure 4-5. The curve is the result of a two-body direct capture calculation. The theoretical prediction is insensitive to which bound state wave function (see Figure 5-2) or optical model potential (see Table 5-2) was employed, provided the same ones were used in both the $^3H(\gamma,n)^2H$ and $^3He(\gamma,p)^2H$ calculations.

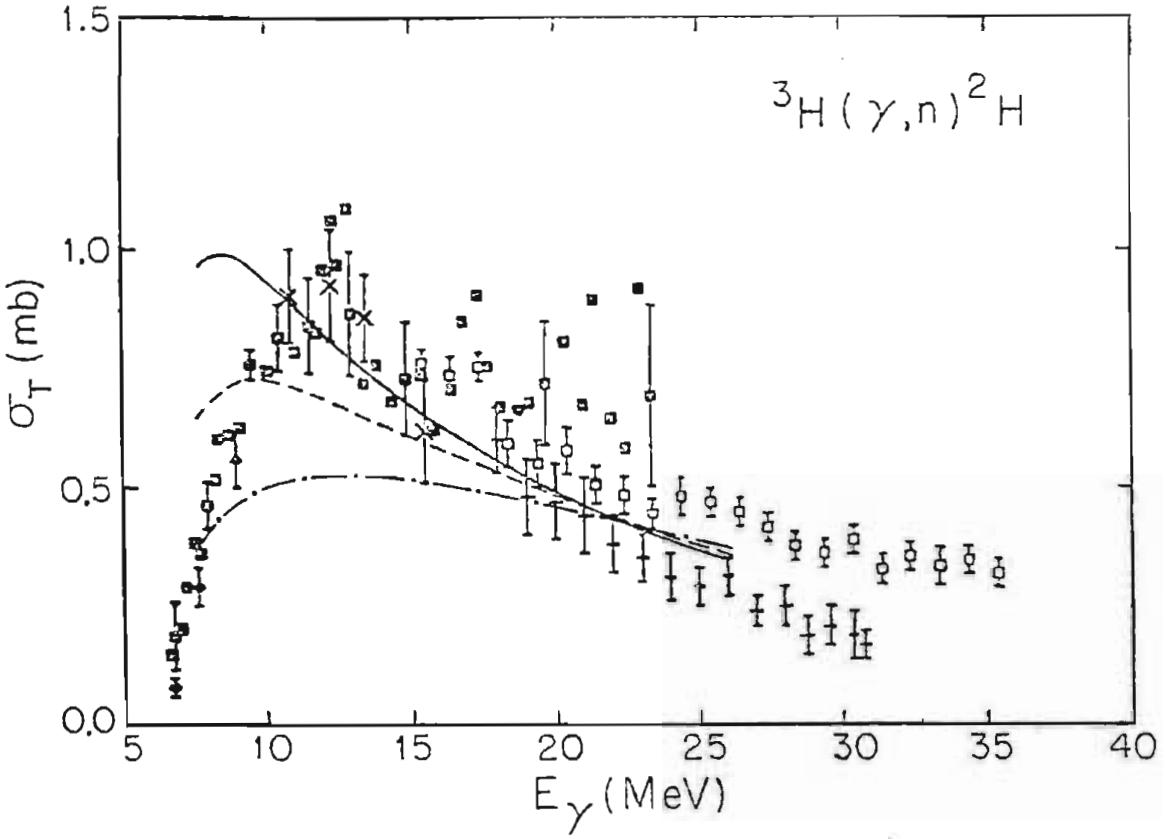

Figure 5-8. Total cross sections of Figure 4-7. The curves are two-body direct capture calculations employing the DeVries potential and the bound state wave functions of Figure 5-2.

shown. The spectroscopic factor for neutron capture to a single-particle final state in ^{3}H is 3 (Lehman 1984) and was included in the calculations. Furthermore, this factor was weighted by the percentage of the total ^{3}H wave function present in the projected n+d wave function (see Table 5-1). The magnitudes of the curves are very sensitive to the final state wave function and to model parameters of the theory. Because of this sensitivity, agreement with the data may be fortuitous. The same data, but with theoretical curves arising from calculations which employed the Guss potential, are displayed in Figure 5-9. These curves peak higher, and fall off more rapidly with energy, than do those associated with the DeVries potential. Thus the theoretical calculations are also very sensitive to the initial state wave function.

One can avoid the uncertainties involved with theoretical calculations of absolute cross sections if one compares ratios of cross sections. Ratios of 90^{o} differential cross sections, derived from capture measurements at TUNL (X's), and ratios published by Skopik et al.(1981), are displayed in Figure 5-10. The TUNL data were converted to photodisintegration values via detailed balance. The two-body direct capture calculation is insensitive to the choice of optical model potential or to the amount of deuteron D-state probability (0%, 4% or 7%) associated with the bound state wave function. Agreement between theory and data is very good. The data display the expected structure in the low energy region and are consistent with the value 1.0 in the 20 to 35 MeV region.

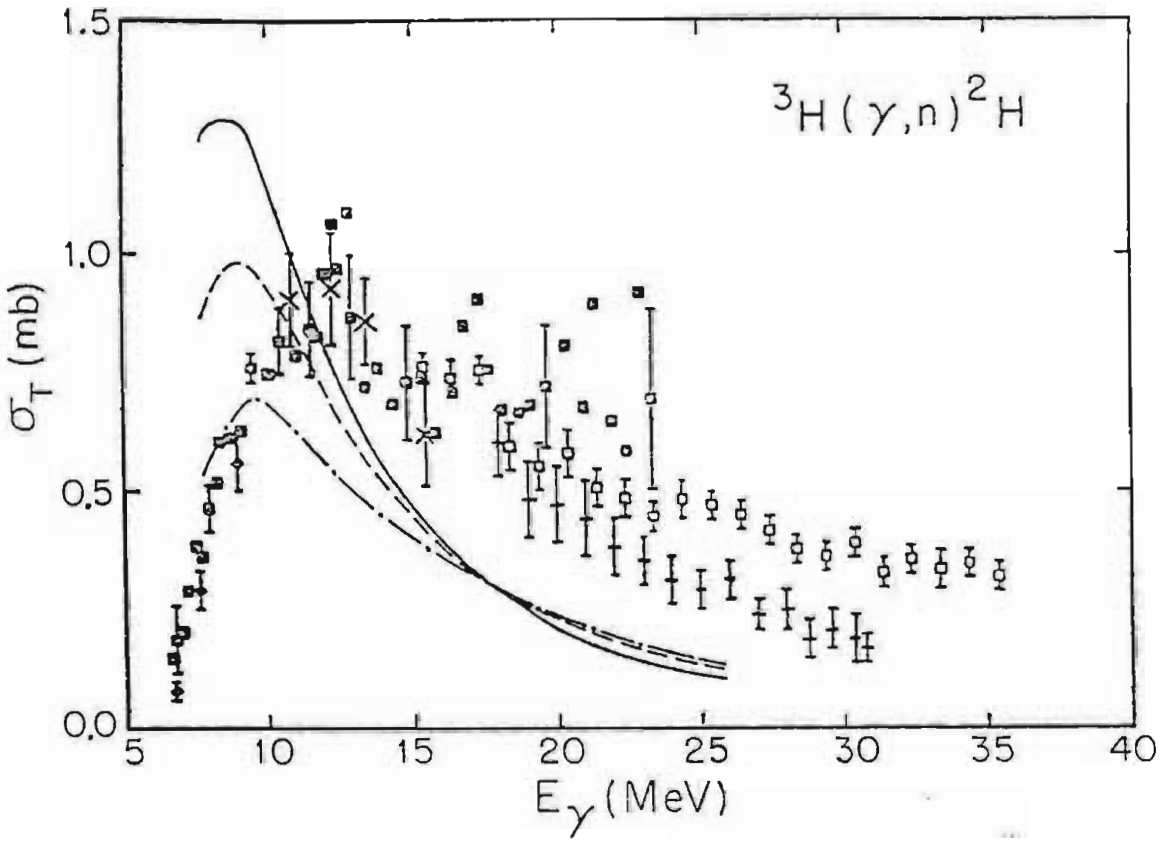

Figure 5-9. Same as Figure 5-8 except that the Guss potential was employed in the calculation to generate the continuum state wave function.

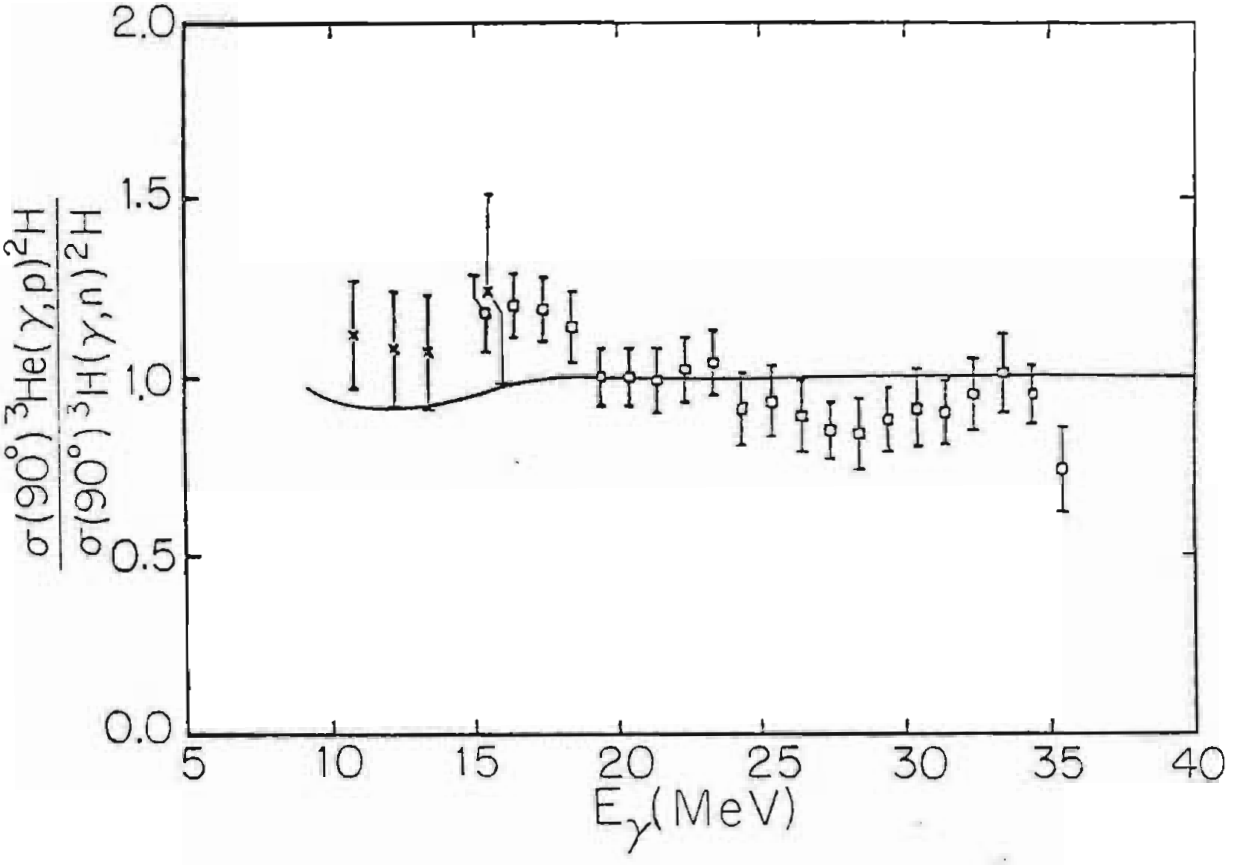

Figure 5-10. $^3He(\gamma,p)^2H$ to $^3H(\gamma,n)^2H$ cross section ratios of Figure 4-8. The curve is the result of a two-body direct capture calculation. The theoretical prediction is insensitive to which bound state wave function (see Figure 5-2) or optical model potential (see Table 5-2) was employed, provided the same ones were used in both the $^3H(\gamma,n)^2H$ an $^3He(\gamma,p)^2H$ calculations.

5.4 Three-Body Calculation of the Fore-Aft Asymmetry Ratio

Full three-body direct capture calculations, with three-body wave functions representing both the bound state and the continuum nucleon plus deuteron state, are currently being developed (Lehman, 1984). Due to the complexity of these calculations, complete results may not be available in the near future. Lehman has suggested a simpler alternative for a three-body calculation which could, in principle, resolve the discrepancies between experimental measurements and two-body theory. Such a calculation has been performed for the specific case of the $^2H(n,\gamma)^3H$ to $^2H(p,\gamma)^3He$ asymmetry ratio.

A theoretical $^2H(n,\gamma)^3H$ to $^2H(p,\gamma)^3He$ asymmetry ratio of -0.5, instead of -0.2 (see Figure 5-7), could be obtained if the E2 strength from the $^2H(n,\gamma)^3H$ channel were enhanced relative to the E2 strength from the $^2H(p,\gamma)^3He$ channel. Recall that the three-body form of the electric operator is

5-30
$$\left(-\frac{1}{3}\,\vec{\varepsilon}\cdot\vec{\rho} - \frac{1}{2}\,\vec{\varepsilon}\cdot\vec{r}\right) + \frac{i}{2}\left[\frac{1}{9}\,\vec{\varepsilon}\cdot\vec{\rho}\;\vec{k}\cdot\vec{\rho} + \frac{1}{6}\,\vec{\varepsilon}\cdot\vec{\rho}\;\vec{k}\cdot\vec{r} + \frac{1}{6}\,\vec{\varepsilon}\cdot\vec{r}\;\vec{k}\cdot\vec{\rho} + \frac{1}{4}\,\vec{\varepsilon}\cdot\vec{r}\;\vec{k}\cdot\vec{r}\right]$$

in the case of ^3H, and

5-31
$$\left(\frac{1}{3}\,\vec{\varepsilon}\cdot\vec{\rho} + \frac{1}{2}\,\vec{\varepsilon}\cdot\vec{r}\right) + \frac{i}{2}\left[\frac{5}{9}\,\vec{\varepsilon}\cdot\vec{\rho}\;\vec{k}\cdot\vec{\rho} - \frac{1}{6}\,\vec{\varepsilon}\cdot\vec{\rho}\;\vec{k}\cdot\vec{r} - \frac{1}{6}\,\vec{\varepsilon}\cdot\vec{r}\;\vec{k}\cdot\vec{\rho} + \frac{1}{4}\,\vec{\varepsilon}\cdot\vec{r}\;\vec{k}\cdot\vec{r}\right]$$

in the case of ^{3}He. Compared with the two-body form of the operator (i.e. $\vec{r} = 0$), the quadrupole part has three additional terms. The significant feature to note is that all three terms have the same sign in the ^{3}H case, whereas in the ^{3}He case there is a mixture. A priori, one cannot predict whether a given term will contribute positively or negatively to the matrix element because of the dot products involved. However, because the additional terms enter differently into the operators depending on the nucleus involved, the possibility exists that a three-body calculation could produce the experimental asymmetry ratio.

It has been demonstrated that, at the energies of this experiment, the fore-aft asymmetry in angular distributions of $^2H(n,\gamma)^3H$ and $^2H(p,\gamma)^3He$ cross sections is an interference effect between E1 and E2 transition matrix elements (see Equation 5-26). The E1 and E2 transitions couple initial and final states which are predominantly S-state with a small admixture of D-state. A three-body calculation, which computes the $^2H(n,\gamma)^3H$ to $^2H(p,\gamma)^3He$ asymmetry ratio resulting from the interference of S-state to S-state matrix elements ($R^{E1}(S\rightarrow S) \times R^{E2}(S\rightarrow S)$), has been performed. The interference terms which one would expect to be the next largest, and which one would want to include in the calculation, are those which are first order in D-state. However, Van Hees (1984) has proved that all such terms, $R^{E1}(S\rightarrow S) \times R^{E2}(S\rightarrow D)$, $R^{E1}(S\rightarrow D) \times R^{E2}(S\rightarrow S)$, $R^{E1}(S\rightarrow S) \times R^{E2}(D\rightarrow S)$ and $R^{E1}(D\rightarrow S) \times R^{E2}(S\rightarrow S)$, are identically zero due to angular momentum restrictions. Terms which are second order, or higher, in D-state are expected to be small in comparison with the ones involving only S-states and have been

neglected. The reasons why the interference terms which are first order in D-state are zero shall be discussed next, followed by a description of the calculation involving $R^{E1}(S\rightarrow S)$ and $R^{E2}(S\rightarrow S)$ matrix elements.

Let α, β, γ, and μ be the spin projections of the incident nucleon, target deuteron, three-nucleon system and emitted photon respectively. The spin coupling involved with $R(S\rightarrow S)$ matrix elements, for both E1 and E2 transitions, gives rise to a Clebsch-Gordan coefficient such that

$$5\text{-}32 \qquad R(S\rightarrow S) \propto (\tfrac{1}{2}\ \alpha\ 1\ \beta\ |\ \tfrac{1}{2}\ \gamma).$$

When the bound three-nucleon system is in a D-state, one finds that for both E1 and E2 transitions

$$5\text{-}33 \qquad R(S\rightarrow D) \propto (\tfrac{1}{2}\ \alpha\ 1\ \beta\ |\ \tfrac{3}{2}\ \gamma).$$

Thus the (E1)(E2) interference of $R(S\rightarrow S)$ and $R(S\rightarrow D)$ matrix elements leads to either

$$5\text{-}34 \qquad \sum_{\alpha\beta}\left[R^{E1}(S\rightarrow S)\ \times\ R^{E2}(S\rightarrow D)\right] \propto \sum_{\alpha\beta}\ (\tfrac{1}{2}\ \alpha\ 1\ \beta\ |\ \tfrac{1}{2}\ \gamma)(\tfrac{1}{2}\ \alpha\ 1\ \beta\ |\ \tfrac{3}{2}\ \gamma)$$

or

$$5\text{-}35 \qquad \sum_{\alpha\beta}\left[R^{E1}(S\rightarrow D)\ \times\ R^{E2}(S\rightarrow S)\right] \propto \sum_{\alpha\beta}\ (\tfrac{1}{2}\ \alpha\ 1\ \beta\ |\ \tfrac{3}{2}\ \gamma)(\tfrac{1}{2}\ \alpha\ 1\ \beta\ |\ \tfrac{1}{2}\ \gamma).$$

These interference terms are zero because of the Clebsch-Gordan orthogonality relation $\sum_{\alpha\beta}\ (j_\alpha\ \alpha\ j_\beta\ \beta\ |\ j\ \gamma)(j_\alpha\ \alpha\ j_\beta\ \beta\ |\ j'\ \gamma) = \delta_{jj'}$, (Rose, 1957).

In the case of an E2 transition from an initial state in which the

deuteron is in a D-state, the spin coupling yields

5-36 $$R^{E2}(D\rightarrow S) \propto (\tfrac{1}{2}\ \alpha\ 1\ \beta-\mu\ |\ \tfrac{1}{2}\ \gamma).$$

Consequently,

5-37 $$R^{E1}(S\rightarrow S) \times R^{E2}(D\rightarrow S) \propto (\tfrac{1}{2}\ \alpha\ 1\ \beta\ |\ \tfrac{1}{2}\ \gamma)\ (\tfrac{1}{2}\ \alpha\ 1\ \beta-\mu\ |\ \tfrac{1}{2}\ \gamma).$$

These two Clebsch-Gordan coefficients cannot simultaneously be nonzero because one requires that $\alpha + \beta = \gamma$, and the other requires that $\alpha + \beta - \mu = \gamma$, where $\mu = \pm 1$. Hence interference terms of this type are zero.

Finally, $R^{E1}(D\rightarrow S) \times R^{E2}(S\rightarrow S)$ is zero because the matrix element $R^{E1}(D\rightarrow S)$ is zero. The bound three-nucleon S-state consists predominantly of S-wave parts (i.e. the relative orbital angular momentum between any two nucleons is zero) (see §1.2). A D-state deuteron in the initial state cannot make an E1 transition, due to selection rules, to such a final state. Thus $R^{E1}(D\rightarrow S) = 0$.

The fact that the above interference terms are zero is consistent with previously discussed two-body calculations. In the channel spin representation of the two-body capture reaction (see §4.5), $R^{E1}(S\rightarrow S) \times R^{E2}(S\rightarrow D)$ and $R^{E1}(S\rightarrow D) \times R^{E2}(S\rightarrow S)$ correspond to the interference of matrix elements with different channel spins. Since channel spin mixing cannot be present in any cross section observables, as is evident from the expressions for a_1 and a_3 in Equations 4-19, such terms do not contribute to the asymmetry in the two-body calculation.

The calculation of the $^2H(n,\gamma)^3H$ to $^2H(p,\gamma)^3He$ asymmetry ratio,

from matrix elements involving only S-states, employed the S-state part of the three-body wave function of Riska (1980) for the bound state, and a plane wave times the deuteron wave function of Hulthén (1957) for the continuum state. These wave functions were selected for the calculation because of their simple analytic forms and because they contain the essential features necessary for a calculation of the fore-aft asymmetry ratio (Lehman, 1984).

Riska's bound state wave function has the form

$$5\text{-}38 \qquad \Psi = \phi \, \Phi = \prod_{i<j} \left[1 - \exp(-\alpha^2 r_{ij}^2)\right]^{1/2} \exp(-\tfrac{1}{2}\beta(\sum_{i<j} r_{ij}^2)^{1/2}) \, \Phi,$$

where Φ is a totally antisymmetric spin-isospin function, $r_{ij} = |\vec{r}_i - \vec{r}_j|$ is the relative distance between two nucleons, and α and β are parameters. The correlation factor $\left[1 - \exp(-\alpha^2 r_{ij}^2)\right]^{1/2}$ determines the shape of the wave function as $r_{ij} \to 0$, whereas the factor $\exp(-\frac{1}{2}\beta(\sum_{i<j} r_{ij}^2)^{1/2})$ determines its asymptotic behavior at large distances. The values of the parameters α and β were chosen so that the correct ^{3}H and ^{3}He form factors and radii were obtained (Riska, 1980). They are $\alpha = 1.0$ (1.0) fm^{-1} and $\beta = 1.39$ (1.44) fm^{-1} for ^{3}H (^{3}He).

The deuteron wave function employed in the calculation was

$$5\text{-}39 \qquad \Psi_d = \phi_d \, \Phi_d = \frac{(e^{-\gamma r} - e^{-\delta r})}{r} \, \Phi_d,$$

where Φ_d is a totally antisymmetric spin-isospin function, r is the distance between the neutron and proton and the spatial function ϕ_d has the Hulthén form. The coefficients in the exponentials are

5-40 $$\gamma = \sqrt{m_n E_b},$$

where m_n is the nucleon mass and E_b is the deuteron binding energy, and

5-41 $$\delta \simeq \frac{1}{2r_o} \left(3 - \gamma r_o + (\gamma^2 r_o^2 - 10\gamma r_o + 9)^{1/2}\right) \simeq 5.98\ \gamma,$$

where $r_o = 1.75$ fm is the triplet effective range parameter.

The matrix elements involved in the calculation were proportional to spatial integrals of the form

5-42 $$\int \phi^*(\vec{\rho},\vec{r})\ H^e_{int}(\vec{\rho},\vec{r})\ \phi_d(\vec{\rho},\vec{r})\ e^{i\vec{k}_n\cdot\vec{\rho}}\ d\vec{\rho}\ d\vec{r},$$

where $\vec{k}_n$ represents the momentum of the incident nucleon. The three-body form of the electric operator and the coordinates $\vec{\rho}$ and $\vec{r}$ are defined by Equations 5-16 through 5-18 and Figure 5-1. These integrals are a function of only three independent variables and were actually expressed in terms of the magnitudes of $\vec{\rho}$ and $\vec{r}$, and the cosine of the angle between them. They were numerically evaluated using LaGuerre integration for the ρ and r coordinates and Gaussian integration for the angle variable (Colby, 1984).

The result of the three-body direct capture calculation is displayed in Figure 5-11. It is essentially the same as that of the two-body calculation. The extra terms, which are present in quadrupole part of the three-body electric operator, have not affected the $^2H(n,\gamma)^3H$ to $^2H(p,\gamma)^3He$ asymmetry ratio significantly.

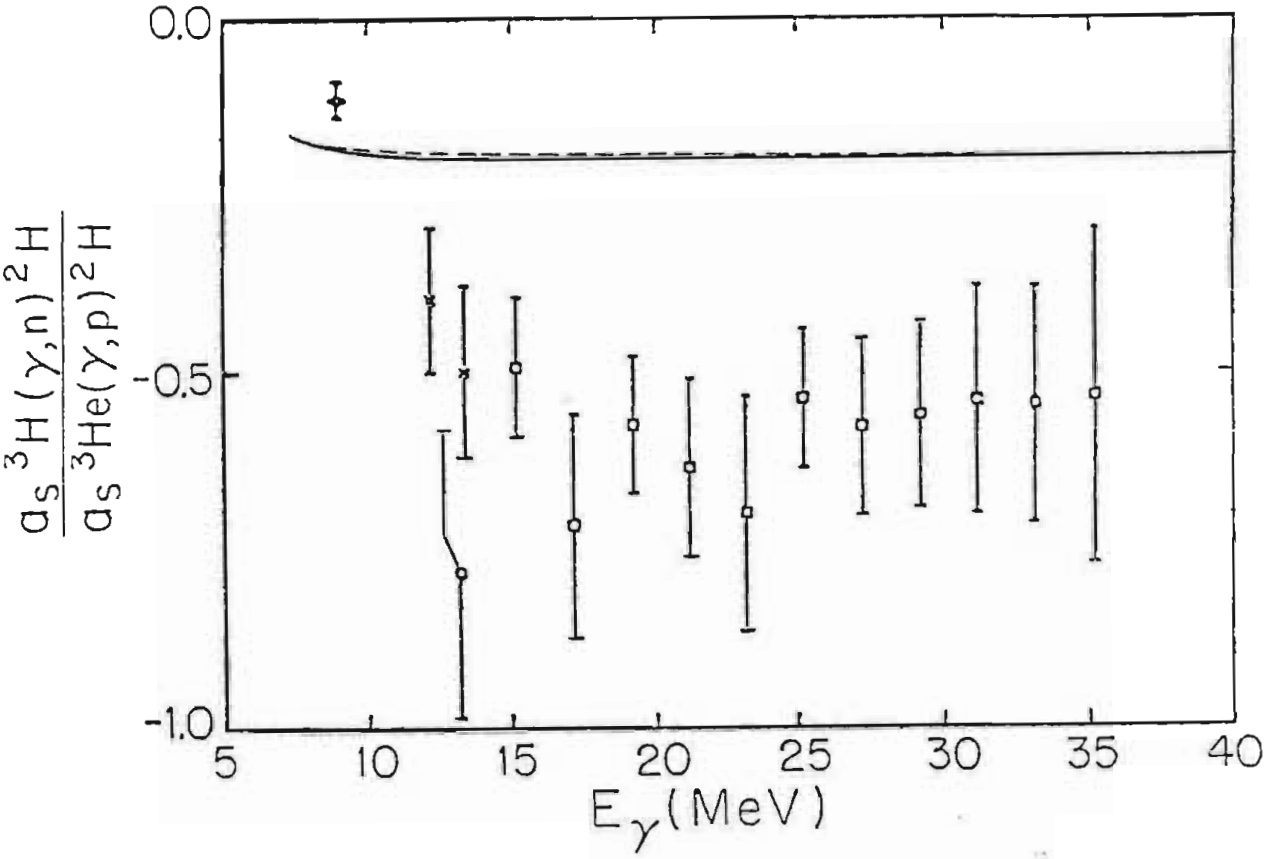

Figure 5-11. $^3H(\gamma,n)^2H$ to $^3He(\gamma,p)^2H$ fore-aft asymmetry ratios of Figure 4-5. The results of two-body (solid curve) and three-body (dashed curve) direct capture calculations are displayed.

6 SUMMARY AND CONCLUSIONS

Total cross sections of the $^{2}H(n,\gamma)^{3}H$ reaction have been determined at E_n = 6.85, 9.0, 10.8 and 14.0 MeV. They agree, after detail balancing, with photodisintegration data of Faul et al. (1980, 1981). Two-body direct capture calculations of $^{2}H(n,\gamma)^{3}H$ total cross sections are very sensitive to changes in the parameters which are employed to generate the initial and final state wave functions. Although one does obtain agreement with experiment for some sets of parameters, the agreement may be fortuitous.

Ninety degree differential cross sections of the $^{2}H(n,\gamma)^{3}H$ reaction have been determined, either by direct measurements or from fits to angular distributions, at the above energies. When compared with previous $^{2}H(p,\gamma)^{3}He$ measurements performed at TUNL (Skopik, 1979), the ratios of the cross sections are consistent with the value 1.0 predicted by conventional two-body capture calculations. This result is very significant in light of the fact that the experimental $^{3}H(p,\gamma)^{4}He$ to $^{3}He(n,\gamma)^{4}He$ 90° cross section ratio is as large as 1.7 at energies several MeV above reaction thresholds (Ward, 1981; Calarco, 1983). The three-body ratio provides a constraint which must be met by any theoretical model which can account for the anomalous ratio in the four-body system.

Fore-aft asymmetries have been determined from angular distributions of cross sections at E_n = 9.0 and 10.8 MeV. The values are surprisingly large in magnitude when compared with predictions of

two-body direct capture calculations. Electrodisintegration measurements of Skopik et al. (1981) have produced similarly large asymmetries. The discrepancy between the data and theory is consistent with an experimental E2 strength which is enhanced relative to the theory by a factor of approximately two. A three-body direct capture calculation, which includes the internal coordinates of the deuteron, was performed in an effort to account for the effect. The motivation behind this calculation was the fact that the three-body form of the electric operator contains extra quadrupole terms which are not present in the two-body form. It was hoped that the E2 strength observed in the $^{2}H(n,\gamma)^{3}H$ channel would result when these extra terms were included. However, the result of the calculation was essentially the same as the two-body prediction. Although all of the (E1)(E2) interference terms which can contribute to the asymmetry were not included in this calculation, the neglected terms all involved small E1 matrix elements arising from the presence of D-states. It is difficult to believe that such second-order terms could possibly account for the experimental result.

The data of this experiment establish the fact that asymmetries in $^{2}H(n,\gamma)^{3}H$ angular distributions of cross sections are inconsistent with conventional two-body capture calculations. A preliminary investigation of a complete three-body calculation, employing (realistic) analytical wave functions, strongly suggests that such a three-body calculation will not account for the observed effect. Lehman et al. (1984) are presently developing a full three-body calculation which employs wave

functions generated from a phenomenological nucleon-nucleon potential via the Faddeev formalism, and which includes a consistent treatment of the continuum. If, as implied by the present work, that calculation also fails to account for the experimental results, a fundamental problem exists. One must then consider what features of these calculations may be at fault. Maybe the wave functions, generated from non-local separable potentials, are inadequate. After all, the binding energy of ^{3}H is not accurately predicted by these same calculations. Perhaps a relativistic calculation which includes the effects of meson-exchange currents is needed. Another more exotic possibility would be the application of a three-body force. Clearly there are numerous possible explanations which could be investigated by theoretical physicists.

In any case, the carefully measured data of this work have established well-defined observables which contribute towards a better understanding of nuclear physics.

REFERENCES

R. D. Amado, M. P. Locher and M. Simonius

Phys. Rev. C17 (1978) 403

M. Anghinolfi, P. Corvisiero, M. Guarnone, G. Ricco and A. Zucchiatti

Nucl. Phys. A410 (1983) 173

I. M. Barbour and A. C. Phillips

Phys. Rev. Lett. 19 (1967) 1388

H. H. Barschall and W. Haeberli

"The Madison Convention," in Polarization Phenomena in Nuclear Reactions, Proceedings of the Third International Symposium, Madison 1970 (H. H. Barschall and W. Haeberli eds., University of Wisconsin Press, Madison, 1971)

D. H. Beck, J. Asai and D. M. Skopik

Phys. Rev. C25 (1982) 1152

B. D. Belt, C. R. Bingham, M. L. Halbert and A. van der Woude

Phys. Rev. Lett. 24 (1970) 1120

W. Bertl, W. Breunlich, A. Chalupka and S. Tagesen

Nucl. Instr. Meth. 104 (1972) 205

J. B. Birks

Proc. Phys. Soc. A64 (1951) 874

J. B. Birks

The Theory and Practice of Scintillation Counting (Pergamon Press, New York, 1964), p. 185

J. M. Blatt and V. F. Weisskopf

Theoretical Nuclear Physics (John Wiley and Sons, New York, 1952), pp. 193, 597, 784

F. Bloch, A. C. Graves, M. Packard and R. W. Spencer

Phys. Rev. 71 (1947) 373

R. Bösch, J. Lang, R. Müller and W. Wölfli

Phys. Lett. 8 (1964) 120

R. Bösch, J. Lang, R. Müller and W. Wölfli

Helv. Phys. Acta 48 (1965) 753

G. E. Brown

Nucl. Phys. 57 (1964) 339

R. Buck and A. A. Pilt

Nucl. Phys. A280 (1977) 133

J. R. Calarco, B. L. Berman and T. W. Donnelly

Phys. Rev. C27 (1983) 1866

H. Collard et al.

Phys. Rev. 138B (1965) 57

C. N. Chou

Phys. Rev. 87 (1952) 904

T. B. Clegg, G. A. Bissinger and T. A. Trainor

Nucl. Instr. Meth. 120 (1974) 445

P. C. Colby

Duke University, private communication (1984)

R. L. Craun and D. L. Smith

Nucl. Instr. Meth. 80 (1970) 239

S. DeBenedetti

Nuclear Interactions (John Wiley and Sons, New York, 1964), p. 290

L. M. Delves and A. C. Phillips

Rev. Mod. Phys. 41 (1969) 497

L. M. Delves, J. M. Blatt, C. Pask and B. Davies

Phys. Lett. 28B (1969) 472

G. Derrick and J. M. Blatt

Nucl. Phys. 8 (1958) 310

G. Derrick

Nucl. Phys. 16 (1960) 405

R. M. DeVries, J. L. Perrenoud and I. Slaus

Nucl. Phys. A188 (1972) 449

G. H. Dieke and F. S. Tomkins

Phys. Rev. 76 (1949) 283

F. S. Dietrich, D. W. Heikkinen, K. S. Snover and K. Ebisawa

Phys. Rev. Lett. 38 (1977) 156

M. Drösg

Nucl. Sci. Eng. 67 (1978) 190

ENDF/B-5

Evaluated Nuclear Data File (National Nuclear Data Center Evaluation B-5 for ^{12}C and ^{16}O, Brookhaven National Laboratory)

R. D. Evans

The Atomic Nucleus (McGraw-Hill, New York, 1955), pp. 713, 791

D. D. Faul, B. L. Berman, P. Meyer and D. L. Olson

Phys. Rev. Lett. 44 (1980) 129

D. D. Faul, B. L. Berman, P. Meyer and D. L. Olson

Phys. Rev. C24 (1981) 849

L. L. Foldy

Phys. Rev. 92 (1953) 178

J. L. Friar, B. F. Gibson, D. R. Lehman and G. L. Payne

Phys. Rev. C25 (1982) 1616

B. F. Gibson and D. R. Lehman

Phys. Rev. C29 (1984) 1017

D. W. Glasgow et al.

NBS SP 425 (1975) 866

C. R. Gould et al.

IEEE Trans. Nucl. Sci. NS-28 (1981) 3708

C. R. Gould and N. R. Roberson

IEEE Trans. Nucl. Sci. NS-30 (1983) 3758

E. Hayward

Photonuclear Reactions (U.S. Department of Commerce Monograph 118, National Bureau of Standards, Washington, 1970), p. 15

P. P. Guss

Duke University, private communication (1982)

J. A. Hendry and A. C. Phillips

Nucl. Phys. A211 (1973) 533

M. A. Hennell and L. M. Delves

Nucl. Phys. A246 (1975) 490

L. G. Holzsweig and R. V. Poore

IEEE Trans. Nucl. Sci. NS-28 (1981) 3815

J. C. Hopkins and G. Breit

Nucl. Data Tab. A9 (1971) 137

L. Hulthén and M. Sugawara

Handbuch der Physik 39 (1957) 14

M. J. Jensen

Ph.D. dissertation, North Carolina State University (1981) (unpublished)

S. E. King, Y. C. Lau and C. R. Gould

IEEE Trans. Nucl. Sci. NS-28 (1981) 3822

S. E. King

Ph.D. dissertation, Duke University (1983) (unpublished)

S. E. King, N. R. Roberson, H. R. Weller and D. R. Tilley

Phys. Rev. C30 (1984) 21

H. Kitazawa

Tokyo Institute of Technology, private communication (1980)

R. Kosiek, D. Müller, R. Pfeiffer and O. Merwitz

Phys. Lett. 21 (1966) 199

S. K. Kundu, Y. M. Shin and G. D. Wait

Nucl. Phys. A171 (1971) 384 and Ph.D. dissertation, University of Saskatchewan (1972) (unpublished)

C. M. Lederer and V. S. Shirley eds.

Table of Isotopes (John Wiley and Sons, New York, 1978)

D. R. Lehman

The George Washington University, private communication (1984)

P. W. Lisowski, R. L. Walter, C. E. Busch and T. B. Clegg

Nucl. Phys. A242 (1975) 298

R. E. Marrs, E. G. Adelberger, K. A. Snover and M. D. Cooper

Phys. Rev. Lett. 35 (1975) 202

J. L. Matthews, T. Kruse, M. E. Williams, R. O. Owens and W. Savin

Nucl. Phys. A223 (1974) 221

G. Mitev, H. R. Weller and D. R. Tilley

Nucl. Instr. Meth. 224 (1984) 324

H. W. Newson, E. G. Bilpuch, F. O. Purser, J. R. Boyce and T. B. Clegg

Nucl. Instr. Meth. 122 (1974) 99

G. G. Ohlsen et al.

Phys. Rev. Lett. 27 (1971) 599

G. G. Ohlsen

Rep. Prog. Phys. 35 (1972) 717

T. Ohmura

Progr. Theoret. Phys. 38 (1967) 626

T. Ohmura

Progr. Theoret. Phys. 41 (1969) 419

P. Paul

"Large NaI Detectors," in Nuclear Spectroscopy and Reactions Part A (J. Cerny, ed., Academic Press, New York, 1974), p. 345

G. L. Payne, J. L. Friar, B. F. Gibson and I. R. Afnan

Phys. Rev. C22 (1980) 823

G. L. Payne, J. L. Friar and B. F. Gibson

Phys. Rev. C22 (1980) 832

R. Pfeiffer

Z. Physik 208 (1968) 129

D. O. Riska

Nucl. Phys. A350 (1980) 227

N. R. Roberson and S. E. Edwards

IEEE Trans. Nucl. Sci. NS-28 (1981) 3834

C. Rolfs

Nucl. Phys. A217 (1973) 29

M. E. Rose

Elementary Theory of Angular Momentum (John Wiley and Sons, New York, 1957), p. 34

T. Sasakawa, H. Okuno and T. Sawada

Phys. Rev. C23 (1981) 905

R. B. Schwartz, R. A. Schrack and H. T. Heaton II

MeV Total Neutron Cross Sections (U.S. Department of Commerce, National Bureau of Standards, Washington, 1974)

P. Schwarz et al.

Nucl. Phys. A398 (1983) 1

J. D. Seagrave

"The Elastic Channel in Nucleon-Deuteron Scattering," in Three Body Problem in Nuclear and Particle Physics (J. S. C. McKee and P. M. Rolph eds., American Elsevier Pub. Co., New York, 1970), p. 41

J. D. Seagrave et al.

Ann. Phys. 74 (1972) 250

R. G. Seyler and H. R. Weller

Phys. Rev. C20 (1979) 453

A. J. F. Siegert

Phys. Rev. 52 (1937) 787

D. M. Skopik, H. R. Weller, N. R. Roberson and S. A. Wender

Phys. Rev. C19 (1979) 601

D. M. Skopik, D. H. Beck, J. Asai and J. J. Murphy II

Phys. Rev. C24 (1981) 1791

D. M. Skopik et al.

Phys. Rev. C28 (1983) 52

D. M. Skopik

University of Saskatchewan, private communication (1984)

E. Storm and H. I. Israel

Nucl. Data Tab. A7 (1970) 565

M. Suffert, W. Feldman, J. Mahieux and S. S. Hanna

Nucl. Instr. Meth. 63 (1968) 1

J. D. Turner

Ph.D. dissertation, Duke University (1978) (unpublished)

S. van der Woude, M. L. Halbert and C. R. Bingham

Phys. Rev. Lett. 26 (1971) 909

D. J. Wagenaar

Duke University, private communication (1981)

L. Ward, D. R. Tilley, D. M. Skopik, N. R. Roberson and H. R. Weller

Phys. Rev. C24 (1981) 317

A. H. Wapstra and K. Bos

At. Data and Nucl. Data Tables 19 (1977) 177

H. R. Weller and N. R. Roberson

Rev. Mod. Phys. 52 (1980) 699

H. R. Weller and N. R. Roberson

IEEE Trans. Nucl. Sci. NS-28 (1981) 1268

H. R. Weller

Duke University, private communication (1984)

S. A. Wender, C. E. Floyd, T. B. Clegg and W. R. Wylie

Nucl. Instr. Meth. 174 (1980) 341

W. Wölfli, R. Bösch, J. Lang, R. Müller and P. Marmier

Phys. Lett. 22 (1966) 75

G. T. Wright

Phys. Rev. 91 (1953) 1282

A ELECTRONICS CIRCUITS

A block diagram of the electronics employed in the $^{2}H(n,\gamma)^{3}H$ experiment is displayed in Figure A-1. The energy signal from the NaI detector is gated by the output of a differential discriminator and sent to the ADC. The computer sorts the energy signals into "accepts" or "rejects" spectra depending on whether or not a coincidence with the NE110 shield occurred. A coincidence circuit between the detector and shield produces router signals which are sent to the ADC and which indicate that the event should be rejected. Another coincidence circuit between the detector and shield, but with a different amount of delay in it, counts accidental coincidences. This information is used to correct the data for counts lost due to accidental coincidences. An LED pulses light into the NaI crystal creating a reference "peak" for the gain stabilizer.

A coincidence circuit between the NaI detector and NE232 target produces a TAC signal which is stored in the computer. Energy signals from the NaI detector are sorted according to time windows (gates) set in the TAC spectrum. This allows both desired data and background to be measured simultaneously. Energy signals from the scintillating target are gated by the output of the NaI differential discriminator and sent to the ADC in order to produce recoil spectra. An LED pulses light into the NE232 scintillator to enable monitoring of the gain stability.

Two circuits such as the one displayed in Figure A-1, corresponding to two NaI detectors and NE110 shields, were employed in

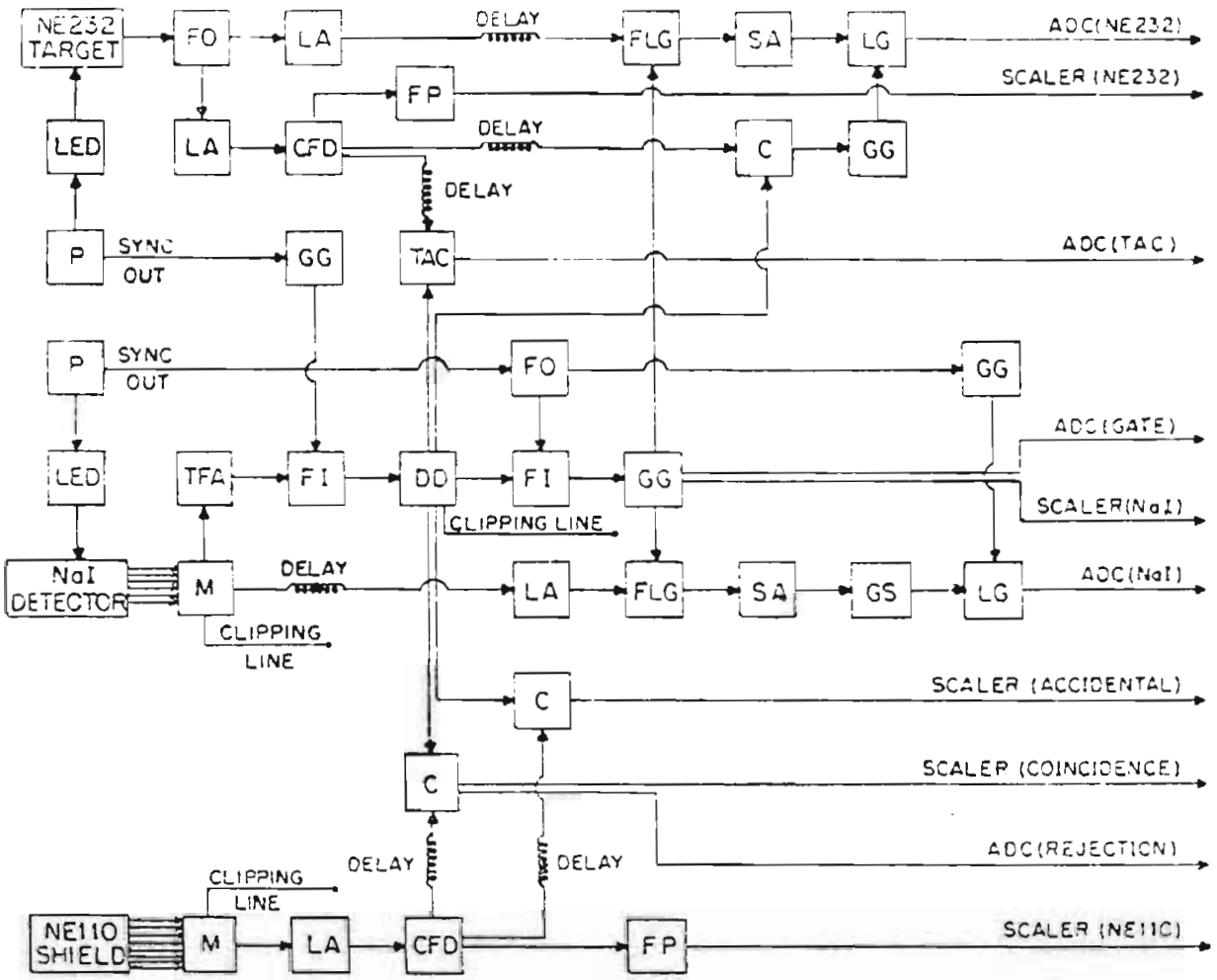

ADC	ANALOG-TO-DIGITAL CONVERTER	GS	GAIN STABILIZER
C	COINCIDENCE	LA	LINEAR AMPLIFIER
CFD	CONSTANT FRACTION DISCRIMINATOR	LED	LIGHT EMITTING DIODE
DD	DIFFERENTIAL DISCRIMINATOR	LC	LINEAR GATE
FI	FAN IN	M	MIXER
FLG	FAST LINEAR GATE	P	PULSER
FO	FAN OUT	SA	SPECTROSCOPY AMPLIFIER
FP	FAST PRESCALER	TAC	TIME-TO-ANALOG CONVERTER
GG	GATE GENERATOR	TFA	TIMING FILTER AMPLIFIER

Figure A-1. Block diagram of electronics for one NaI detector, shield and target.

the experiment.

An NE110 scintillator was placed directly in the path of the neutron beam and use to monitor the 0° neutron flux. The circuit employed for this purpose is displayed in Figure A-2. The fast and slow signals from the scintillator were amplified and routed to a TAC. As a consequence of different rise times among the fast signals, a pulse shape discrimination (PSD) spectrum was stored in the computer. Two peaks, corresponding to γ-rays and neutrons, appeared in the spectrum. External gating was applied to the (same) ADC in order to store only the neutron peak. The accumulated counts, corresponding to neutrons only, were recorded.

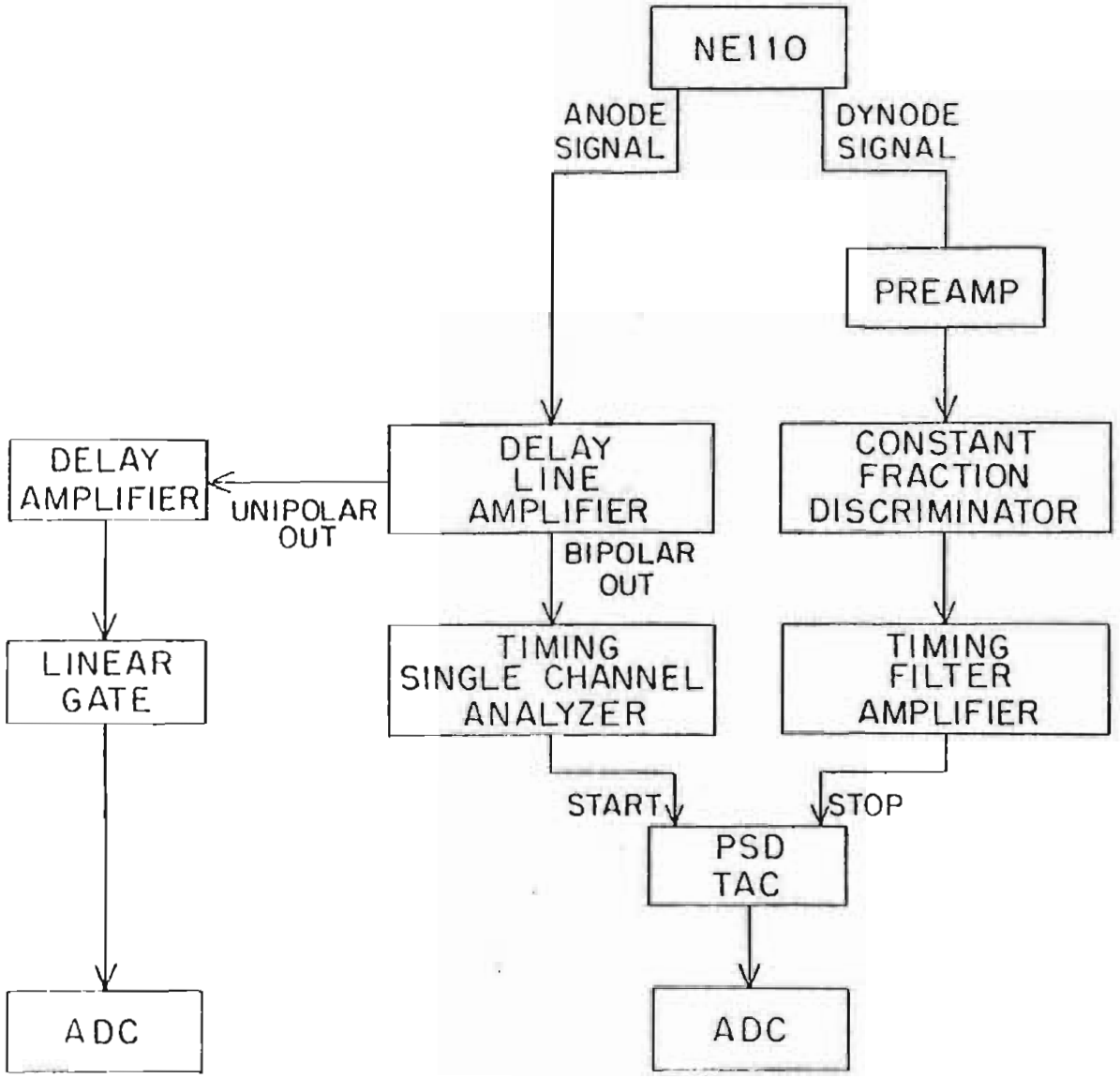

Figure A-2. Neutron monitor electronics.

B POLYNOMIALS RELEVANT TO ANGULAR DISTRIBUTION FITTING

Explicit forms of Legendre and associated Legendre polynomials, which were fit to angular distribution data according to Equations 4-1 and 4-2, are presented in Table B-1. The relations among coefficients of the Legendre expansion (see Equation 4-1) and coefficients of the sine-cosine expansion (see Equation 4-8) are given in Table B-2.

Table B-1. Legendre polynomials and associated Legendre polynomials of the first kind.

Legendre Polynomials
$P_0(\theta) = 1$
$P_1(\theta) = \cos \theta$
$P_2(\theta) = \frac{1}{2} (3 \cos^2 \theta - 1)$
$P_3(\theta) = \frac{1}{2} (5 \cos^3 \theta - 3 \cos \theta)$
$P_4(\theta) = \frac{1}{8} (35 \cos^4 \theta - 30 \cos^2 \theta + 3)$
Associated Legendre Polynomials
$P_0^1(\theta) = 0$
$P_1^1(\theta) = \sin \theta$
$P_2^1(\theta) = 3 \sin \theta \cos \theta$
$P_3^1(\theta) = \frac{3}{2} \sin \theta (5 \cos^2 \theta - 1)$
$P_4^1(\theta) = \frac{5}{2} \sin \theta (7 \cos^3 \theta - 3 \cos \theta)$

Table B-2. Relations among coefficients of the Legendre expansion (A_0, a_1, a_2, a_3 and a_4) and coefficients of the sine-cosine expansion (a, b, β, γ, and ε). See Equations 4-1 and 4-7.

$a = A_0 \left(1 + a_2 + a_4\right)$	$A_0 = a + b \left(\frac{2}{3} + \frac{2}{15}\gamma\right)$
$b = A_0 \left(-\frac{3}{2} a_2 - \frac{5}{8} a_4\right)$	$a_1 = \dfrac{\frac{2}{5}\beta + \varepsilon}{\frac{a}{b} + \frac{2}{3} + \frac{2}{15}\gamma}$
$\beta = \dfrac{-\frac{5}{2} a_3}{\left(-\frac{3}{2} a_2 - \frac{5}{8} a_4\right)}$	$a_2 = \dfrac{-\frac{2}{3} + \frac{2}{21}\gamma}{\frac{a}{b} + \frac{2}{3} + \frac{2}{15}\gamma}$
$\gamma = \dfrac{-\frac{35}{8} a_4}{\left(-\frac{3}{2} a_2 - \frac{5}{8} a_4\right)}$	$a_3 = \dfrac{-\frac{2}{5}\beta}{\frac{a}{b} + \frac{2}{3} + \frac{2}{15}\gamma}$
$\varepsilon = \dfrac{a_1 + a_3}{\left(-\frac{3}{2} a_2 - \frac{5}{8} a_4\right)}$	$a_4 = \dfrac{-\frac{8}{35}\gamma}{\frac{a}{b} + \frac{2}{3} + \frac{2}{15}\gamma}$

C MEASURED $^{2}H(n,\gamma)^{3}H$ DIFFERENTIAL CROSS SECTIONS

Table C-1. Measured $^{2}H(n,\gamma)^{3}H$ center-of-mass differential cross sections of this work. The uncertainties are purely statistical. Estimates of systematic uncertainties in cross section measurements are presented in Table 4-9.

E_n(lab) (MeV)	θ_γ(c.m.) (degrees)	$\sigma(\theta_\gamma)$ (μb/sr)
6.85	90.0	1.33 ± 0.029
9.00	55.0	0.81 ± 0.045
9.00	72.5	1.19 ± 0.047
9.00	102.6	1.26 ± 0.051
9.00	125.0	1.09 ± 0.043
9.00	136.8	0.78 ± 0.039
10.80	55.0	0.76 ± 0.044
10.80	72.7	1.03 ± 0.055
10.80	90.0	1.21 ± 0.062
10.80	112.7	1.16 ± 0.056
10.80	137.0	0.76 ± 0.040
14.00	68.0	0.62 ± 0.18
14.00	127.7	0.82 ± 0.10

BIOGRAPHY

George Mitev was born in Novi Sad, Yugoslavia on October 9, 1955. His mother, Milosava Živković, was born Yugoslav, and his father, Atanas Geno Mitev, was born Bulgarian. The family left Yugoslavia shortly after his birth and moved, after three years in Belgium and eleven years in Canada, to the United States. George graduated from Irvington High School, New Jersey in 1973. His interest in physics was realized during undergraduate studies at Florida State University, leading to graduate school in physics at Duke University as of August, 1978. He has been employed as a research assistant at the Triangle Universities Nuclear Laboratory for the past five years.